The Expanding Solar System Resonance Theory: A Geocentric Model of Earth's Precession Cycles, Eclipses and Deep-Time Climate

D. van Sonsbeek*

Independent Researcher, Den Dolder, The Netherlands

September 5, 2026

Abstract

Three major frameworks in planetary science — Kepler's orbital geometry, Milankovitch climate theory, and Laplace–Lagrange secular perturbation theory — describe planetary motion with high precision, yet no unifying principle connects precession timescales, orbital amplitudes, and the collective structure of the solar system. We present a geometric model in which two counter-rotating reference points, with periods in the Fibonacci ratio 13:3, generate a 335,317-year master cycle at J2000 (the Earth Fundamental Cycle H, slowly evolving to $H(t)$ across geological time per the Expanding Solar System Resonance Theory of section 11) from which Earth's major precession periods emerge as integer Fibonacci divisions. From this single timescale we identify 6 structural laws connecting the orbital inclinations and eccentricities of all eight planets through Fibonacci numbers: a Fibonacci cycle hierarchy for Earth's precession periods (Law 1), paired amplitude-constant and collective-balance laws on inclinations (Laws 2–3) and eccentricities (Laws 4–5), and a Saturn–Jupiter–Earth resonance locking Jupiter's ICRF perihelion and Saturn's ecliptic perihelion to the climate-recorded obliquity beat at $8H/65$ (Law 6). All 6 laws require zero free parameters beyond the master cycle itself; two empirical constants (ψ for inclination amplitudes, K for eccentricity amplitudes), each derived from Earth, predict all eight planets. Using J2000 orbital elements (a, m, i from JPL/DE440) plus phase-derived base eccentricities, Laws 3 and 5 reach 99.9974% and 99.8636% respectively from Fibonacci divisors with no forced constraints. A joint permutation test over the 4 empirical laws yields $p = 1.5 \times 10^{-4}$ (conservative) to $p = 1.0 \times 10^{-6}$ (Monte Carlo), corresponding to 3.62–4.75 σ. A formation-epoch mechanism (KAM-selected Fibonacci configurations frozen at protoplanetary disk dissipation) explains the precision; the five standard Milankovitch cycles emerge as H/n with Fibonacci-related indices; Saturn's observed ecliptic-retrograde perihelion precession is decomposed in both frames and carried as a window-era motion (the long-term secular mean is prograde); and Earth is identified as the sole planet with prograde ICRF perihelion precession. A geocentric 3D simulation reproduces the positions of the Sun, Moon, and all eight planets — including Earth's own obliquity, eccentricity, and inclination — to $< 0.09°$ RMS against JPL Horizons (~1800–2200 AD).

The framework produces testable consequences for Earth, including a unified obliquity formula and a reinterpretation of the 100,000-year glacial cycle as a multi-planet eigenmode-beat signal modulating Earth's orbital plane (empirical centroid at the $s_1 - s_4$ nodal eigenmode beat at 107.3 kyr — a planet-pair orbital-plane coupling, not direct eccentricity forcing). These are operationalised in a canonical three-layer Climate Formula: a 33-integer L1 lattice on $8H$ (positions fixed by orbital geometry, only per-line amplitudes fitted), a 3-line L2 silicate-weathering carbon thermostat (405-kyr fundamental + 202/135-kyr harmonics), and L3 Heaviside step transitions at six major Cenozoic boundary-condition changes. Action-angle closure of the obliquity-sector secular dynamics — distinct from Chirikov–KAM stability — forces eigenfrequencies onto integer divisors of $8H$ and provides the mechanism for the L1 lattice. Sequential ridge regression per climate regime on four independent proxy records (LR04, CENOGRID, EPICA Dome C CO_2, CenCO2PIP CO_2) reaches R^2 up to 0.87 (post-MPT LR04) and 0.76 (CenCO2PIP 0–66 Ma). A frequency-resolved decomposition of the L1 amplitudes per orbital band yields a Charney climate sensitivity ECS = 3.61 K, consistent with published paleo-ECS reconstructions. Cross-tabulating the 33 L1 lattice integers under the Berger eigenmode-beat convention and the model's per-planet attribution gives 0 of 33 fully agreeing on both planet and mechanism — the two frameworks identify the same periods but disagree on every per-band attribution. The model generates 27 testable predictions, including frame-decomposition tests of Earth-measured perihelion rates and deep-time claims from the Expanding Solar System Resonance Theory (Earth-Moon genesis at the rigid Roche limit at ~4.5 Ga, Devonian day counts matching Wells 1963 and Wu et al. (2024) to 0.01%, tidal-lock asymptote at ~87 $R_\oplus$, Lunar Precession Invariant $T_{\text{apsidal}} \times H = \text{const}$). The same ΔT formula (pure-tidal Farhat + L1-coupled $\alpha(t)$ GIA correction anchored on satellite gravimetry (Cox & Chao, 2002)) places the model umbra within a ±4-hour scan window of the observation site for 21/26 documented solar eclipses spanning −762 to 2026 CE, with 5/26 geographic-class events. On the 267-event Stephenson et al. (2016) lunar timing set the mean |residual| is 20.2 min. The framework rejects the full Munk-MacDonald non-tidal speedup and includes GIA via $\alpha(t)$ with zero parameters fitted to eclipse data. BepiColombo (science operations from 2027) and the Vera Rubin Observatory (LSST, 2025–2035) provide near-term discriminating tests. The model uses 6 adjustable parameters; all data, formulas, and a 3D simulation are publicly available.

Keywords: celestial mechanics, precession, obliquity, eccentricity, Milankovitch cycles, orbital dynamics, Fibonacci sequence, invariable plane, reference frame effects, BepiColombo, Mercury perihelion, angular momentum deficit, KAM theory, paleoclimate, 100,000-year glacial cycle, Mid-Pleistocene Transition, climate sensitivity, secular eigenfrequencies, Saturn–Jupiter resonance, Expanding Solar System Resonance Theory, tidal recession, paleo-day-count, historical solar eclipses, historical lunar eclipses, $\alpha(t)$ climate-driven GIA correction, glacial isostatic adjustment, ΔT validation

1. Introduction

1.1 The Missing Link

Modern astronomy describes planetary orbits with extraordinary precision, yet three major frameworks operate in isolation. Kepler's laws describe orbital geometry. Milankovitch theory describes Earth's climate cycles through eccentricity, obliquity, and precession. Laplace–Lagrange secular theory describes long-term orbital perturbations and angular momentum exchange. No framework connects the *timescales* of precession, the *amplitudes* of orbital inclinations and eccentricities, and the *collective structure* of the solar system within a single mathematical description.

This disconnection leaves fundamental questions unanswered. Why does Earth's obliquity oscillate at ~41k years? Why does eccentricity vary quasi-periodically? Why do Fibonacci ratios appear in planetary period ratios (Pletser, 2019; Aschwanden, 2018)? Each question has partial answers within its own framework, but no unifying principle connects them.

1.2 Open Questions

Three long-standing problems motivate this work:

1. **The 100,000-year problem**: Geological records show a dominant ~100,000-year glacial cycle, but Milankovitch eccentricity provides only ~0.2% insolation change — too weak without amplification mechanisms (Hays et al., 1976; Muller & MacDonald, 1997a). The theoretically dominant ~400,000-year eccentricity cycle is largely absent from climate records. This remains unsolved: Barker et al. (2025) continue to debate the distinct roles of precession, obliquity, and eccentricity, while the Mid-Pleistocene Transition is described as "one of paleoclimatology's great unsolved puzzles."
2. **No unified precession framework**: Axial precession (luni-solar torque), apsidal precession (planetary perturbations), and obliquity variation (secular perturbations) share gravitational origins but are modeled independently (Capitaine et al., 2003; Laskar et al., 1993; Berger, 1988).
3. **No single-formula predictions**: Current models rely on polynomial fits to numerical integrations, valid over limited time ranges. Vondrák et al. (2011) extended IAU 2006 precession to ±200,000 years — the state of the art. No closed-form solution exists for the gravitational n-body problem.

1.3 Approach: Bottom-Up from Observed Motion

Standard paleoclimate and secular celestial-mechanics analysis proceeds top-down: take the observed climate spectrum (LR04 peaks at ~100, ~41, ~23 kyr), construct beat frequencies ($k + g_j$, $g_i - g_j$, $s_i - s_j$, $\ldots$) from Laplace–Lagrange secular eigenmodes, and select which beat explains which climate peak by fitting amplitudes to the data. The eigenmodes themselves are mathematically rigorous — they are the eigenvalues of the secular perturbation matrix capturing gravitational coupling between all eight planets — but the interpretive overlay that maps a particular beat to a particular climate signal is climate-data-driven inference. Successive theoretical refinements (Laplace's Great Inequality, mode mixing, post-Newtonian relativistic corrections, chaotic-diffusion modelling (Laskar, 1989)) accumulate to reconcile predicted with observed planetary motion. The open puzzles enumerated above persist because no clean beat explanation matches the empirically observed climate spectra.

The methodology of this work reverses this direction. We begin from *directly observed orbital motion*. Earth's principal precession periods are measured against IAU/JPL/Horizons reference data and anchored observationally to the 1246 AD perihelion–solstice alignment, setting the Earth Fundamental Cycle $H = 335,317$ yr at the J2000 reference epoch (section 11 extends this to a slowly-evolving $H(t)$ in deep time; the variation is sub-percent within ± a few Myr of J2000 and grows to ~8% at the Devonian). All eight planets' principal cycle periods are then measured against JPL Horizons / WebGeoCalc data (1800–2100 AD; RMS positional accuracy <0.09° across all nine targets), and turn out to divide a single longer cycle $8H = 2,682,536$ yr as integer fractions $8H/N$ — the Solar System Resonance Cycle (subsection 6.3). Only *after* this integer-divisor structure has been established from motion alone is the $8H$ lattice overlaid onto the climate record (subsection 10.5): the L1 orbital-forcing layer of the canonical Climate Formula consists of 32 lattice integers with positions *fixed by orbital geometry*, with only the per-line amplitudes a_n, b_n fitted against LR04 (Lisiecki & Raymo, 2005), CENOGRID (Westerhold et al., 2020), EPICA Dome C CO_2 (Bereiter et al., 2015), and CenCO2PIP CO_2 (CenCO2PIP Consortium, 2023).

The structural difference makes the framework falsifiable in a way the classical framework is not. Standard secular theory has a large and flexible set of available beat frequencies: virtually any climate peak between ~10 kyr and ~500 kyr can be reached by some combination of g_i and s_j eigenmodes with k, so the spectral peaks themselves cannot disconfirm the framework. The Holistic model commits to integer-divisor structure: climate peaks at frequencies that do *not* equal $8H/N$ for any integer N would falsify the orbital-forcing layer. The closure test (subsection 10.5, "no orphan peaks off the $8H$ lattice") verifies exactly this — fitting all 200 integer divisors of $8H$ jointly to LR04 leaves zero residual peaks in empty lattice regions (e.g. $n \approx 43.5$, $n \approx 80$, $n \approx 140$).

1.4 The Holistic Universe Model

The starting point is an empirical observation: two of Earth's precession motions — axial and inclination — rotate in *opposite directions*, and their periods relate as a Fibonacci ratio (13:3). The same geometric construction — two reference points per planet — produces the analogous cycles for every planet. The Holistic Universe Model explores their collective structure within a geocentric 3D software simulation built from 6 adjustable parameters that reproduces all major solar system movements: invariable plane orientation, inclination and perihelion precession, eccentricity cycles, obliquity, and planetary orbits. All orbits use circular geometry with equation of center corrections and empirical parallax corrections fitted against JPL Horizons and historical transit/opposition reference data (~1800–2200 AD), achieving RMS positional accuracy within 0.09° for all nine targets (Sun, Moon, and seven planets), with six under 0.06° (Sun, Moon, Venus, Jupiter, Uranus, Neptune).

The methodology is empirical-first: orbital parameters were measured from the simulation, exported to independent analysis tools, and only then were analytical formulas and structural laws identified from the numerical output. Two categories of results emerged. First, closed-form formulas for obliquity, eccentricity, precession rates, and day/year lengths at any epoch (the unified ∼ 2,400-term predictive system, section 13). Second, six Fibonacci Laws connecting all eight planets through Fibonacci numbers and a single timescale. The simulation serves as both discovery tool and independent test bed: established results such as the invariable plane orientation of Souami & Souchay (2012) can be verified within the same framework. The simulation and full documentation are publicly available (see Data Availability).

The model does not claim to replace n-body gravitational theory. Rather, it proposes a geometric framework that captures regularities in the solar system's dynamics not immediately visible in numerical integrations.

1.5 This Paper's Contribution

We present 6 Fibonacci relations of planetary motion derived from a geometric model of the solar system. The paper is organized in three parts:

- **Part I** (section 2–section 8): The Fibonacci structure — the model, the 6 laws, physical origin, statistical significance, and exoplanet evidence
- **Part II** (section 9–section 12): Consequences for Earth — observable Earth dynamics, the canonical Climate Formula and its empirical tests (including the per-integer dual attribution and the insolation null test), the deep-time evolution of the lattice under the Expanding Solar System Resonance Theory (Earth-Moon genesis at the giant-impact epoch, paleo-day-count validation against Wells 1963 Devonian corals, tidal-lock asymptote), and Mercury's perihelion as a reference frame effect
- **Part III** (section 13–section 17): Predictions and validation — predictive formulas, calibration transparency, 27 testable predictions (including deep-time claims from the Expanding Solar System Resonance Theory of section 11), and discussion

Part I: The Fibonacci Structure

2. The Model: Two Counter-Rotating Reference Points

2.1 Foundation

The model is built on two mathematical constructs — not physical objects, but reference points that parameterize known precession phenomena:

Earth-Wobble-Center: A reference point at a distance of 0.001356 AU from Earth, circling Earth clockwise (as seen from the north ecliptic pole) once per axial precession. Period: $\sim 25,794$ years. This represents the luni-solar precession; the point marks the precession (solstice) direction. Its distance A is not a free parameter but the closure of the 1246 triangle, $e(2000)^2 = e_{\text{base}}^2 + A^2 + 2\,e_{\text{base}} A \cos\varphi$ with $\varphi = 360°\,(2000 - 1246.03)/(H/16) = 12.95°$, and it feeds Law 4 (Equation 12); the point is a marker only — Earth's eccentricity itself follows the single $H/3$ law of subsection 14.8.

Perihelion-of-Earth: A reference point near the Sun, at a distance of 0.015386 AU. This point orbits counter-clockwise around the Sun, marking the direction of Earth's closest approach. Period: $\sim 111,772$ years. This represents the planetary precession.

The model recasts these as two counter-rotating circular motions within a single geometric framework (Figure 1).

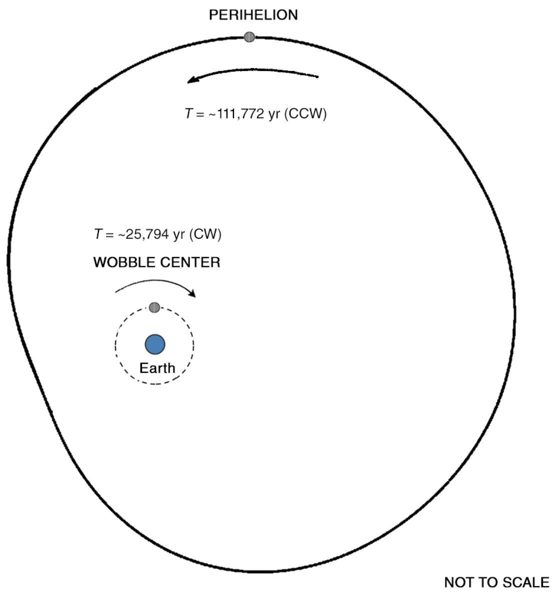

Figure 1: Schematic of the two counter-rotating reference points. Earth orbits the Earth-Wobble-Center clockwise (CW) with period $T \approx \sim 25,794$ years, while the Perihelion-of-Earth orbits counter-clockwise (CCW) around the Sun with period $T \approx \sim 111,772$ years. The 13:3 ratio produces the 335,317-year Earth Fundamental Cycle. Not to scale.

2.2 The Fibonacci Ratio and KAM Theory

The ratio of the two fundamental periods is:

$$\frac{T_{\text{incl}}}{T_{\text{axial}}} \approx \frac{\sim 111,772}{\sim 25,794} = 4.333\ldots = \frac{13}{3} \tag{1}$$

Both 3 and 13 are Fibonacci numbers (F_4 and F_7). This has theoretical grounding in the Kolmogorov–Arnold–Moser (KAM) theorem, which proves that orbital systems with "most irrational" frequency ratios are maximally stable against perturbation (Morbidelli & Giorgilli, 1995). The golden ratio $\varphi \approx 1.618$, to which successive Fibonacci ratios converge, is the most irrational number in a precise mathematical sense. Greene (1979) showed computationally that the golden-ratio torus is the last to break under perturbation. Pletser (2019) demonstrated that orbital period ratios preferentially cluster near Fibonacci fractions (∼60% vs ∼40% for non-Fibonacci), and Aschwanden (2018) found Fibonacci fractions in 73% of 932 exoplanet pairs. The 13:3 ratio thus reflects a maximally stable configuration predicted by dynamical systems theory.

KAM theory explains why Fibonacci ratios are *preferred* but not why they are realized so precisely. Across the 6 laws developed in the rest of the paper, Laws 1 and 6 are exact algebraic identities; using J2000 orbital elements (a, m, i from

JPL/DE440) and phase-derived base eccentricities, Law 3 reaches 99.9974% inclination balance and Law 5 reaches 99.8636% eccentricity balance; Laws 2 and 4 predict all oscillation amplitudes from two empirical constants (ψ and K, both derived from Earth); and Law 5 predicts Saturn's eccentricity from the other seven planets to ~0.27%. The precision comes from the solar system's formation epoch: dissipative forces in the protoplanetary disk drove orbits into the deepest Fibonacci stability wells, and disk dissipation froze the configuration in place (section 7).

2.3 The Earth Fundamental Cycle and Derived Cycles

The 13:3 ratio produces a master cycle, the Earth Fundamental Cycle:

$$H = 13 \times {\sim}25,794 = 3 \times {\sim}111,772 = 335,317 \text{ years} \quad (2)$$

H_{J2000} is a continuous, observationally fitted quantity — and under the Expanding Solar System Resonance Theory (section 11) it evolves over geological time. The integer $H_0 = 335,317 = 23 \cdot 61 \cdot 239$ is its **lattice representative**: the value used for integer-divisor bookkeeping throughout this paper. The historical Earth-rotation record independently constrains $H_{J2000} = 335,317 \pm {\sim}25$ yr (sensitivity of the ΔT drift and 1650–2017 reference-window shape to the implied LOD level, ~10 μs/day per year of H) — a cross-check on the astronomical determination from an unrelated observable.

All subsidiary cycles emerge as integer divisions of the Earth Fundamental Cycle (Table 1).

Table 1: Derived cycles from the Earth Fundamental Cycle (Law 1)

Cycle	Divisor	Duration (yr)	Fibonacci?
Earth Fundamental Cycle	1	335,317	$F_1 = 1$
Inclination Precession	3	~111,772	$F_4 = 3$
Ecliptic Precession	5	~67,063	$F_5 = 5$
Obliquity cycle	8	~41,915	$F_6 = 8$
Axial precession	13	~25,794	$F_7 = 13$
Perihelion precession	16	~20,957	$13 + 3 = 16$

The perihelion precession period emerges from the meeting frequency of the two counter-rotating motions:

$$\frac{1}{T_{\text{perihelion}}} = \frac{1}{T_{\text{axial}}} + \frac{1}{T_{\text{incl}}} = \frac{1}{{\sim}25,794} + \frac{1}{{\sim}111,772} = \frac{1}{{\sim}20,957} \quad (3)$$

The frequencies add (rather than subtract) because the motions are in opposite directions. **Earth's H/Fibonacci hierarchy is unique among the planets** (Law 1, section 3); the other planets' precession periods divide the Solar System Resonance Cycle $8H$ (subsection 2.5) by various integers, mostly non-Fibonacci. Jupiter's perihelion ($H/5$ ecliptic, $H/8$ ICRF) and Saturn's perihelion ($H/8$ ecliptic, $H/21$ ICRF) fall near these Fibonacci anchors, with their 8H-lattice values sitting one lattice integer away ($8H/39$, $8H/65$, $8H/169$ — the matched quantities being Earth-frame beats, $|s_3|$ and $k + s_3$, at J2000); both the Fibonacci anchors and the 8H-lattice values — and the Earth-frame beat identity that links them — are the subject of Law 6 (section 6).

2.4 The Balanced Year (Epoch Anchor)

The model uses a reference epoch called the Balanced Year, calculated from the last perihelion–solstice alignment:

$$T_{\text{balanced}} = 1246.03 \text{ AD} - 14.5 \times 20,957.31 = -302,635 \quad (4)$$

At this epoch (302,635 BC), the axial tilt and inclination tilt effects are in exact opposition, producing the Pythagorean mean obliquity of ~23.453° (the geometric mean 23.41353° increased by perpendicular perihelion and ecliptic tilt components). The value is not arbitrary: within the 335,317-year cycle, the observed inclination trend (currently decreasing) and the observed obliquity trend (currently decreasing) must be simultaneously reproduced. Only a narrow range of phase offsets achieves this, and $14.5 \times {\sim}20,957$ emerged as the only configuration consistent with all observational constraints — the current rates of change, the J2000 values, and the known oscillation ranges. This serves as the phase-zero reference for all cycle calculations at J2000, analogous to how J2000 serves as the standard astronomical epoch. All quoted balanced-year dates, and the cycle period H used to compute them, are J2000-anchor values; under the deep-time framework of section 11, the interval between two balanced events is more precisely the integral $\int 1/H(t)\,dt$, which differs from the snapshot product $H_{J2000} \times N$ by <0.1% within ± a few Myr of J2000 and grows to ~8% at the Devonian.

2.5 The Solar System Resonance Cycle ($8H$)

The preceding subsections developed H as Earth's master cycle. Each of the other seven planets has its own characteristic master period; all eight converge at a common super-period of eight Earth Fundamental Cycles — the Solar System Resonance Cycle:

$$8H = 2,682,536 \text{ years} \quad (5)$$

The same six kinds of cycles observed for Earth — axial precession, perihelion precession (ecliptic and ICRF), inclination oscillation, ascending-node regression, obliquity oscillation, and eccentricity oscillation — exist for every planet (visible in JPL ephemeris data and long-term integrations such as Laskar's La2010 solution). What unifies them is that across all eight planets, every one of these cycles is an integer divisor of $8H$. After one Solar System Resonance Cycle (~2.68 million years), each planet returns to its starting configuration simultaneously across all six cycle types.

Empirically, the Pliocene and Pleistocene epochs each span approximately one Solar System Resonance Cycle (~2.6–2.8 Myr); a pre-registered test of $8H$ as a Phanerozoic-wide pacer of major geological boundaries gave a null result, consistent with the framework's claim being about orbital-forcing structure rather than geological-event pacing.

The Solar System Resonance Cycle plays three structural roles in the model:

- **Universal divisor**: Every planetary cycle period is expressible as $8H/N$ for some integer N. For example, Earth's axial precession ($H/13$) is $8H/104$, its perihelion precession ($H/16$) is $8H/128$, and its obliquity cycle ($H/8$)

is $8H/64$. This integer-divisor property holds for all eight planets and all six cycle types.

- **Ascending-node periods are integer divisors of** $8H$: each fitted planet's ascending-node regression period takes the form $8H/N$ for an integer N, with Jupiter and Saturn locked to a shared $N = 36$. Across all 7 fitted planets, the $8H/N$ integers reproduce JPL's J2000-fixed-frame ascending-node trends with a cumulative residual error of $\sim 5.8''$/century ($\approx 0.8''$/century per planet, subsection 6.5).
- **Mean obliquity computation**: the analytical mean obliquity (Equation 16) is defined as the time-average over $8H$, the period over which all cosine terms in the two-component obliquity formula return to their starting values.

3. Law 1: Fibonacci Cycle Hierarchy

Earth's major precession periods divide the Earth Fundamental Cycle $H = 335,317$ *by Fibonacci-related divisors — $H/3$ (inclination), $H/5$ (ecliptic), $H/8$ (obliquity), $H/13$ (axial), and $H/16$ (perihelion). The Fibonacci addition rule connects them:* $3 + 5 = 8$, $5 + 8 = 13$, *and* $13 + 3 = 16$ *for the perihelion period.*

The resulting periods (Table 1) obey a beat-frequency rule inherited from the Fibonacci recurrence $F_n + F_{n+1} = F_{n+2}$:

$$\frac{1}{H/F_n} + \frac{1}{H/F_{n+1}} = \frac{1}{H/F_{n+2}} \tag{6}$$

Any two consecutive Fibonacci periods combine to produce the next. The entire hierarchy is generated by the interaction of just two physical periods — the axial precession ($H/13$) and the inclination precession ($H/3$) — through successive beat frequencies. Law 6 (section 6) reveals the physical mechanism behind this hierarchy.

4. Laws 2–3: Inclination Structure

Laws 2 and 3 together describe how planetary inclinations are organised against the invariable plane. Law 2 sets the *amplitude* of each planet's inclination oscillation through a single empirical constant ψ shared across all eight planets; Law 3 organises those amplitudes into a 7-vs-1 *balance* in which Saturn alone counterweights the other seven. Both laws operate in mass-weighted variables — the natural scaling for Angular Momentum Deficit (AMD), the conserved quantity governing long-term orbital stability (Laskar, 1997).

4.1 Mass-Weighted Variables and AMD

The planetary data reveals deeper structure when expressed in mass-weighted variables:

- Mass-weighted eccentricity: $\xi = e \times \sqrt{m}$
- Mass-weighted inclination amplitude: $\eta = \text{amplitude} \times \sqrt{m}$

The $\sqrt{m}$ exponent is not arbitrary: a numerical scan over all mass exponents from 0 to 1 shows that the products $d \times \eta$ across all eight planets converge to a single value only at exponent 0.50, with a relative spread of 0.11%. No other exponent achieves a spread below 28%. The same exponent makes the AMD decomposition come out mass-independent, derived in subsection 4.5.

4.2 The Invariable Plane

The invariable plane — perpendicular to the solar system's total angular momentum vector, dominated by Jupiter (~60%) and Saturn (~25%) — serves as the model's spatial reference. Unlike the ecliptic, which itself precesses, the invariable plane is fixed in inertial space. When measured against it, all planetary inclinations show smooth, predictable oscillations (Table 2).

Table 2: Planetary inclination oscillations relative to the invariable plane

Planet	d	J2000 (°)	Mean (°)	Ampl. (°)	Ecliptic period (yr)	ICRF period (yr)
Mercury	21	6.347	6.703228	±0.386501	243,867	−28,844
Venus	34	2.155	2.151359	±0.062168	−447,089	−24,387
Earth	3	1.579	1.48113	±0.63607	~20,957	+111,772
Mars	5	1.631	1.833263	±1.164287	74,515	−39,449
Jupiter	5	0.322	0.321086	±0.021405	68,783	−41,270
Saturn	3	0.925	0.984969	±0.065196	−41,270	−15,873
Uranus	21	0.995	1.015183	±0.023832	~111,772	−33,532
Neptune	34	0.735	0.743803	±0.013552	670,634	−26,825

d is the planet's Fibonacci divisor in the inclination constant (Law 2): $d \times \text{amp} \times \sqrt{m} = \psi$. Mirror pairs across the asteroid belt: Mercury–Uranus ($d = 21$), Venus–Neptune ($d = 34$), Earth–Saturn ($d = 3$), Mars–Jupiter ($d = 5$).

Determining which d-value belongs to each planet requires an exhaustive search over 7,558,272 assignments, narrowed by physical filters to a single mirror-symmetric solution (subsection 4.4). That solution predicts that Jupiter's ICRF perihelion period equals the ecliptic precession and Saturn's equals the obliquity cycle — the structural identity underlying Law 6 (section 6).

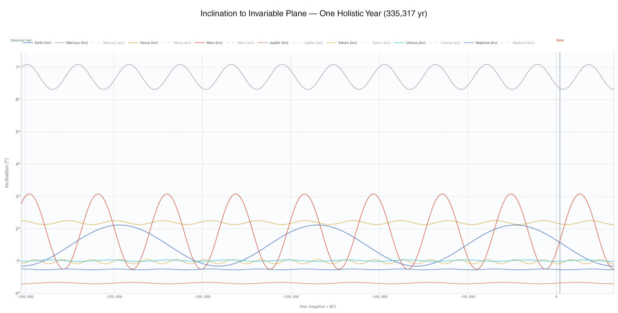

Figure 2: Inclination oscillations of all eight planets relative to the invariable plane over one Earth Fundamental Cycle ($H = 335,317$ yr), shown at their ICRF perihelion periods. Mars has the largest amplitude and completes ~8.6 cycles; Earth completes 3 cycles ($H/3$); Saturn completes 21 cycles ($H/21$ in ICRF), the highest of any planet; Jupiter completes exactly 8 cycles ($H/8$).

4.3 Law 2: The Inclination Constant

Each planet's mass-weighted inclination amplitude, multiplied by a Fibonacci quantum number, equals the same universal constant.

Defining $\eta = \text{amplitude} \times \sqrt{m}$, every planet satisfies:

$$d \times \eta = \psi \tag{7}$$

where d is a Fibonacci integer specific to each planet. The constant ψ is empirical, derived from Earth's fitted inclination amplitude:

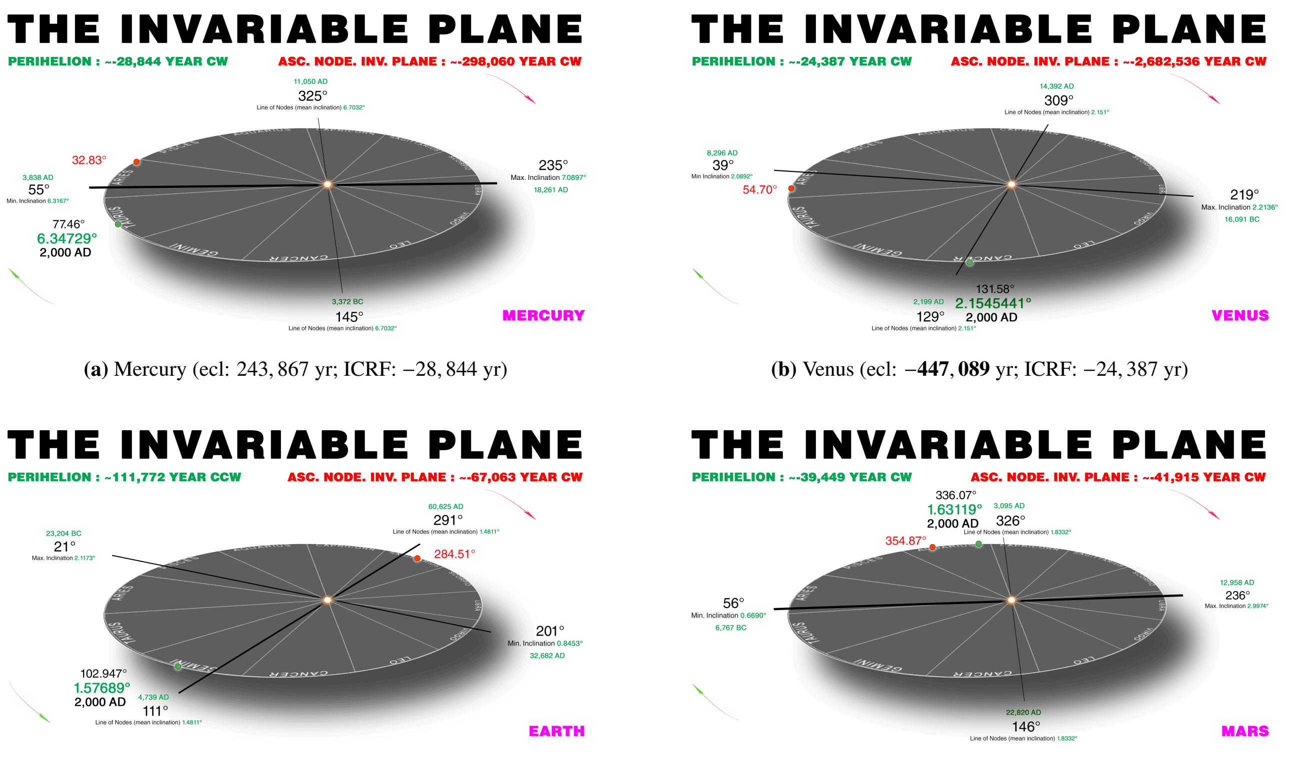

(a) Mercury (ecl: 243, 867 yr; ICRF: −28, 844 yr) **(b)** Venus (ecl: **−447, 089** yr; ICRF: −24, 387 yr)

(c) Earth (ecl: ~20, 957 yr; ICRF: **+111, 772** yr) **(d)** Mars (ecl: 74, 515 yr; ICRF: −39, 449 yr)

Figure 3: Perihelion and ascending node precession relative to the invariable plane — inner planets. Each panel shows one complete inclination oscillation cycle. The inclination oscillation is driven by the **ICRF perihelion longitude** (green dot), with per-planet inclination cycle anchors. The ascending node precesses on the invariable plane at a different rate; its role is to set the direction of the angular momentum perturbation vector that determines the vector balance. **Earth (panel c) is the only planet whose ICRF perihelion rate is prograde**, because Earth's ecliptic apsidal rate ($H/16$) exceeds the general precession ($H/13$).

$$\psi = d_E \times \mathrm{amp}_E \times \sqrt{m_E} = 3.3070 \times 10^{-3} \tag{8}$$

With zero free parameters, the model predicts inclination amplitudes for all eight planets (Table 3).

Table 3: Law 2: Inclination constant predictions

Planet	d	Fibonacci	Predicted amp	Mirror pair
Mercury	21	F_8	0.386501°	↔ Uranus
Venus	34	F_9	0.062168°	↔ Neptune
Earth	3	F_4	0.63607°	↔ Saturn
Mars	5	F_5	1.164287°	↔ Jupiter
Jupiter	5	F_5	0.021405°	↔ Mars
Saturn	3	F_4	0.065196°	↔ Earth
Uranus	21	F_8	0.023832°	↔ Mercury
Neptune	34	F_9	0.013552°	↔ Venus

Seven of the eight predicted ranges fall within the bounds of Laplace–Lagrange secular theory; Saturn exceeds its upper bound by 0.030° (range 0.92–1.05° against 0.797–1.02°), the one documented margin case, which the verification suite tracks explicitly. The check is applied per-configuration across all 15 surviving configurations in the selection pipeline (subsection 4.4). The divisors (3, 5, 21, 34) are all Fibonacci numbers, and each inner planet shares its d with its outer mirror across the asteroid belt — a structural symmetry that reflects the block-diagonal coupling of the secular system, with the asteroid belt acting as a dynamical barrier.

4.4 Configuration Selection

Each planet needs a Fibonacci divisor d and a balance group (in-phase or anti-phase). Earth is locked at $d = 3$; Jupiter and Saturn are constrained by Law 6. The remaining five planets each have $9 \times 2 = 18$ options, giving 7,558,272 candidates across four Jupiter–Saturn scenarios. Five successive physical filters narrow these to a single mirror-symmetric solution:

Table 4: Selection pipeline

Filter	Surviving
Total search space	7,558,272
Inclination balance ≥ 99.994%	767
+ Eccentricity balance ≥ 99%	96
+ Optimised anchor satisfies LL bounds (7/8)	51
+ Direction match, rate error ≤ 6″	15
+ Mirror symmetry	**1**

The first two filters depend only on d-values. The LL-bounds and direction checks depend on two additional parameters: the **anchor position** $n \in \{0, \ldots, 7\}$ (which of eight equally-spaced points in $8H$ defines the balanced year, setting all inclination cycle anchors) and the **ascending node integer** N per planet (Ω regression period = $-8H/N$). Each candidate is evaluated at its own optimal (n, N); Jupiter and Saturn share the same N to preserve lockstep regression. Of 15

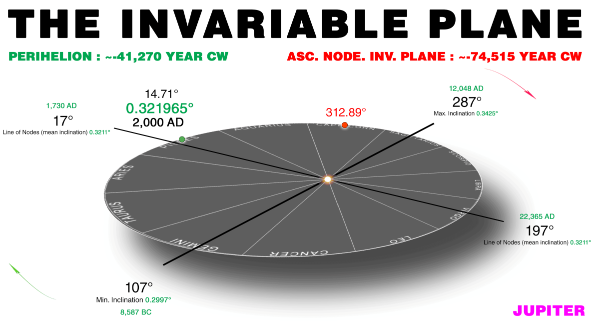

(a) Jupiter (ecl: 68, 783 yr; ICRF: −41, 270 yr)

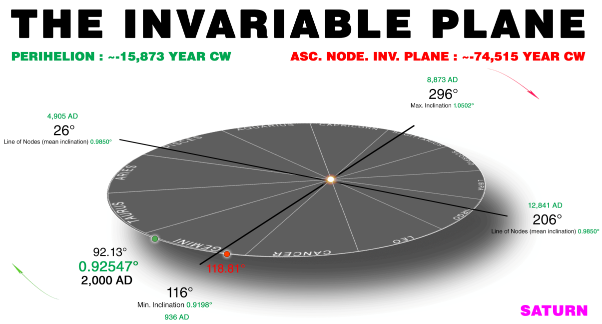

(b) Saturn (ecl: **−41, 270** yr; ICRF: −15, 873 yr)

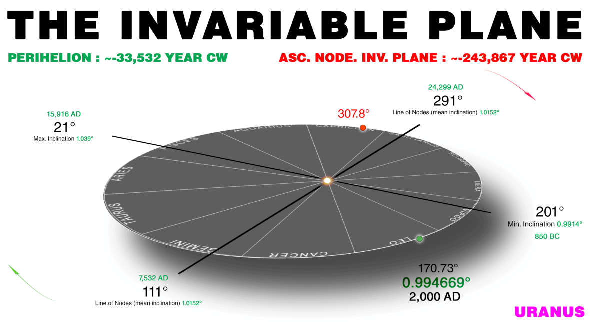

(c) Uranus (ecl: ∼111, 772 yr; ICRF: −33, 532 yr)

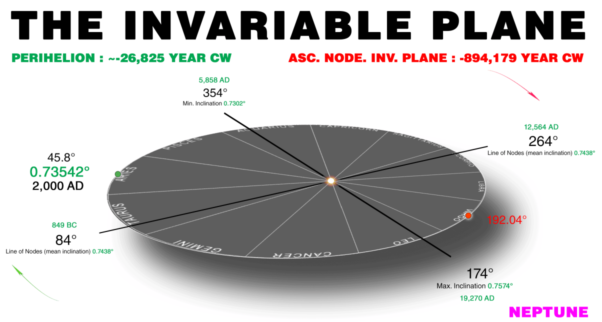

(d) Neptune (ecl: 670, 634 yr; ICRF: −26, 825 yr)

Figure 4: Perihelion and ascending node precession relative to the invariable plane — outer planets. Saturn (panel b) precesses clockwise (CW) in the ecliptic frame, caused by Jupiter's gravitational pull from inside its orbit. Saturn is **anti-phase**: its cosine sign is flipped relative to all other planets — making it the sole counterweight in the inclination balance (Law 3).

survivors, **only one is mirror-symmetric**: Me=21, Ve=34, Ma=5, Ju=5, Sa=3, Ur=21, Ne=34 (Config #4, ranked #4 of 15 by eccentricity balance at 99.8636%). Its anchor is $n = 7$ with Jupiter–Saturn $N = 36$.

4.5 Physical Meaning of ψ: Mass-Independent Energy Partition

Substituting Law 2 (amp $= \psi/(d\sqrt{m})$) into the standard AMD gives each planet's inclination oscillation AMD:

$$\mathrm{AMD}_{\mathrm{incl}} = \frac{m\sqrt{a}}{2}\left(\frac{\psi}{d\sqrt{m}}\right)^2 = \frac{\sqrt{a}\,\psi^2}{2\,d^2} \qquad (9)$$

Mass cancels exactly. Law 2 appears to depend on mass — heavier planets tilt less — but this apparent mass dependence is precisely what removes mass from the energy budget: $\sqrt{m}$ is the unique exponent that makes this cancellation work. Each planet's inclination oscillation energy depends only on its orbital distance ($\sqrt{a}$) and Fibonacci quantum number (d), not on how massive the planet is.

The divisor d acts as an energy quantum number (Table 5): higher d means less oscillation energy, scaling as $1/d^2$. Saturn dominates (56%) not because of mass (Jupiter is 3× heavier) but because $d = 3$ combined with a large orbit maximises $\sqrt{a}/d^2$. Earth carries more oscillation energy than Jupiter (18% vs 15%) despite being ∼1000× lighter. The Earth–Saturn pair ($d = 3$) carries 74% of the eight-planet total; the E–J–S resonance triad (Law 6) carries 89%. Shares are relative to the eight major planets, which carry ∼99% of the system's orbital angular momentum (Li et al., 2019).

Table 5: Inclination oscillation energy shares ($\propto \sqrt{a}/d^2$)

Planet	d	$\sqrt{a}/d^2$	Share
Mercury	21	0.0014	0.2%
Venus	34	0.0007	0.1%
Earth	**3**	**0.1111**	**18.2%**
Mars	5	0.0494	8.1%
Jupiter	5	0.0912	14.9%
Saturn	**3**	**0.3430**	**56.1%**
Uranus	21	0.0099	1.6%
Neptune	34	0.0047	0.8%

The same structural properties that make Saturn the dominant energy carrier — $d = 3$ and a large orbit — also make it the sole counterweight in the inclination balance (Law 3 below). In this mass-independent partition Saturn carries 56%; in the mass-dependent balance of Law 3, Saturn carries exactly 50% (by definition equal to the other seven combined). The gap is absorbed by mass: Jupiter is 3.3× heavier than Saturn, boosting Jupiter's balance weight relative to its energy share and redistributing the load from 56/44 to an exact 50/50 split.

Summing over all planets yields a budget equation that determines ψ's magnitude:

$$\psi^2 = \frac{2 \times \mathrm{AMD}_{\mathrm{incl}}^{\mathrm{total}}}{\sum_j \sqrt{a_j}\,/\,d_j^2} \qquad (10)$$

This fixes ψ from two formation-epoch quantities: the total inclination oscillation energy and the geometric sum $\sum \sqrt{a}/d^2$ set by Fibonacci structure and Kepler spacing. An identical mass cancellation holds for eccentricity via Law 4 (section 5).

4.6 Law 3: The Inclination Balance

The angular-momentum-weighted inclination oscillations of seven planets balance against Saturn's alone, conserving the orientation of the invariable plane.

Each planet's inclination to the invariable plane oscillates with the ICRF perihelion longitude:

$$i(t) = \bar{i} + A\cos(\varpi_{\mathrm{ICRF}}(t) - \varphi) \tag{11}$$

where $\varpi_{\mathrm{ICRF}}(t)$ is the ICRF perihelion longitude (ecliptic rate minus general precession $H/13$) and φ is a per-planet **inclination cycle anchor** derived from the System Reset epoch (~2,649,854 BC, $n = 7$; J2000-anchor projection — the integer-divisor phase structure is invariant across epochs, but the literal BC date drifts at $O(1\%)$ per Myr under the deep-time evolution of section 11). The anchors are constructed so that all eight planets reach minimum inclination simultaneously at the System Reset: $\varphi = \varpi_{\mathrm{ICRF}}(t_{\mathrm{SR}}) + 180°$ for in-phase planets (giving cos $= -1$, hence $i = \bar{i} - A$ at t_{SR}), and $\varphi = \varpi_{\mathrm{ICRF}}(t_{\mathrm{SR}})$ for Saturn (giving cos $= +1$, which combined with Saturn's flipped cosine sign — see below — also yields $i = \bar{i} - A$ at t_{SR}). All ICRF periods divide $8H = 2{,}682{,}536$ years (the Solar System Resonance Cycle; J2000 anchor — the $8H/N$ integer-divisor structure is invariant at any epoch while the literal year count rescales per section 11), so this integer-recurrence of the synchronized inclination minimum once per $8H$ is itself a structural invariant. Saturn's sign-flipped contribution — not its anchor placement — is what provides the reversed term in the angular-momentum-weighted balance sum (Law 3 below). The **ascending node** Ω_{inv} precesses on the invariable plane at a different rate and plays a complementary role: the ICRF perihelion longitude drives the magnitude of each oscillation (inside the cosine in Equation 11), while the ascending node sets the direction of the angular momentum perturbation vector $\vec{P}_j = L_j \sin(i_j)(\sin\Omega_j, \cos\Omega_j)$ that determines the vector balance.

The balance itself requires two groups:

- **In-phase group**: Mercury, Venus, Earth, Mars, Jupiter, Uranus, Neptune — cosine sign positive
- **Anti-phase group**: Saturn (alone) — cosine sign flipped

Saturn's orbital angular momentum — amplified by its large distance from the Sun — single-handedly balances the other seven planets combined. Using the structural weight $w_j = \sqrt{m_j \cdot a_j(1 - e_j^2)}/d_j$ with phase-derived base eccentricities, the inclination balance is 99.9974%. The same Fibonacci divisors and phase assignments simultaneously produce an independent eccentricity balance of 99.8636% (Law 5, subsection 5.2).

Scalar vs vector balance. Law 3 is a *scalar* balance condition: it requires that the structural weights w_j of the in-phase and anti-phase groups cancel exactly. This is the genuine physical constraint that selects the unique Fibonacci d-value configuration. A separate question is whether the angular momentum perturbation *vectors* (each planet's $L \times \sin i$ acting along its ascending node direction) cancel as 2D vectors at all times — not just on average. The vector cancellation is guaranteed by the eigenmode structure of secular perturbation theory: the invariable plane is by definition the plane where these vectors sum to zero, and any decomposition of the planetary orbits into eigenmodes (e.g., the seven Laplace–Lagrange secular modes s_1–s_8 with $s_5 = 0$) automatically preserves this cancellation. The d-value selection (Law 3 + Law 5, scalar) and the vector cancellation (eigenmode structure) operate independently and address different aspects of the same physics.

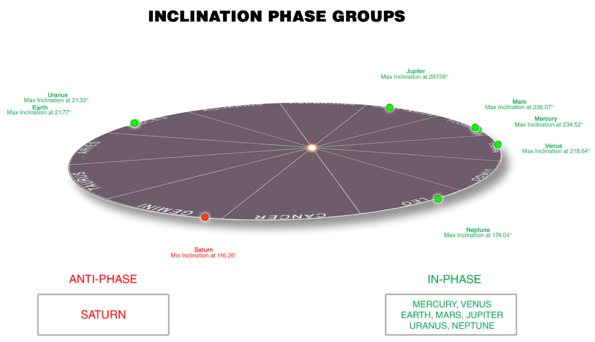

Figure 5: Inclination balance groups on the invariable plane. Seven in-phase planets (green) have positive cosine sign; Saturn alone (red, anti-phase) has flipped sign. The angular-momentum-weighted oscillations of the two groups cancel exactly.

5. Laws 4–5: Eccentricity Structure

5.1 Law 4: The Eccentricity Amplitude Constant

A single constant K predicts all eight eccentricity oscillation amplitudes from Fibonacci divisors, mass, distance, and axial tilt.

Each planet's eccentricity oscillates around a base value over its eccentricity cycle. The oscillation amplitude follows a universal formula:

$$e_{\mathrm{amp}} = K \times \frac{\sin(\bar{\varepsilon}) \times \sqrt{d}}{\sqrt{m} \times a^{3/2}} \tag{12}$$

where $\bar{\varepsilon}$ is the planet's mean obliquity (the time-averaged axial tilt, not the J2000 instantaneous value) and $K = 3.4143 \times 10^{-6}$, derived from Earth's mean obliquity (23.41353°) and eccentricity amplitude (0.001356). This is the eccentricity analog of ψ (Law 2): where ψ determines each planet's inclination amplitude from Fibonacci divisor and mass, K determines each planet's eccentricity amplitude from those same quantities plus semi-major axis and axial tilt. Both are empirical constants derived from Earth, both predict all 8 planets with zero free parameters. K's additional dependence on a and $\bar{\varepsilon}$ couples the spin and orbital domains: a planet's mean obliquity determines its eccentricity amplitude, and its eccentricity amplitude reveals its obliquity. Together, ψ and K link inclination amplitude, eccentricity amplitude, and axial tilt through just two constants. Earth's own input $e_{\mathrm{amp}} = A$ is itself derived: it closes the 1246 alignment triangle (section 2 — A 5% too small would move the perihelion–solstice alignment to 2,000 AD, 5% too large to 690 AD), so K rests on the observed J2000 eccentricity, the Law 5 base, the alignment epoch and $H/16$ alone.

Combined with the base eccentricities (Law 5 below), the full eccentricity of the seven planets other than Earth at any time is:

$$e(t) = \sqrt{e_{\text{base}}^2 + e_{\text{amp}}^2} + (-e_{\text{amp}} - h_1 \cos\theta)\cos\theta \qquad (13)$$

where $\theta = 360° \times (t - t_0)/T_{\text{cycle}}$ and $h_1 = \sqrt{e_{\text{base}}^2 + e_{\text{amp}}^2} - e_{\text{base}}$. At $\cos\theta = +1$ the formula reduces to $e_{\text{base}} - e_{\text{amp}}$ (minimum), at $\cos\theta = -1$ to $e_{\text{base}} + e_{\text{amp}}$ (maximum), and at $\cos\theta = 0$ to $\sqrt{e_{\text{base}}^2 + e_{\text{amp}}^2}$. The asymmetric $\cos\theta$ dependence (relative to a simple cosine) preserves the Law 5 eccentricity balance at every epoch, not only at the extrema — a consequence of $\delta v = K \times \sin(\bar{\varepsilon})$ for the per-planet weight change (mass and distance cancel completely). Inverting the formula — using JPL J2000 eccentricities to predict obliquities — provides an independent cross-check for all planets. Earth is the exception: its eccentricity is frame-invariant and rides the single $H/3$ line $e(t) = e'_{\text{base}}(1 + \cos\theta_3/2)$ shared with the lunar theory and the solar equation of centre (subsection 14.8); its $H/16$ beat governs the perihelion *direction*, and A enters only through Law 4.

5.2 Law 5: The Eccentricity Balance

An independent balance condition on eccentricities holds using the same Fibonacci divisors and phase groups, with Saturn alone balancing the other seven planets.

Each planet receives an eccentricity weight $v_j = \sqrt{m_j} \times a_j^{3/2} \times e_j / \sqrt{d_j}$. The weights for the seven in-phase planets sum to match Saturn's weight alone:

Balance: 99.8636% **(base eccentricities);** 99.8753% **(J2000 eccentricities)**

With base eccentricities derived from the **System Reset phase** ($n = 7$, with balance-group offsets: 90° for in-phase planets, 270° for Saturn) (Table 6), the eccentricity balance reaches 99.8636% — naturally, with no forced constraints. This is genuinely independent of Law 3: eccentricity weights differ from inclination weights by over 100-fold for some planets, yet both conditions are simultaneously satisfied by the same Fibonacci divisors. Three tests confirm it depends on the actual eccentricity values: without eccentricities the balance drops to 74%; random eccentricities give only 50–85%; and the balance peaks at linear eccentricity, dropping for other powers.

Base eccentricities for the seven non-Earth planets are derived from the System Reset phase anchor with balance-group phase offsets: in-phase planets at 90° (mean, rising), Saturn at 270° (mean, falling). Earth's base is independently determined by the Sun optimizer from its two-vector model geometry. Venus shows the largest base-to-J2000 offset (+13.7%), indicating it is well away from its oscillation midpoint at the current epoch; Mars's base is −1.9% relative to J2000. The outer planets are essentially at their midpoints (< 0.1%) because their K-derived amplitudes are negligible relative to their base eccentricities.

Table 6: Phase-derived base eccentricities

Planet	Base e	vs. J2000
Mercury	0.20563	< 0.01%
Venus	0.00771	+13.7%
Earth	0.01539	−7.9%
Mars	0.09165	−1.9%
Jupiter	0.04839	< 0.01%
Saturn	0.05387	< 0.01%
Uranus	0.04724	−0.03%
Neptune	0.00860	+0.07%

The ~0.14% residual — two-channel decomposition. The eccentricity balance reaches 99.8636% but not exactly 100%. Sensitivity analysis on the 8-planet sum rules out mis-measurement of any single planet's mass or orbit: the required shifts are 4–6 orders of magnitude larger than DE440 mass and JPL period precision. The gap is in what is missing from the eight-planet sum, and decomposes into two physically-motivated channels.

(i) Minor-body contributions (~96% of the residual). Substituting Law 4 (Equation 12) into the Law-5 weight $v = \sqrt{m}\, a^{3/2}\, e / \sqrt{d}$ produces a striking cancellation: every body following Law 4 contributes a uniform $v = K \sin(\bar{\varepsilon}) \approx 1.7 \times 10^{-6}$ to the eccentricity balance, independent of its mass and distance. Random ± in-phase/anti-phase aggregation across $N \approx 625$ such bodies gives $\sigma \approx 4.3 \times 10^{-5}$, matching the observed residual. The relevant population is sub-200 km low-eccentricity classical-belt KBOs, where the body's actual oscillation amplitude approximates the Law-4 intrinsic prediction (no resonance pumping). Named TNOs (Pluto, Eris, Haumea, Sedna, etc.) are *not* part of this aggregation: their actual e_{amp} values are dominated by external forcing (Neptune resonance, scattering, galactic tides), not by intrinsic Law-4 dynamics, and their individual v contributions run 10–40× larger than $K \sin(\bar{\varepsilon})$. For Pluto specifically, long-term numerical integrations give actual $e_{\text{amp}} \approx 0.025$, whereas Law 4's intrinsic prediction is ~0.001 — a 1:24 intrinsic-to-external split, with Law 4 correctly capturing the intrinsic baseline while Neptune's 3:2 mean-motion resonance pumps the amplitude up by ~25×.

(ii) Mass uncertainty (~4% of the residual). Uranus and Neptune masses are currently constrained only by Voyager 2 flybys (relative uncertainties $\sim 5 \times 10^{-4}$); the other six are known to 10^{-6}–10^{-8} from orbiters and ranging. A 10^5-trial Monte Carlo perturbation of each planet's mass within its 1σ uncertainty gives a combined $\sigma \approx 1.5 \times 10^{-6}$ contribution to the Law-5 gap, dominated almost entirely by Uranus (which carries 37% of the in-phase v).

Testable predictions. (a) The Vera Rubin Observatory (LSST, 2025–2035) is expected to constrain rotation poles for $\sim 10^3$ small TNOs. A statistical clustering of small classical-belt KBO obliquities near $\arcsin(K \sqrt{d}\, a^{-3/2} \sqrt{m}/e)$ would empirically support the bidirectional reading of Law 4 beyond the eight planets. (b) A future Uranus or Neptune orbiter (e.g., NASA's proposed Uranus Orbiter and Probe, target launch ~2032) would shrink the mass-uncertainty channel by ~100×, leaving the bulk of the residual (the minor-body signature) largely intact — discriminating the two channels in the budget.

Law-4 closure as a quantitative criterion for planethood. The pattern of which bodies satisfy Law-4 closure (actual $e_{\mathrm{amp}} \approx$ intrinsic Law-4 prediction) and which are externally dominated maps onto the IAU's 2006 third criterion: *has cleared the neighborhood around its orbit*. Bodies that have cleared their neighborhood evolve under their own dynamics — their secular e_{amp} is set intrinsically by Law 4. Bodies that have not (Pluto and the plutinos, scattered-disk objects, Sedna, comets, asteroids) have their secular evolution dominated by external coupling, exactly as the IAU criterion implies. The two formalisations partition the same eight bodies. The IAU's third criterion has long been criticised for being qualitative; Soter (2006) proposed a mass-discriminant Λ to formalise it, but Λ never became canonical. Law-4 closure provides a different quantitative formalisation — *does the body's secular e_{amp} close under K with $\sin(\bar{\varepsilon}) \leq 1$ using only its own (m, a, d)?* — that returns a clean pass/fail and matches the same 8-body partition. The agreement is not tautological: all proposed Planet Nine candidates fail Law-4 closure by 4–7 orders of magnitude independent of how the observed eccentricity is interpreted, making Law-4 closure a predictive criterion rather than a post-hoc relabelling.

Saturn from Law 5 alone. Law 5 derives Saturn's eccentricity from the global balance equation involving all eight planets simultaneously: $e_{\mathrm{Saturn}} = 0.05372$ (predicted from the other seven planets; −0.27% from the model midpoint of 0.05387). Saturn's eccentricity oscillates secularly between ~0.01 and ~0.09 — a factor-of-9 dynamic range — and is the only planetary eccentricity currently derivable from the model. The Fibonacci divisors were originally chosen to match precession periods (Law 1) and inclination balance (Law 3); the Saturn eccentricity prediction was never optimized for. Predicting the remaining seven *base* eccentricities (Law 4 currently covers oscillation amplitudes only) is open work for a future extension.

6. Law 6: Saturn-Jupiter-Earth Resonance

Earth's only intrinsic precessional motion is its axial precession ($H/13$), driven by the lunisolar torque on its equatorial bulge; obliquity, eccentricity, and climatic precession are not intrinsic but planetary coupling beats dominated by Jupiter and Saturn. The core of this law is an exact structural balance, not a coincidence: Jupiter's ICRF perihelion period and Saturn's ecliptic perihelion period lock to a single integer divisor of the $8H$ lattice, $8H/65 \approx 41,270$ yr at the J2000 anchor — the obliquity beat recorded in Earth's climate. Earth's own obliquity sits one lattice integer away at the Fibonacci value $H/8$ (= $8H/64$), because obliquity is Earth's axial precession beating against the precession of the ecliptic plane: against the gas giants' actual ecliptic period $8H/39$ the beat is $8H/65$, while against Law 1's Fibonacci anchor $H/5$ it is $H/8$. The integers 64 and 65 (and their ~41-kyr separation) are invariant at any epoch under section 11; the literal "41,270 yr" value is a J2000 snapshot that rescales smoothly at geological time. The gas giants drive Earth's spin-axis dynamics through their mutual resonance lock.

Each cycle in this law carries two compatible attributions: a *Fibonacci anchor* — the integer divisor of H that fixes Earth's cycle hierarchy (Law 1) — and an *8H-lattice value* — an Earth-frame beat produced by the N-body coupling as seen in Earth's frames at J2000 (the Laskar matches of this law are against $|s_3|$ and $k + s_3$, not against Jupiter's or Saturn's own secular frequencies g_5, g_6). For Earth's own anchors the two coincide exactly. For Jupiter's and Saturn's perihelion motions they differ by one lattice integer (~1.5–2.6%). Saturn's anti-phase role (its cosine sign flipped relative to the other seven planets) makes it the natural pivot for both balance laws (Laws 3 and 5); the Fibonacci-clean anchors that position Jupiter and Saturn here are Earth's own ecliptic precession ($H/5$) and obliquity ($H/8$), with the planets' 8H-lattice values landing one lattice integer away.

6.1 Dynamical Refinement: the Secular Periods at $8H/65$

The 8H-lattice secular periods produced by the actual gas-giant gravitational coupling on Earth's orbital plane sit one lattice integer off the Fibonacci anchors:

Table 7: Fibonacci anchors vs. 8H-lattice secular periods

Quantity	Fibonacci anchor	8H-lattice secular
Jupiter perihelion ecliptic	$+H/5 = \sim 67,063$ yr	$+8H/39 = 68,783$ yr
Jupiter perihelion ICRF	$-H/8 = \sim 41,915$ yr	$-8H/65 = 41,270$ yr
Saturn perihelion ecliptic	$-H/8 = \sim 41,915$ yr	$-8H/65 = 41,270$ yr
Saturn perihelion ICRF	$-H/21 = 15,967$ yr	$-8H/169 = 15,873$ yr

Two structural facts survive the refinement. First, **Jupiter's ICRF perihelion and Saturn's ecliptic perihelion coincide exactly at $8H/65 = 41,270$ yr** — the period at which they drive Earth's obliquity (the climate-recorded $k + s_3$ beat). Both gas giants carry a perihelion motion at this period, in different reference frames. Earth's own obliquity is the Fibonacci $H/8 = 8H/64$, one lattice step off. Second, Earth's nodal precession — driven by the same Jupiter+Saturn torque — sits at $8H/39 = 68,783$ yr.

Why the single-integer offset. Earth's obliquity is the beat of its axial precession against the precession of the ecliptic plane: in $8H$-integer terms, 104 (axial, $H/13$) minus the ecliptic integer. With Law 1's ecliptic anchor $H/5 = 40$, the beat is $104 - 40 = 64 \to H/8$; with the gas giants' actual ecliptic period $8H/39$, it is $104 - 39 = 65 \to 8H/65$. The single-integer shift in the ecliptic period propagates one-for-one into the obliquity beat.

Seen on the $8H$ lattice, the four periods order as $39 < 40 < 64 < 65$: Jupiter ecliptic perihelion ($8H/39$), Earth ecliptic precession ($8H/40 = H/5$), Earth obliquity ($8H/64 = H/8$), and Saturn ecliptic perihelion ($8H/65$). Earth's two Fibonacci values each sit exactly one $8H$-step off a gas-giant period: its ecliptic precession just *below* Jupiter's, its obliquity just *above* Saturn's. The two gas giants move in opposite senses and drive Earth's orbital plane from both sides; the clean Fibonacci anchors are the balance point between them.

Independent cross-validation. These periods are derived analytically from the Fibonacci architecture and the gas-giant coupling; they are not fitted to any external solution. Laskar et al. (2004)'s numerical secular theory, computed independently from the full Laplace–Lagrange eigensystem, places Earth's nodal eigenmode at $|s_3| = 68,750$ yr and the obliquity beat at $k + s_3 = 41,220$ yr. The analytical and numerical values agree to 0.04% and 0.12% respectively, and the empirical LR04 obliquity peak (40,950 yr from a fine-grid spectral sweep) lands within one Rayleigh element of both. The convergence is not a calibration: neither method consults the other.

6.2 Saturn's Ecliptic-Retrograde Perihelion Precession

JPL's WebGeoCalc tool — which computes geometric quantities directly from the SPICE ephemeris kernels — shows that Saturn's longitude of perihelion ($\varpi = \Omega + \omega$) is **decreasing** over 1900–2000 AD at approximately $-3,400''$/cy. The ascending node regresses faster than the argument of perihelion advances, producing a net retrograde motion. The JPL Keplerian elements table (Standish & Williams, 1992) confirms $\mathrm{d}\varpi/\mathrm{d}t = -0.419°$/cy in the 1800–2050 fit — the only gas giant with a negative rate.

The standard explanation: the Great Inequality. Standard celestial mechanics attributes this to a transient phase of the Great Inequality — the ~900-year oscillation from the near-5:2 mean-motion resonance of Jupiter and Saturn. The history: Kepler first noticed positional discrepancies (~1625); Halley quantified the drift (~1695); Euler and Lagrange failed to explain it (1748, 1766); Laplace solved it in 1784–1786, showing it was periodic, not secular (Wilson, 1985). Under this theory, the long-term secular rate is prograde at $\sim +19.5''$/yr, dominated by $g_6 = 28.245''$/yr, and the current retrograde motion is a temporary oscillation.

Why the standard explanation is incomplete. (1) No complete 900-year cycle of Saturn's *perihelion* precession has ever been observed; the Great Inequality was derived from mean longitude, not ϖ. (2) The observed rate ($\sim -3,400''$/cy) differs from the predicted secular rate (+1,950″/cy) by ~5,350″/cy with opposite sign. (3) Iorio (2009) showed that no standard physics — not planetary perturbations, solar oblateness, asteroid belt mass, trans-Neptunian objects, general relativity, or modified gravity — can explain even a tiny retrograde residual detected in EPM2008 (−6 ± 2 mas/cy).

The model's statement. Saturn's perihelion moves ecliptic-retrograde throughout the observed era, and the model carries that motion on the $-8H/65$ descriptor (Fibonacci anchor $-H/8$); the model's own N-body engine confirms the standard mechanism — the retrograde is the window phase of the Great-Inequality epicycle, with the long-term secular mean prograde (g_6) — so $-8H/65$ is a *window-epoch descriptor*, exact for the era and quantity it names. At J2000, the heliocentric rate is $360°/41,270 \approx -3,140.3''$/cy; adding the missing advance of perihelion ($\sim -280''$/cy) gives a geocentric rate of $\sim -3,422''$/cy, matching the observed $\sim -3,400''$/cy. This ecliptic-retrograde motion is what makes Saturn the unique pivot for the 7-vs-1 balance (Laws 3 and 5).

Table 8: Saturn's perihelion: the two readings and their resolution

Aspect	Great Inequality	Holistic Model
Direction	Prograde (+19.5″/yr long-term secular, heliocentric ecliptic)	Ecliptic-retrograde (−31.4″/yr, heliocentric ecliptic-of-J2000; the geocentric observed rate is the next row)
Current ecliptic-retrograde	Transient (~900-yr phase)	Window-era motion carried by the $-8H/65$ descriptor; the model's own N-body confirms the transient mechanism (long-term mean prograde, g_6)
WebGeoCalc match ($\sim -3,400''$/cy)	Requires large GI amplitude in ϖ	$\sim -3,422''$/cy (geocentric)
Saturn's role	Same as other planets	Anti-phase pivot (Laws 3, 5, 6)
Resolution	**Rate reverses within ~450 yr**	**Originally predicted permanently retrograde; RETIRED — the model's own N-body agrees the rate reverses on the Great-Inequality flank**

The two theories make a decisive, testable prediction: over decades to centuries of continued high-precision ephemeris tracking, Saturn's $\mathrm{d}\varpi/\mathrm{d}t$ should either show curvature toward zero (Great Inequality) or remain steady near −3,140 to $-3,400''$/cy (this model).

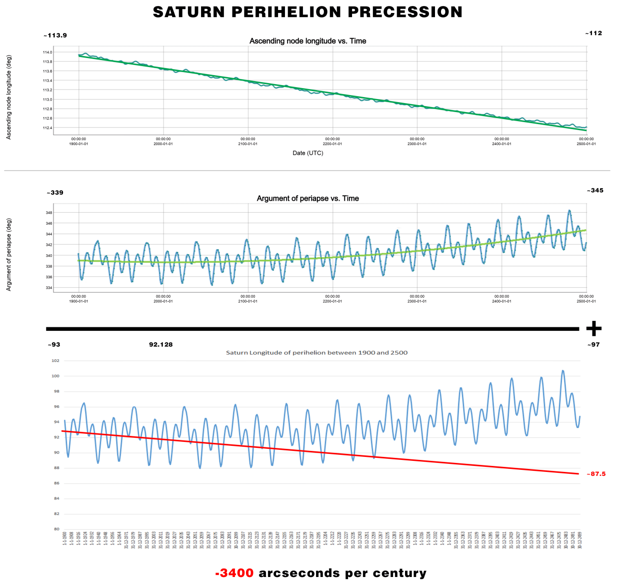

Figure 6: Saturn's perihelion precession decomposed from JPL WebGeoCalc (1900–2500 AD). **Top**: Ascending node longitude (Ω) decreases smoothly (retrograde). **Middle**: Argument of periapse (ω) oscillates with the ~900-year Great Inequality. **Bottom**: Their sum $\varpi = \Omega + \omega$ shows a net retrograde trend; the 1900–2000 slope is $\sim -3,400''$/cy (red line). The prograde-vs-retrograde debate concerns ϖ, not ω: ω itself *advances* (middle panel — it oscillates with the Great Inequality about an advancing trend), and the net retrogradation enters ϖ through Ω regressing faster than ω advances (top panel). Standard secular theory requires all g-eigenfrequencies to be positive (prograde), so the observed retrograde ϖ trend must be attributed to the Great Inequality; the model carries ϖ ecliptic-retrograde on the integer $-8H/65$ (the absolute arcsec/cy rate scales with $H(t)$ per section 11).

6.3 The ICRF Perspective: A Fibonacci Chain

The model is formulated in the ecliptic frame — the natural frame for solar system dynamics. Secular perturbation theory, the Laplace–Lagrange eigensystem, and angular momentum conservation all operate in this plane; the planetary precession rates emerge from mutual gravitational interactions within it. The ICRF (International Celestial Reference Frame), fixed to distant quasars, provides an inertial reference, but no physical mechanism couples the solar system's internal precession to that external frame. The ICRF rates therefore follow from the ecliptic dynamics expressed in a different reference frame, not from an independent constraint.

Viewing the same motions from the ICRF reveals a deeper Fibonacci structure. **In the ICRF, only Earth precesses prograde.** Earth's ecliptic apsidal rate ($H/16 \approx 61.840''$/yr) is the only one that exceeds the general precession of the equinoxes ($H/13 \approx 50.245''$/yr). All other planets — including Jupiter — precess retrograde in the ICRF. The frame transformation subtracts the general precession uniformly:

$$\text{ICRF rate} = \text{ecliptic rate} - H/13 \tag{14}$$

For Earth, $16-13 = 3$ closes a Fibonacci identity and gives its prograde ICRF perihelion $+H/3$. For Jupiter and Saturn, the Fibonacci anchors would give $-H/8$ and $-H/21$, but

Table 9: Perihelion precession: ecliptic vs. ICRF frame (all planets). ICRF rate = ecliptic rate $-H/13$. Bold rows highlight the planets discussed in the text: Venus (ecliptic-retrograde) and the Law 6 chain (Earth, Jupiter, Saturn). At the Fibonacci-*anchor* level the Law 6 chain has pure Fibonacci ICRF denominators (3, 8, 21); in the 8H-lattice secular values shown here only Earth's ($+H/3$) remains exactly Fibonacci.

Planet	Ecliptic H/n	Period (yr)	Dir.	ICRF H/n	Period (yr)	Dir.
Mercury	8H/11	243,867	prograde	$-8H/93$	28,844	retrograde
Venus	**–8H/6**	**447,089**	**retrograde**	$-8H/110$	24,387	retrograde
Earth	**H/16**	**~20,957**	**prograde**	**+H/3**	**~111,772**	**prograde**
Mars	8H/36	74,515	prograde	$-8H/68$	39,449	retrograde
Jupiter	**8H/39**	**68,783**	**prograde**	**–8H/65**	**41,270**	**retrograde**
Saturn	**–8H/65**	**41,270**	**retrograde**	**–8H/169**	**15,873**	**retrograde**
Uranus	H/3	~111,772	prograde	$-H/10$	33,532	retrograde
Neptune	2H	670,634	prograde	$-2H/25$	26,825	retrograde

their actual secular ICRF periods are $-8H/65$ and $-8H/169$ (one lattice integer off; see Table 7). Earth is the sole prograde planet in the ICRF (Figure 3c) — an exception created by the Fibonacci number $H/13$ (the general precession). At the Fibonacci-anchor level all three Law 6 planets have pure Fibonacci ICRF denominators (3, 8, 21); under the 8H-lattice secular refinement only Earth's denominator stays exactly Fibonacci (3), consistent with Jupiter and Saturn carrying ~85% of the solar system's angular momentum and having their own secular periods that do not land exactly on the Earth-anchored Fibonacci lattice.

Alongside the subtraction identity in Equation 14, the Fibonacci-anchor ICRF denominators also satisfy Fibonacci *addition* identities:

- Earth ICRF apsidal (3) + Ecliptic Precession (5) = Jupiter ICRF (8)
- Ecliptic Precession (5) + Jupiter ICRF (8) = general precession (13)
- Jupiter ICRF (8) + general precession (13) = Saturn ICRF (21)

The complete Fibonacci chain $3 \to 5 \to 8 \to 13 \to 21$ thus appears twice: once through subtraction of general precession from ecliptic rates, and once through addition across ICRF rates. The Ecliptic Precession ($H/5$) serves as the bridge between the two frames.

6.4 Extending the Framework to All Planets

The Fibonacci framework extends beyond perihelion precession to axial precession and obliquity cycles for all planets.

Table 10: Axial precession periods expressed in H

Planet	H expression	Period	Dir.	Observed / Theory	Source
Mercury	$8H/9$	298,060 yr	retro	~300 kyr (Cassini)	Peale 2005
Venus	$8H/91$	29,478 yr	pro	~29 kyr	Cottereau & Souchay 2009
Earth	$H/13$	25,794 yr	retro	~25,772 yr	Capitaine et al. 2003
Mars	$H/2 = 8H/16$	167,659 yr	retro	170,400 yr	Kahan et al. 2021
Jupiter	$8H/21$	127,740 yr	retro	113–136 kyr	Saillenfest et al. 2020
Saturn	$4H/3 = 8H/6$	447,089 yr	retro	400–480 kyr	Saillenfest et al. 2021
Uranus	$H \times 610$	~204 Myr	pro	~40–50 Myr	Saillenfest et al. 2022
Neptune	$H \times 68$	~22.8 Myr	retro	~70 Myr (est.)	Rogoszinski & Hamilton 2020

Mercury's $8H/9$ coincides with its ascending-node period (Cassini state, confirmed by MESSENGER). Jupiter's $8H/21$ uses $F_6/F_8 = 8/21$, a clean Fibonacci ratio. Mars ($H/2 = 8H/16$) matches the InSight measurement to 1.7%. Uranus and Neptune have extremely slow axial precession (~40–200 Myr), with large observational uncertainties.

Obliquity cycles. The Fibonacci decomposition that produces Earth's obliquity cycle ($H/8$ from the identity $3{+}5 = 8$) extends to all planets where the perihelion ecliptic rate numerator can be Fibonacci-decomposed. Three obliquity cycles are confirmed by observation; three remain as testable predictions:

Table 11: Obliquity cycle predictions. All period values are J2000-anchor; the integer divisors of H and $8H$ are invariant at any epoch under section 11.

Planet	Predicted	Observed / Theory	Status	Source
Mercury	$8H/3 = 894,179$ yr	~895,000 yr	0.2%	Bills & Comstock 2005
Earth	$H/8 = {\sim}41,915$ yr	~41, 040 yr	2%	Laskar et al. 1993
Mars	$8H/21 = 127,740$ yr	~124,800 yr	2.4%	Laskar et al. 2004
Jupiter	$H/2 = 167,659$ yr	no regular cycle	prediction	Saillenfest et al. 2020
Saturn	$H/3 = 111,772$ yr	no regular cycle	prediction	Saillenfest et al. 2021
Uranus	$H/2 = 167,659$ yr	frozen at ~98°	prediction	Saillenfest et al. 2022

Venus and Neptune have obliquity cycle = |ICRF perihelion period| (auto-derived from their ecliptic periods; tidally damped). In the two-component formula (Equation 15), the inclination and obliquity terms are at the same frequency and cancel exactly, producing constant obliquity — consistent with observations (Venus tidally damped at 177°, Neptune frozen at ~28°).

Universal two-component formula. Every planet with an obliquity cycle follows the same two-component structure as Earth (Earth's formula derivation in subsection 9.1), with one cosine term at the ICRF perihelion period (inclination component) and one at the obliquity cycle period (obliquity component), both with amplitude $A_p = \psi/(d_p \times \sqrt{m_p})$ from Law 2:

$$\begin{aligned} \varepsilon_p(t) = \varepsilon_{p,\mathrm{J2000}} \\ - A_p[\cos(\omega_i t) - \cos(\omega_i t_{2000})] \\ + A_p[\cos(\omega_o t) - \cos(\omega_o t_{2000})] \end{aligned} \tag{15}$$

where $\omega_i = 2\pi/T_{\mathrm{ICRF}}$ and $\omega_o = 2\pi/T_{\mathrm{obliq}}$. The anchoring offsets ensure $\varepsilon_p(2000) = \varepsilon_{p,\mathrm{J2000}}$ exactly.

The time-averaged obliquity over $8H$ differs from the J2000 snapshot because the cosine terms average to zero, leaving only the constant anchoring offsets:

$$\bar{\varepsilon}_p = \varepsilon_{p,\mathrm{J2000}} + A_p \cos(\omega_i t_{2000}) - A_p \cos(\omega_o t_{2000}) \tag{16}$$

Table 12: Mean obliquity (analytical, averaged over $8H$)

Planet	J2000 (°)	Mean (°)	Shift (°)
Mercury	0.03	0.01	−0.02
Venus	2.64	2.64	—
Earth	23.44	23.41353	−0.03
Mars	25.19	25.32	+0.21
Jupiter	3.13	3.12	−0.01
Saturn	26.73	26.80	+0.07
Uranus	82.23	82.24	+0.01
Neptune	28.32	28.32	—

The formula midpoint remains close to the J2000 snapshot for every planet (within ±0.2°). Mars's midpoint differs by 0.21°; Mercury, Jupiter, Saturn, and Uranus all sit within 0.1°. Cross-planet connections emerge: Mars's obliquity cycle equals Jupiter's axial precession ($8H/21$, where $21 = F_8$).

Eccentricity cycles. Each planet's eccentricity cycle is the meeting frequency of its axial precession and its perihelion precession in the ICRF — the same derivation that produces Earth's $H/16$ beat. Earth is the family's exception: that beat ($13 + 3 = 16$, the ~20,957 yr perihelion precession) is the perihelion-*direction* cycle only, and Earth's eccentricity magnitude oscillates on the $H/3$ line of subsection 14.8, which the table lists:

Table 13: Eccentricity cycles from axial–perihelion meeting frequencies. All period values are J2000-anchor snapshots; the structural H/N identities are invariant at any epoch under section 11.

Planet	Axial dir.	Peri ICRF dir.	H expression	Period
Mercury	retro	retro	2H/21	31,935 yr
Venus	pro	retro	8H/19	141,186 yr
Earth	**retro**	**pro**	**H/3** (beat $H/16$ = direction only)	**~111,772 yr**
Mars	retro	retro	8H/52	51,587 yr
Jupiter	retro	retro	8H/44	60,967 yr
Saturn	retro	retro	8H/163	16,457 yr
Uranus	pro	retro	≈H/10	33,532 yr
Neptune	retro	retro	≈2H/25	26,825 yr

When axial and perihelion ICRF precessions move in opposite directions (Earth, Venus, Uranus), their rates add; when in the same direction, the rates subtract. For Uranus and Neptune the extremely slow axial precession makes their eccentricity cycle approximately equal to the perihelion ICRF period.

6.5 Ascending Node Periods: Integer Divisors of $8H$

Each planet's ascending node regression period takes the form $T_\Omega = 8H/N$ for an integer N. The seven fitted planets' integers are jointly fit to the JPL J2000-fixed-frame ascending-node trends (Earth's node is the structural $-H/5$, not fitted), with Jupiter and Saturn locked to a shared $N = 36$ to keep the gas-giant pair from drifting apart in long-term integration.

Table 14: Ascending node periods as integer divisors of $8H$

Planet	Period	Note
Mercury	$-8H/9$	
Venus	$-8H/1$	full $8H$ cycle
Earth	$-H/5 = -8H/40$	ecliptic precession (special)
Mars	$-8H/64$	
Jupiter	$-8H/36$	locked with Saturn
Saturn	$-8H/36$	locked with Jupiter
Uranus	$-8H/11$	
Neptune	$-8H/3$	

Across all 7 fitted planets, the $8H/N$ integers reproduce JPL's J2000-fixed-frame ascending-node trends with a cumulative residual error of ~5.8″/century (≈0.8″/century per planet). The structural claim is that each planet's ascending-node period is an integer divisor of a single Earth Fundamental Cycle-derived super-period $8H$ — all seven $8H/N$ integers derive from one constant. Under section 11, these integer divisors are invariant at any epoch while the literal $8H$ value rescales smoothly at geological time.

Earth as a special case. Earth's ascending node period of $-H/5 = -8H/40 =$ ~67,063 years is the ecliptic precession rate and reflects its unique structural role as the planet defining the ecliptic frame. The negative sign indicates retrograde precession on the invariable plane. The ecliptic precession rate $H/5$ is itself a derived quantity from the general precession ($H/13$) and the obliquity cycle ($H/8$): $1/(H/13) - 1/(H/8) = 1/(H/5)$ closes the Fibonacci identity $13 - 8 = 5$, embedding Earth's ascending node into the same Fibonacci hierarchy.

Jupiter–Saturn lockstep. Allowing Jupiter and Saturn to drift independently makes the gas-giant pair separate in long-term integration, breaking the gas-giant coupling of Law 6; the shared N is therefore a structural constraint of the joint model, not a coincidence.

Observability limitation. These ascending node periods describe motion over 50,000–2,000,000-year timescales. With only ~4,000 years of recorded astronomy, the periods cannot be observationally verified by direct observation of a complete cycle. The model's contribution is the structural derivation: all seven periods derive from a single constant (H) and a single super-period ($8H$).

7. Physical Origin: Formation-Epoch Freezing

KAM theory (section 2) explains why Fibonacci ratios are *preferred*. This section presents evidence that the observed precision — 99.9974% inclination balance (Law 3) and 99.8636% eccentricity balance (Law 5) — originates from the solar system's formation epoch.

7.1 The Three-Phase Mechanism

Phase 1 — Protoplanetary disk (0–10 Myr): Planets form and migrate within a gas disk. Dissipative forces — gas drag, disk torques, tidal interactions — continuously push orbits toward configurations that minimize the Angular Momentum Deficit (AMD), the conserved quantity governing long-term stability (Laskar, 1997).

Phase 2 — KAM selection: Among all AMD-minimizing configurations, those organized by Fibonacci ratios have the widest stability margins (KAM theory). Dissipative evolution therefore preferentially *converges toward Fibonacci-organized configurations* — not because Fibonacci is imposed, but because Fibonacci configurations are the deepest stability wells in the energy landscape.

Phase 3 — Disk dissipation (~3–10 Myr): When the gas disk dissipates, the dissipative mechanism shuts off. The Fibonacci configuration is *frozen* — like a ball settling into the deepest valley and then the landscape hardening around it. 4.5 billion years of conservative Hamiltonian dynamics have preserved the architecture because KAM tori protect it against perturbation.

7.2 Hierarchy of Certainty

Not all claims carry equal evidence:

Table 15: Hierarchy of certainty

Claim	Evidence	Status
Fibonacci structure in orbital architecture	$p \leq 1.5 \times 10^{-4}$ (≈ $3.62\,\sigma$)	Established
Structure acts on AMD-natural variables	0.11% vs > 28% spread	Established
KAM provides mathematical foundation	Proven theorem	Established
Structure frozen at formation	N-body: no mode preserves it	Well-supported

The *existence* of non-trivial Fibonacci structure beyond chance is supported at 3.62–$4.75\,\sigma$ (section 8). The *mechanism* — KAM theory selecting golden-ratio-compatible orbits, frozen at formation — is well-supported. The *specific* *values* ($H = 335,317$, ψ, K) are empirically determined and not yet derived from first principles.

7.3 Three Fibonacci Levels

The Fibonacci structure operates at three distinct, nested levels — each independently observable:

Level 1 — Fibonacci d-values (Laws 2–5): Each planet is assigned a Fibonacci number $d \in \{3, 5, 21, 34\}$ that determines its inclination amplitude through $A = \psi/(d\sqrt{m})$. The eight d-values form mirror-symmetric pairs across the asteroid belt. This level determines the *scalar balance* (Laws 3 and 5) — the genuine constraint that, with mirror symmetry, selects the unique configuration (subsection 4.4).

Level 2 — ICRF perihelion periods are H/Fibonacci-related (Law 1): Earth's major precession periods divide the Earth Fundamental Cycle by Fibonacci-related divisors: $H/3$, $H/5$, $H/8$, $H/13$, and the derived $H/16 = H/(13+3)$. The Fibonacci addition rule applies as a beat-frequency identity: e.g. Earth's inclination and ecliptic precession beat to its obliquity cycle, $1/(H/3) + 1/(H/5) = 1/(H/8)$ (subsection 9.8).

Level 3 — Ascending-node periods are $8H/N$: The ascending node regression rates are integer divisors of the Solar System Resonance Cycle ($8H$), with Jupiter and Saturn locked to a shared $N = 36$, reproducing JPL trends to $\sim 5.8''$/century cumulatively across 7 fitted planets (subsection 6.5).

The three levels are nested: d-values (Level 1) determine the amplitudes, H/Fibonacci periods (Level 2) determine the dominant precession rates, and $8H/N$ eigenfrequencies (Level 3) determine the secular ascending node motion. Each level is independently observable, and each agrees with measurement.

7.4 Action-Angle Closure for the $8H$ Climate Lattice

KAM theory and the three-phase formation freezing of section 7 explain why *planetary spacing* (Laws 1–5) sits at Fibonacci-stable configurations. They do not, on their own, explain why the framework's *climate lattice* — the Solar System Resonance Cycle $8H$ and the 33 integer divisors $8H/N$ used in the canonical Climate Formula of section 10 — is the specific structure picked out by Earth's paleoclimate spectrum. The two are distinct claims at distinct scales. The mechanism behind the climate lattice is **action-angle closure** of the secular dynamics in the obliquity sector. The Chirikov-KAM resonance-overlap mechanism, the natural first hypothesis, returns null.

Chirikov-KAM resonance overlap was the wrong mechanism. The first hypothesis was that $8H/N$ integers mark the surviving KAM-stable spectral structure — positions that sit in gaps between overlapping resonance widths (Chirikov's criterion (Chirikov, 1979)). The empirical test was null. Across 33 spectral peaks identified by Welch PSD in the LA2004 51-Myr eccentricity and obliquity solutions, every peak is KAM-stable — sharp spectral peaks already imply quasi-periodic dynamics, by construction. Lattice-aligned peaks have median Chirikov $K = 0.584$; non-lattice peaks have median $K = 0.516$. The difference is not significant (Mann-Whitney $p = 0.667$), and the sign is opposite to the KAM-overlap hypothesis prediction. KAM stability is necessary but not sufficient: $8H$-lattice positions sit in the stable manifold, but the stable manifold contains substantially more than the $8H$ lattice.

Action-angle closure is the mechanism. If $8H = 2,682,536$ yr is a true closed-orbit period of the secular system, then in action-angle coordinates the obliquity trajectory should return to its starting point every $8H$, and the obliquity eigenfrequencies should be integer multiples of $1/(8H)$. Three pre-registered tests on LA2004 51-Myr data confirm this — strikingly, in the obliquity sector only:

- The closure distance $D(8H)$ for the obliquity time series is in the top 2.5% of all random non-$8H$ lags (whereas the closure distance for the eccentricity vector $(h, k) = (e \sin \varpi, e \cos \varpi)$ is beaten by 57.5% of random lags — null).
- Of the top 10 obliquity spectral peaks, **8 of 10 fall within 5% of integer divisors of $1/(8H)$, most within 0.2%** (whereas only 6 of 10 eccentricity peaks satisfy this criterion).

The asymmetry is internally consistent. The previously documented Test C-Invariant result — that 100% of LA2004 obliquity power and only 74% of LA2004 eccentricity power lies on the lattice (section 10 and Table 29) — shows the same channel split. The off-lattice 26% eccentricity power is the spectral signature of Mercury-chaos-driven secular perturbation (Laskar, 1989), which breaks closure for the eccentricity vector but not for the obliquity sector.

Why this forces integer divisibility of the lattice. If $8H$ is the closed-orbit period and the eigenfrequencies are commensurate at this period, then each eigenfrequency must take the form $n/(8H)$ for some integer n. The spectrum is *forced* onto integer divisors of $8H$ — conservation, not coincidence. The 33-integer L1 set used in the Climate Formula is a specific subset of those integers, selected on a separate climate-activity criterion within an already-quantized set. Integer divisibility itself is automatic once action-angle periodicity is established.

KAM and action-angle closure operate on different scales and do not compete. KAM tori protect the architecture at the planetary-spacing level (Laws 1–5, the Fibonacci-stable ratios of section 2); action-angle closure forces the secular spectrum at the climate-lattice level ($8H/N$ integer divisors used in section 10). Both mechanisms persist as the lattice evolves in time — the integer labels stay invariant while the absolute periods rescale — which is the structural claim of section 11.

8. Statistical Significance and Exoplanet Evidence

8.1 11 Tests, Three Null Distributions

To address concerns first raised by Backus (1969) about Fibonacci structure in planetary systems, a comprehensive significance analysis was performed using 11 test statistics covering all 6 laws plus four findings. Each was evaluated against three independent null distributions:

- **Permutation** (exhaustive $8! = 40,320$ trials): same values, randomly reassigned to planets.
- **Log-uniform Monte Carlo** (10^6 trials): random eccentricities and amplitudes from physical ranges, random d-

values from Fibonacci sets, random period denominators, random year-length ratios.

- **Uniform Monte Carlo** (10^6 trials): same ranges, flat distribution.

Of the 11 tests, 4 are genuinely *empirical* under the permutation null (Laws 3, 5; Findings 4 and 6) and 9 are combinable under the Monte Carlo nulls (the empirical set plus Laws 1, 6; Findings 1, 1b; year-length beat, which become meaningful when the null draws random d-assignments, random period denominators, and random year lengths). Two tests — Laws 2 and 4 — are tautological by construction (the model defines the amplitude relations to hold identically) and are excluded from every combined statistic, reported only as internal-consistency checks; see the footnotes of Table 16 for the full classification.

The 4 empirical tests are not statistically independent — all four use the same fundamental quantity $v_j = \sqrt{m_j}\, a_j^{3/2}\, e_j / \sqrt{d_j}$ — so older combining methods (Fisher's, Stouffer's+Brown) must absorb a correlation penalty. The direct joint test used here avoids the approximation by computing the combined statistic's null distribution directly (Table 16).

Headline statistic: direct joint permutation test. Each empirical test's raw statistic is studentized against the null mean and standard deviation computed across all 8! permutations; the four studentized z-scores are summed into a single combined statistic $T = \sum_i z_i$; and the p-value is the fraction of null permutations with $T_{\text{null}} \geq T_{\text{obs}}$.

This approach is model-independent (no Gaussian or χ^2 assumption), self-correcting for correlation (because the joint null is computed from the same shared permutation that generates the correlation, no explicit variance-inflation factor is needed — the correlation is baked into the null by construction), and has no floor-clamp artifact ($p \geq 1/(n+1)$ by construction). For reference, the *measured* average pairwise correlation between the four tests under the permutation null is $\bar{r} = 0.283$ (replacing an earlier estimate of $\bar{r} \approx 0.5$ that proved too conservative). Under the MC nulls the measured correlation is much smaller ($\bar{r} \approx 0.032$) because random d-assignments break the shared v_j dependency.

All 4 empirical tests reach $p < 0.01$ in the permutation null, and all 9 MC-combinable tests reach $p < 0.05$ in both Monte Carlo nulls. The joint combined p-value is robust across the three null distributions and lands in a tight range:

$$
\begin{aligned}
p_{\text{joint, perm.}} &= 1.5 \times 10^{-4} && \approx 3.62\,\sigma \\
p_{\text{joint, log-u. MC}} &= 1.0 \times 10^{-6} && \approx 4.75\,\sigma \\
p_{\text{joint, unif. MC}} &= 1.0 \times 10^{-6} && \approx 4.75\,\sigma.
\end{aligned}
\tag{17}
$$

The permutation result ($\approx 3.62\,\sigma$) is the most defensive figure — it conditions on the actual values and tests only the planet-to-value assignment, making no assumptions about what counts as a "random" planetary system. The Monte Carlo nulls test the more general question of whether fully randomised systems would reproduce the patterns, and give a stronger answer ($\approx 4.75\,\sigma$). The two MC nulls agree to within $0.01\,\sigma$, indicating complete insensitivity to the choice between log-uniform and uniform sampling. The headline comfortably exceeds the conventional 3σ "evidence" threshold across all three null distributions, and the MC results lie just below the particle-physics 5σ "discovery" threshold ($p \approx 3 \times 10^{-7}$).

Table 16: Statistical significance of Fibonacci structure (11 tests)

Test	Observed	Perm.	Log-u.	Unif.
1. Law 1 Fib. denominators‡	7/8	1	2.6e-5	3.0e-5
2. Law 2 ψ full§	0.0000%	1	1	1
3. Law 3 Incl. balance	**99.9974%**	**7.4e-3**	**1.0e-5**	**0.8e-5**
4. Law 4 K amplitude§	0.0000%	1	1	1
5. Law 5 Ecc. balance	**99.8636%**	**7.2e-4**	**3.7e-4**	**3.7e-4**
6. Law 6 E–J–S reson.‡	exact	1	0.032	0.032
7. F1 Mirror symm.‡	4/4	1	1.2e-4	1.5e-4
8. F1b d-set clustering‡	yes	1	0.020	0.020
9. F4 Saturn pred.	**0.27%**	**7.2e-4**	**3.7e-4**	**3.7e-4**
10. F6 Solo planet ID	**0.27%**	**4.0e-3**	**2.8e-3**	**3.1e-3**
11. Year-length beat‡	0.0048%	1	$< \mathbf{10^{-6}}$	$< \mathbf{10^{-6}}$
Joint permutation test (headline)		$\mathbf{1.5 \times 10^{-4}}$	$\mathbf{1.0 \times 10^{-6}}$	$\mathbf{1.0 \times 10^{-6}}$

‡ **Structural / multiset-invariant** (Laws 1, 6; Findings 1, 1b; Year-length beat). Permutation yields $p = 1$ by construction (the multiset of values is preserved under shuffling, or the observation is a single scalar). Under the Monte Carlo nulls the tests *are* meaningful — random d-assignments, random period denominators, and random year lengths produce distinct null distributions — and these five tests are therefore *included* in the MC joint combined statistic.

§ **Tautological by construction** (Laws 2 and 4). The model defines amplitudes as $\psi/(d\sqrt{m})$ and $K\sin(\bar{\varepsilon})\sqrt{d}/(\sqrt{m}a^{3/2})$, so the test relations hold identically under any null. Reported as internal-consistency checks; excluded from every combined statistic.

Headline: direct joint permutation test — studentized combined statistic $T = \sum_i z_i$ over the $k = 4$ empirical tests, $p = \#\{T_{\text{null}} \geq T_{\text{obs}}\}/n$. Under the MC nulls the joint test combines $k = 9$ tests. Model-independent: no Gaussian assumption, no correlation-correction factor (the joint null captures the correlation directly).

Jackknife: robustness to dropping any single planet. A leave-one-out jackknife re-runs the direct joint permutation test (now over 7! = 5,040 permutations) with each planet removed from the system in turn (Table 17). Dropping Jupiter collapses the signal to $\approx 0.5\,\sigma$, and dropping Uranus collapses it to $\approx 0.9\,\sigma$.

Table 17: Leave-one-out jackknife of the direct joint permutation test

Planet dropped	Joint p	Sigma
Mercury	3.2×10^{-2}	$\approx 1.85\,\sigma$
Venus	2.4×10^{-3}	$\approx 2.82\,\sigma$
Earth	3.4×10^{-3}	$\approx 2.71\,\sigma$
Mars	5.0×10^{-3}	$\approx 2.58\,\sigma$
Jupiter	$\mathbf{3.1 \times 10^{-1}}$	$\approx \mathbf{0.49}\,\sigma$
Saturn†	6.6×10^{-2}	$\approx 1.50\,\sigma$
Uranus	$\mathbf{1.9 \times 10^{-1}}$	$\approx \mathbf{0.86}\,\sigma$
Neptune	6.0×10^{-2}	$\approx 1.55\,\sigma$
Full 8-planet suite	$\mathbf{1.5 \times 10^{-4}}$	$\mathbf{3.62}\,\sigma$

† F4 undefined when Saturn is dropped; $k = 3$ tests used.

The pattern matches what the six laws predict: the v_j balance is *global* (each side of the Fibonacci d-ladder must contribute), so the full 3.62 σ requires all eight planets cooperating, with the outer planets (Jupiter, Saturn, Uranus, Neptune) carrying the largest v-weights.

Comparison with supporting approximations. Two older combining methods are retained for transparency but are approximations of the direct joint test:

- **Stouffer's Z with measured $\bar{r}$** (permutation: 1.8×10^{-5}, $\approx 4.1\,\sigma$). Converts each per-test p-value to a one-tailed z and sums with a variance-inflation factor $1 + (k-1)\bar{r}$. Uses the measured correlation $\bar{r} = 0.283$ instead of the previously hard-coded value of 0.5.
- **Fisher's method** (permutation: 8.6×10^{-8}). Combines log-p-values into a χ^2 statistic; highly sensitive to floor-clamping at small p-values. Reported as a cross-check only.

Both give stronger apparent significance than the direct joint test, because both rely on Gaussian/χ^2 distributional assumptions that the direct test avoids. The gap is a useful indicator of how much the approximations contribute versus the raw data.

8.2 Exoplanet Context: A Question for Future Work

Compact multi-planet exoplanet systems raise the question of whether Fibonacci period-ratio patterns appear more broadly. TRAPPIST-1 (Grimm et al., 2018) has 5 of 6 consecutive period ratios near Fibonacci fractions (83%); Kepler-90 has 5 of 7 (71%). These observations are consistent with prior findings that Fibonacci fractions cluster preferentially in orbital period distributions (Pletser, 2019; Aschwanden, 2018).

However, neither system can test the deeper Fibonacci Laws presented here. TRAPPIST-1 is a known mean-motion resonance chain, so Fibonacci-like period ratios are partly a by-product of resonance rather than an independent realization of the same mechanism. Its eccentricities span only ~0.002–0.01 (a factor-of-4 dynamic range, compared with the solar system's 141× range), leaving the inclination and eccentricity balance conditions (Laws 3 and 5) untestable. Kepler-90 has only two mass measurements, which precludes any ξ- or η-based test. The period-ratio observations in these systems are therefore suggestive rather than confirmatory — they motivate future work once more TTV-mass-measured exoplanet systems become available, but they are not used as support for any of the eleven significance tests above, which rest entirely on solar system data.

Formation-epoch resonance for the terrestrial planets. Recent N-body work by Huang et al. (2025) reaches an independent conclusion consistent with the Fibonacci Laws' formation-epoch reading: the inner planets (Venus, proto-Earth, Theia, Mars) were locked in a 2:3:4:6 mean-motion resonance chain during the gas-disk phase, disrupted at ~10 Myr by the Giant Planet Instability. Their headline observational anchor is the present Mars–Venus period ratio of 3.05, which their simulations reproduce as a natural relic of the former chain rather than as a coincidence of late-stage accretion. The mechanisms differ — Huang et al. (2025) invoke gas-disk migration and drag, whereas the Fibonacci Laws rest on KAM optimality — but the observational conclusion converges: today's inner-planet spacing is a formation-epoch resonance signature. The definitional distinction between a *live* mean-motion chain (with actively librating resonance angles, TRAPPIST-1 style) and a *KAM-stabilised quasi-resonance* (proximity to golden-mean ratios without live libration) remains an open observational question that upcoming exoplanet surveys can adjudicate.

Part II: Consequences for Earth

9. Observable Consequences for Earth

The six Fibonacci Laws produce specific, testable consequences for Earth's orbital dynamics. Each of Earth's known precession phenomena emerges from the model's two counter-rotating reference points.

9.1 Obliquity

The model's key structural insight is that observed obliquity is the sum of two oscillating components with equal amplitude:

$$\varepsilon(t) = \bar{\varepsilon} - A\cos\!\left(\frac{2\pi t}{T_{\text{incl}}}\right) + A\cos\!\left(\frac{2\pi t}{T_{\text{obliq}}}\right) \qquad (18)$$

where $\bar{\varepsilon} = 23.41353°$ (mean obliquity), $A = 0.63607°$ (amplitude), $T_{\text{incl}} = H/3 = {\sim}111{,}772$ years (inclination component), and $T_{\text{obliq}} = H/8 = {\sim}41{,}915$ years (obliquity component). The two cosine terms have opposite signs: the inclination component is subtracted while the obliquity component is added. Maximum obliquity occurs when both terms reach their respective extremes such that they add constructively; minimum occurs when they cancel. The dominant visible period is $H/8 \approx {\sim}41{,}915$ years, matching the observed obliquity cycle. Agreement with standard theory is excellent for ±10,000 years; beyond this range, the model predicts bounded oscillation within 22.21°–24.72° while Laskar's polynomial extrapolation diverges (Figure 7).

Table 18: Obliquity: model vs. standard theory

Year	Model	La2004 (Laskar et al., 2004)	Chapront et al. 2002	Diff.
2000 AD	23.4393°	23.4393°	—	0
10,000 BC	24.5294°	24.1592°	24.3053°	~0.37°
10,000 AD	22.6182°	22.6534°	22.6370°	~0.04°

Independent amplitude confirmation. Berger (1978) decomposed obliquity into 47 Fourier terms. The dominant term (frequency $s_3 + k$, period ~41,000 years) has amplitude 0.684° — within 8% of the model's 0.636°. Physically, s_3 is the eigenmode most strongly associated with Earth's orbital plane (precessing retrograde) and k is the axial precession rate (prograde); their beat $s_3 + k$ produces the ~41,915-yr obliquity cycle, matching the model's Fibonacci beat (H/5 ecliptic precession + H/3 inclination precession → H/8 obliquity cycle, via $3 + 5 = 8$). The secondary Fourier terms partially cancel the dominant term, which may account for the 8% gap.

Why equal amplitudes? The model's claim that both obliquity components oscillate by the same amplitude is not

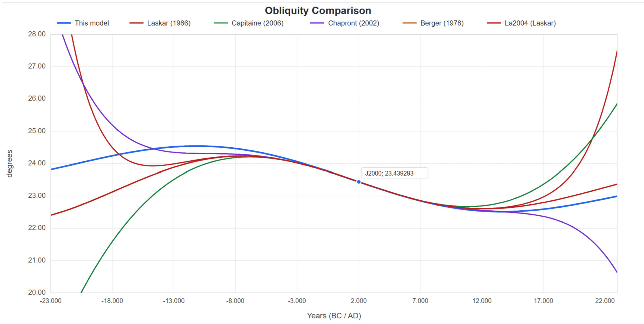

Figure 7: Obliquity predictions compared: this model (blue) versus La2004 (Laskar et al., 2004) (red) and Chapront et al. (2002) (green). Chapront's polynomial extrapolation diverges to unphysical values (20°–28°), while the model predicts bounded oscillation within 22.21°–24.72°.

merely a simplification. In coupled oscillator theory, two effectively identical oscillators produce normal modes with exactly equal amplitudes. Angular momentum conservation (Noether's theorem) requires that two counter-rotating motions with equal amplitudes produce zero net angular momentum transfer — the symmetric, energy-conserving state. Unequal amplitudes would require explaining why the symmetry is broken.

The model's inclination precession cycle (~111,772 years) is independently validated by comparison with the La2010a numerical orbital solution (Laskar et al., 2011), which provides Earth's orbital elements in the invariable plane frame over 250 Myr (Figure 8). Over 500 kyr, both show oscillation between ~0.845° and ~2.117°, with the current value near 1.58° (J2000; Souami & Souchay 2012).

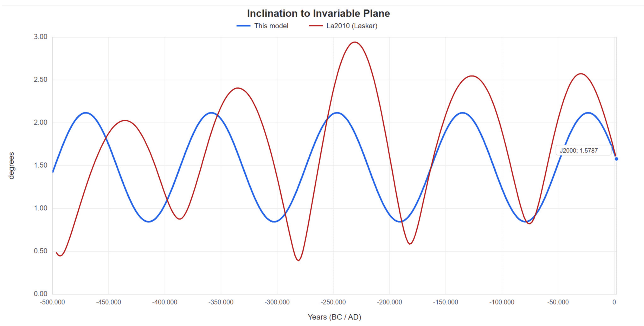

Figure 8: Orbital inclination compared: this model (blue) versus La2010a (Laskar et al., 2011) (red). Both show oscillation between ~0.845° and ~2.117° with the ~111,772-year period.

9.2 Eccentricity: The $H/3$ One-Law Line

In contrast to Milankovitch's ~95,000/125,000/400,000-year eccentricity cycles, the model proposes a single law on the $H/3$ inclination cycle, $e(t) = e'_{\text{base}}\,(1+\cos\theta_3/2)$, with e'_{base} derived from the observed J2000 value and the System-Reset anchor (the same law the lunar theory and the solar equation of centre ride; subsection 14.8). The $H/16$ beat of the two counter-rotating reference points governs where the perihelion *points*, not how elliptical the orbit is. Current eccentricity: 0.01671022 (J2000). Derived mean: 0.0155200. Range: ~0.0078–~0.0233. The law's rate at J2000, −0.0000431/cy, matches the observed $-4.2037e-5$/cy to 2.5% with no fitted input. Next minimum: ~32,682 AD (Figure 9).

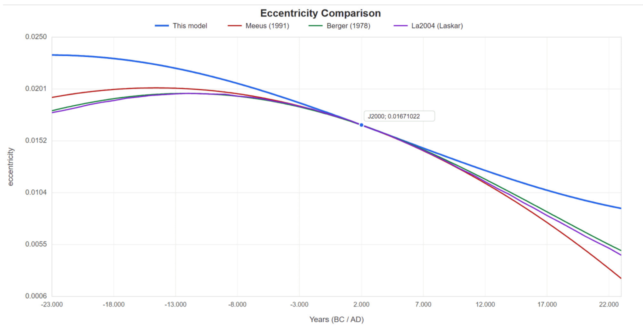

Figure 9: Eccentricity over ±20,000 years: this model (blue) versus the Meeus (1998) polynomial (red), Berger (1978) (green) and La2004 (Laskar et al., 2004) (purple). All converge at the observed J2000 value; beyond a few thousand years the secular solutions decline faster toward their deep minimum, while the single $H/3$ line declines more gently toward its own minimum of ~0.0078 at ~32,682 AD and then rises.

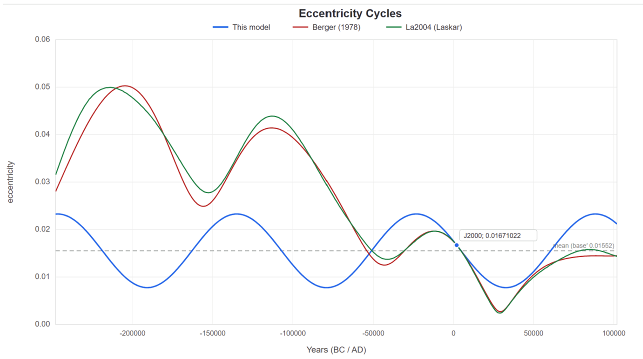

Figure 10: Eccentricity over −250,000 to +100,000 years: the model's $H/3$ line (blue) between ~0.0078 and ~0.0233 around the derived mean $e'_{\text{base}} = 0.0155200$ (dashed), against Berger (1978) (red) and La2004 (Laskar et al., 2004) (green), with the observed J2000 value marked. The single line reproduces the present decline and one minimum; it does not reproduce the multi-mode envelope of the secular solutions.

This curve reflects only Earth's own ~20,957-year perihelion cycle. Saturn's eccentricity is predicted by Law 5, and the two are coupled through the balance system and Saturn's ecliptic-retrograde precession (subsection 6.2); the coupled correction is not yet incorporated.

9.3 Longitude of Perihelion

The longitude of perihelion advances through all 360° once per ~20,957-year cycle, currently at 102.947° (J2000). Comparison with Meeus (1998) shows close agreement for ±3,000 years (±0.025° at 1000 AD, ±0.100° at 2500 AD); beyond this range the predictions diverge (Figure 11).

9.4 Length of Day and Timekeeping

Standard theory attributes Earth's rotational slowing to lunar tidal friction (~2.3 ms/century) (Stephenson et al., 2016), predicting monotonic increase in LOD. The model proposes an additional millennial-scale *cyclic modulation of the growth rate* superimposed on the secular trend (Table 19): LOD itself only grows — the secular baseline (+1.77 ms/cy)

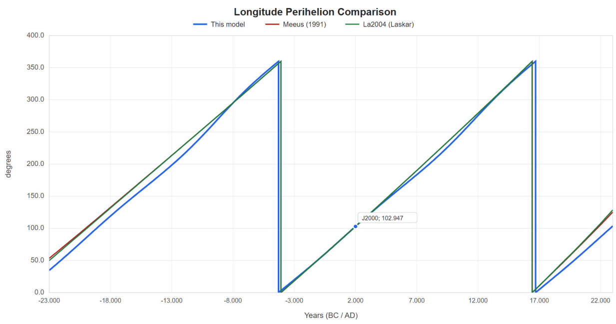

Figure 11: Longitude of perihelion: this model (blue) versus Meeus (1998) polynomial (red). Close agreement for ±3,000 years around J2000.

is modulated, never overcome. The composite δLOD of the four $8H$-lattice ΔT harmonics (Table 20) is currently in a descending phase (all-cycles rate -1.88 ms/cy at J2000, observable total -0.07 ms/cy), reaching its next trough (maximum below-baseline excursion) near ~2,250 AD and its next peak near ~2,750 AD, with successive extrema following the Bond/Hallstatt/Jose beat structure at a few-millisecond amplitude. This millennial oscillation rides on top of the Driver-1 monotonic tidal LOD growth that governs deep-time evolution (section 11, subsection 11.2); the two effects act on different timescales — the cyclical variation is milliseconds over millennia, while Driver 1 accumulates to several hours across the Phanerozoic. Short-term fluctuations are superimposed on both. Earth unexpectedly began rotating faster in 2020; July 5, 2024 set the all-time record for the shortest day since atomic-clock timekeeping began (1.66 ms under 24 hours) — qualitatively consistent with the model's prediction that LOD's growth rate is cyclically modulated.

The framework distinguishes **two mean-LOD values at any epoch** (Table 19). The kinematic baseline $\mathrm{LOD}_{\mathrm{mean}}$ follows from the $H/13$ identity that relates the sidereal year in seconds (J2000 anchor) to the framework's kinematic sidereal year in days ($\bar{Y}_{\mathrm{sid,kin}} = \bar{Y}_{\mathrm{trop}} \times H/(H-13)$). The physical value $\mathrm{LOD}_{\mathrm{real}}$ is the Layer 4 composite: it adds an $H/5$ ecliptic-precession correction, the calibrated cyclic ΔT stack (Bond/Hallstatt/Jose5/Jose4), and the Core-mantle swing so that at J2000 the composite exactly matches the USNO Earth Orientation Center anchor:

$$\mathrm{LOD}_{\mathrm{real}} = \underbrace{\mathrm{LOD}_{\mathrm{mean}} + \frac{\mathrm{LOD}_{\mathrm{mean}}}{(H/5)\,\bar{Y}_{\mathrm{trop}}}}_{\text{raw } H/5 \text{ kinematic}} + \underbrace{\sum_i \delta_{\mathrm{LOD},i}(t)}_{\Delta T \text{ cycles}} \tag{19}$$
$$= 86,400.001480 \text{ s at J2000}$$

where the raw $H/5$ kinematic term contributes $+3.527$ ms and the calibrated cyclic stack contributes a net -2.15 ms at J2000 to close the composite onto the USNO anchor (86,400.0018 s) by construction of the joint-optimum fit against Espenak history (RMS $\approx$ 12.5 s across 20 reference years 1650–2017).

Physically the $H/5$ term represents Earth's need to rotate slightly more per solar day to compensate for the ecliptic's slow precession in ICRF over the $H/5$ ecliptic-precession cycle ($H/5 \approx$ 67,063 yr); the mean solar day is measured against the Sun, whose apparent motion follows the ecliptic. Over one solar day the ecliptic advances by $1/((H/5)\bar{Y}_{\mathrm{trop}}) \approx 4.08 \times 10^{-8}$ revolutions, requiring $+3.527$ ms of extra Earth rotation. The $H/13$ axial precession is *already implicit* in $\mathrm{LOD}_{\mathrm{mean}}$ via the $H/(H-13)$ denominator (over H tropical years the sidereal frame counts $H-13$ years, the missing 13 being the axial-precession contribution); an additional $H/13$ correction would double-count. The remaining H-lattice cycles ($H/3$ inclination precession is an invariable-plane-frame effect, not the solar-day frame; $H/8$ obliquity oscillation time-averages to zero; $H/16$ perihelion motion enters the anomalistic year, not the tropical-day count) — only $H/5$ gives the correct reference frame for the Sun's apparent motion. Both $\mathrm{LOD}_{\mathrm{mean}}$ and $\mathrm{LOD}_{\mathrm{real}}$ evolve slowly with $H(t)$ under Driver 1 (section 11).

Table 19: Length of Day: kinematic and physical mean values at J2000 anchor (mean values rescale at geological time per section 11). $\mathrm{LOD}_{\mathrm{real}}$ is the Layer 4 composite of (19) — $\mathrm{LOD}_{\mathrm{mean}}$ plus the raw $H/5$ kinematic correction plus the calibrated cyclic ΔT stack and Core-mantle swing — and matches the USNO joint-optimum anchor exactly by construction of the fit against Espenak history.

Parameter	Model value	Reference
Solar day — $\mathrm{LOD}_{\mathrm{mean}}$ (kinematic, $H/13$ identity)	86, 399.999676 s	—
Solar day — raw $H/5$ kinematic (intermediate, no ΔT cycles)	86, 400.003634 s	(raw H/5 physics only)
Solar day — $\mathrm{LOD}_{\mathrm{real}}$ (Layer 4 composite, physical)	86, 400.001480 s	86, 400.0018 s (USNO joint-fit anchor, matches by construction)
Sidereal day	86, 164.0902182 s	86,164.090639 s (framework J2000 readout; IAU Aoki 86,164.090531 s)

The two mean-LOD conventions serve different purposes internally: $\mathrm{LOD}_{\mathrm{mean}}$ enters all sidereal-to-tropical conversions and the calibrated ΔT stack's integrand (which is jointly fit against Stephenson et al. (2016)/Espenak residuals assuming that baseline); the raw $H/5$ kinematic intermediate underlies the pure-$H/5$-physics ΔT prediction shown as the calibrated stack's baseline (the "V curve" near J2000); and $\mathrm{LOD}_{\mathrm{real}}$ is the Layer 4 composite (raw $H/5$ kinematic + calibrated cyclic stack + Core-mantle swing) used for the physical LOD readout and the USNO comparison above.

The four cyclical ΔT harmonics. The calibrated ΔT stack decomposes into four harmonics on integer divisors of $8H =$ 2, 682, 536 yr, each with an independent physical anchor established in the paleoclimate or solar-activity literature (Table 20). The four periods are structural predictions of the $8H/n$ lattice — zero free parameters. The four amplitudes and phases are calibrated in one joint solve — together with the Core-mantle swing episode described below — against the observed ΔT history (Espenak & Meeus (2006) polynomial, 1650–2017), with the composite Layer-4 LOD pinned to the USNO Earth Orientation Center anchor at $J2000$ as a hard equality constraint; RMS $\approx$ 12.5 s across 20 reference years. Their joint appearance in the ΔT residual — after subtracting the pure-tidal $H(t)$ trend — is the framework's central testable claim about the millennial cycle, and the four-harmonic configuration is the optimal one: removing any harmonic degrades both the in-sample closure (Espenak RMS rises from 12.5 s to 26–35 s) and out-of-sample prediction of an era withheld from the fit (predicting −720 to 0 CE from post-CE data alone: 85 s RMS with all four, against 94–307 s for any reduced set and a 223 s no-correction baseline).

Two limits must be stated alongside that result. First, **no individual harmonic is significant on its own**: each sits below its own permutation threshold in the ΔT record, so the four carry the residual collectively rather than severally. Second, **the identification of these periods with the named climate and solar-activity cycles they are numerically close to is not established**; the null tests behind that statement are reported once, with the IRD comparison, in subsection 14.11. The harmonics are therefore justified here as ΔT correction terms on structurally-derived periods — which is what they were calibrated against and what they demonstrably close — and not as detections of the named cycles.

Table 20: The four cyclical ΔT harmonics that generate the millennial LOD variation on top of the pure-tidal trend. Each period is an integer divisor of $8H$; each has an independent paleoclimate or solar-activity anchor. Periods are zero-fit structural predictions of the $8H/n$ lattice; amplitudes and phases are calibrated, jointly with the Core-mantle swing episode, against Espenak 1650–2017 history under the hard USNO LOD closure.

Cycle	Divisor	Period (yr)	Independent anchor
Bond	$8H/1830$	1,466	74× Jupiter–Saturn synodic; numerically close to the Bond et al. (2001) ~1470-yr N-Atlantic IRD cycle, though phase testing does not establish the two as the same signal
Hallstatt	$8H/1104$	2,430	Hallstatt solar-activity cycle (~2400 yr, cosmogenic-isotope reconstructions)
Jose5	$8H/2989$	897	5× Charvátová (2000) Jose 179-yr solar-inertial-motion cycle
Jose4	$8H/3749$	716	4× Charvátová (2000) Jose 179-yr cycle

The fifth component: the Core-mantle swing. On top of the four periodic harmonics, the joint solve fits one *aperiodic episode*: a damped oscillation of the core's eigenmode ($T_0 = 8H/685 \approx 3{,}916$ yr, $Q = 1.8$ — inside the published axisymmetric Magneto-Coriolis eigenmode range) driven at the bond–hallstatt difference tone ($8H/726$), excited around 1600 BC and actively terminated around 1600 AD, with displacement-continuous (impulse-consistent) kicks. Physically this is the documented millennial core–mantle length-of-day fluctuation — the ~1,500-yr oscillation of Stephenson et al. (2016), mechanistically modelled by Dumberry & Bloxham (2006) as core–mantle angular-momentum exchange — so, unlike the four climate-mediated harmonics, its amplitude is core-supplied rather than ice-mass-mediated. It contributes $d\mathrm{LOD}/dt|_{\mathrm{swing}} = +0.04$ ms/cy at J2000 and is the framework's fourth $d\mathrm{LOD}/dt$ driver alongside tidal, GIA, and the cyclic stack.

The ΔT trend anchor. The framework's ΔT trend anchor at $J2000$ is $\Delta T_{\mathrm{trend}}(J2000) = 55.16$ s, distinct from the IERS-observed instantaneous value $\Delta T \approx 63.63$ s. The ~8-second offset is definitional, not disagreement: the observed instantaneous value includes decadal-scale non-tidal residuals (atmospheric angular-momentum transfer, mantle-core coupling, ENSO) that vary on year-to-year timescales; the trend value is the noiseless mid-line of the calibrated model. Numerically `deltaTStart` is selected together with the USNO LOD anchor value (86,400.0018 s) by joint-optimum sweep minimizing $\sum_y(\Delta T_{\mathrm{model}}(y) - \Delta T_{\mathrm{Espenak}}(y))^2$ across the same 20 reference years 1650–2017 that constrain the four cyclical harmonics above. Readers cross-checking values against IERS ΔT tables should expect the ~8-second trend/instantaneous offset by construction.

Decomposing $d\mathrm{LOD}/dt$ at J2000. The composite LOD's total time-derivative decomposes into a monotonic secular piece and a millennial-cyclic piece. The secular piece splits further into the pure-tidal $H(t)$ trend and the $L1$-orbital-coupled $\alpha(t)$ GIA correction: $d\mathrm{LOD}/dt|_{\mathrm{tidal}} = +2.12$ ms/cy (Farhat pure-tidal) and $d\mathrm{LOD}/dt|_{\mathrm{GIA}} = -0.35$ ms/cy (GIA via $\alpha(t)$; Cox & Chao (2002) $\dot{J}_2$ anchored), summing to a net secular $d\mathrm{LOD}/dt|_{\mathrm{secular}} = +1.77$ ms/cy. The four cyclical ΔT harmonics of Table 20 contribute $d\mathrm{LOD}/dt|_{\mathrm{cycles}} = -1.88$ ms/cy at J2000 (currently in a descending phase of the composite cycle) and the Core-mantle swing adds $d\mathrm{LOD}/dt|_{\mathrm{swing}} = +0.04$ ms/cy, so the observed total is $d\mathrm{LOD}/dt|_{\mathrm{full}} = -0.07$ ms/cy at J2000. All channel contributions carry zero free parameters relative to the framework's shipped physics: tidal from $H(t)$; GIA from independent satellite gravimetry $\dot{J}_2$; cycles and swing calibrated jointly on Espenak history under the hard USNO closure.

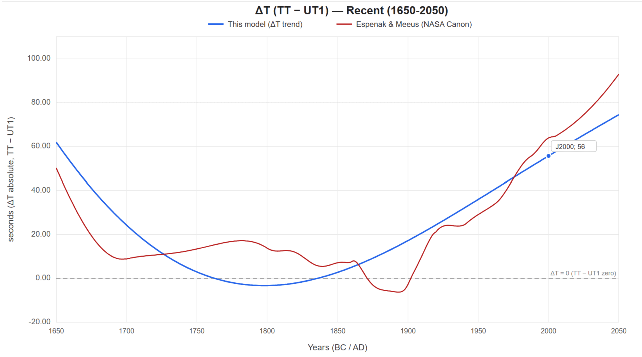

Figure 12: The framework's ΔT trend curve 1650–2050 (blue) overlaid on the Espenak & Meeus (2006) polynomial (grey). The pure-tidal $H(t)$ trend plus the four cyclical harmonics of Table 20 and the Core-mantle swing episode, anchored at $\Delta T_{\mathrm{trend}}(J2000) = 55.16$ s, reproduces the characteristic V-shape (minimum near ~1900 AD) without polynomial coefficients fitted to observed ΔT. Residual against Espenak & Meeus (2006) across 20 reference years 1650–2017 is ≈ 12.5 s RMS. The V-shape is not fitted; it emerges from the pure-tidal trend plus the calibrated stack, and the exact minimum location near ~1900 AD is a prediction rather than a curve-fit.

Mitchell & Kirscher (2023) demonstrated that Earth's day length stalled at approximately 19 hours for roughly 1 billion years during the mid-Proterozoic, likely due to atmospheric thermal tides balancing lunar tidal deceleration (Bartlett & Stevenson, 2016). This proves that LOD dynamics are more complex than simple tidal deceleration and that additional mechanisms can influence Earth's rotation over geological timescales.

The model's ΔT formula — derived from the same lunar-distance evolution that governs LOD on deep-time scales (subsection 11.2), together with an L1-orbital-coupled $\alpha(t)$ GIA correction anchored on independent satellite gravimetry (Cox & Chao (2002)) and tied to the L1 orbital layer of the Climate Formula (subsection 10.5) — has been validated on two complementary tracks: a solar-eclipse alignment test on 26 documented events spanning −762 to 2026 CE (21/26 with the model umbra reaching the observation site within a ±4-hour scan window; 5/26 geographic-class events (an umbra-centerline metric; the penumbra can still cover the site); subsection 14.10), and a 267-event working set from the Stephenson et al. (2016) lunar timing record (20.2-min mean |residual|; subsection 14.11). Together the two tests reject the full Munk-MacDonald-scale (~5–6 ms/century) non-tidal speedup and confirm a smaller GIA-scale contribution carried by $\alpha(t)$; a residual fractional non-tidal channel (~0.5 ms/century window-average, ~10% of Munk-MacDonald) in the medieval-era residual is carried by the Core-mantle swing episode introduced above.

9.5 Obliquity & Eccentricity Define Lengths of Days & Years

Year lengths in days and the length of day in SI seconds follow closed-form Fourier harmonic series anchored to a single input constant ($\bar{Y}_{\text{trop}} = 365.2422$ days). All three year types share the same form:

$$Y(t) = \bar{Y} + \sum_i \left[s_i \sin\left(\frac{2\pi t}{T_i}\right) + c_i \cos\left(\frac{2\pi t}{T_i}\right) \right] \tag{20}$$

with periods $T_i = H/n$ at small integer divisors n. The tropical year uses 12 harmonics (dominant: $n = 8$, the obliquity cycle), the sidereal year uses 5 (dominant: $n = 8$ and $n = 3$), and the anomalistic year uses 8 (dominant: $n = 24$, the beat between obliquity and inclination). The means are derived: $\bar{Y}_{\text{trop}}$ from input snapping to the $H/8$ grid, then $\bar{Y}_{\text{sid}} = \bar{Y}_{\text{trop}} \times (H/13)/(H/13 - 1)$ and $\bar{Y}_{\text{anom}} = \bar{Y}_{\text{trop}} \times (H/16)/(H/16 - 1)$. **Length of Day** follows from the sidereal year being held at its J2000-anchor value of 31, 558, 149.76 seconds:

$$D = \frac{31,558,149.76}{Y_{\text{sid}}(\text{days})} \tag{21}$$

The harmonic system reproduces the model's year-length output to RMS ~0.03 seconds on the tropical year and machine precision on the sidereal and anomalistic years.

The two formulas reveal a clean separation of roles. The tropical year is almost entirely determined by the obliquity cycle ($T = H/8 \approx$ ~41, 915 yr), while eccentricity has negligible effect. Conversely, the sidereal year in days is determined by eccentricity: the sidereal year *in seconds* is held at its J2000-anchor value of 31, 558, 149.76 s within this section's modern-era scope (Earth's orbital period relative to fixed stars; at deep time this value drifts via solar mass loss through Kepler's third law — see section 11), but changing eccentricity changes the day length, which changes how many days fit into that J2000 number of seconds. The day length varies by ~0.7 ms peak-to-peak over the ~20,957-year perihelion cycle. Additionally, tropical years measured at different cardinal points differ by up to ~91 seconds due to eccentricity effects (from −46 s at the summer solstice to +45 s at the winter solstice at the current epoch), with the pattern rotating through the seasons over the perihelion cycle.

9.6 The Cardinal-Point Braid Law

The per-point year-length differences above are not four independent phenomena. Writing the event-time offset of cardinal point X from the mean tropical year as δ_X (with $\sum_X \delta_X \equiv 0$ by construction), the model requires

$$\delta_X(t) = \text{Im}\left[e^{\,i n \lambda_X}\, W_n(t) \right], \qquad \lambda_{\text{SS}}, \lambda_{\text{AE}}, \lambda_{\text{WS}}, \lambda_{\text{VE}} = 0°, 90°, 180°, 270° \tag{22}$$

— one complex function per order n, read through four fixed rotations. $W_1(t)$ is Earth's perihelion vector of the $H/16$ cycle as seen in event time (the equation-of-centre braid, with $e(t)$ the single $H/3$ eccentricity law). The law is verified at three independent levels against the model's full 335,318-row event catalogue spanning one H cycle:

1. **Carrier (order 1):** the four *independently* fitted $e \sin M$ terms sit in 90° quadrature with equal amplitudes to 0.08° / 0.29% spread — a property the fit does not enforce, so additional fitting freedom cannot fake it.
2. **Order 2:** the $e^2 \sin 2M$ terms repeat the pattern at phase $2\lambda_X$ (pairwise: solstices against equinoxes).
3. **The modulation spectrum:** the residual mid-band content (divisors $H/20$–$H/37$) is captured by 52 coefficients *shared across all four points* — zero per-point freedom — reducing the residual from ~1.2–1.7 to 0.28–0.37 min over ±270 kyr, with held-out rows reproducing the in-sample statistics exactly.
4. **The symmetry test:** the law requires the four points to be statistically identical, and they are — 0.28/0.28/0.36/0.37 min. An earlier 2× excess at one point traced to the fit basis, not the physics: its historically-frozen sinusoid set lacked one divisor, at which its residual carried a coherent 73-s line. Symmetrizing the basis (one identical divisor set for all four points) equalized the residuals and *tightened* the carrier quadrature from 0.22° to 0.08°.

The sign experiment. What elevates level 3 above a goodness-of-fit statistic is a discrete, falsifiable requirement: because the carrier is $e^{i(\lambda_X - \theta_{16})}$, the model requires the seasonal-asymmetry spectrum to be quadrature-locked *counter*-rotating — sidebands must carry point-phase $+n\lambda_X$ against time-phase $-\theta_d$. Both rotation senses were fitted with identical freedom. The counter-rotating lock captures the residual; the co-rotating lock captures *nothing* (RMSE unchanged to three digits). A wrong geometry would fail both senses; an over-flexible basis would pass both. Exactly one sense passing is structure detection: Earth's seasonal asymmetries — from the ~91-second per-point spread at J2000 down to the sub-minute sideband comb — are a single rotating geometric object, the perihelion vector, with no per-point physics anywhere in the description.

Forward prediction. The law fixes the *differential drift rates* of the four per-point tropical years with zero per-point freedom: at J2000, relative to the common mean, SS +0.4, WS −0.4, VE +1.5, AE −1.6 s/century — two near-opposite pairs summing to zero, the quadrature structure expressed in rates. Century-scale precision timing of equinoxes and solstices must reproduce this pattern, and any high-precision decomposition of cardinal-point timing residuals must place the fine structure in the counter-rotating sideband only; a coherent co-rotating component at measurable amplitude would falsify the one-vector geometry.

9.7 The Coin Rotation Paradox

The model reveals structural relationships between different measures of days and years (Table 21).

Table 21: Types of days and years. All values are J2000-anchor snapshots; under section 11 the SI-second values drift via Driver 2 (solar mass loss → Kepler) and the day counts drift via Driver 1 (Earth-Moon tidal evolution).

Type	Reference	Duration
Solar day	Sun's apparent position	~86,400 s
Sidereal day	Precessing equinox	~86,164.09 s
Stellar day	Fixed stars (ICRF)	~86,164.10 s
Solar year	Equinox to equinox	~365.2422 d
Sidereal year	Fixed stars	31,558,149.76 s
Anomalistic year	Perihelion to perihelion	~365.2596324 d

The difference between stellar and sidereal day, and between sidereal and solar year, are direct consequences of axial precession. Two related but distinct quantities appear below. The counting identities use 9.12 ms/sidereal day, the precession rate p measured *along the ecliptic* (precession in longitude), which is the frame the $H/13$ lattice is defined in. This is the difference between the sidereal day and the *ecliptic sidereal day* (86,164.099760 s), the ecliptic-frame counterpart to the stellar day. The physical stellar−sidereal day offset is smaller, 8.37 ms, because it is the same precession projected onto the *equator* by $\cos\varepsilon$ (precession in right ascension, $m = p\cos\varepsilon$), which is what a meridian clock measures directly; with that projection the framework stellar day is 86,164.099007 s, matching the IAU 2000A value to within 0.01 ms. Substituting the equatorial figure into the identity below would give 0.917 sidereal days per cycle rather than exactly one — because the identity is written in ecliptic longitude, not equatorial time. Both p and m are in the IAU precession model; the ecliptic sidereal day is not directly meridian-observable (clocks project onto the equator by construction) but is fully determined by observed quantities: given the measured equator-projected offset 8.37 ms/day and the observed obliquity $\varepsilon = 23.4393°$, the ecliptic-lattice rate follows as $8.37/\cos\varepsilon = 9.12$ ms/day. The precession rate varies over the Earth Fundamental Cycle: the cycle-averaged mean period is ~25,794 years[1], while the current instantaneous period is ~25,771 years. Using mean values, each difference accumulates to exactly one fewer unit per cycle (J2000-anchor arithmetic — the identities below are integer-invariant; the literal SI-second and day counts rescale with $H(t)$ per section 11):

Day level:

$$9.12 \text{ ms/sid. day} \times 366.25 \text{ sid. days/yr} \times {\sim}25,794 \text{ yr} \approx 86{,}164 \text{ s} = 1 \text{ sidereal day} \quad (23)$$

Year level:

$$1,223.49 \text{ s/yr (mean solar–sidereal year diff.)} \times {\sim}25,794 \text{ yr} \approx 31{,}558{,}150 \text{ s} = 1 \text{ sidereal year} \quad (24)$$

The coin rotation paradox (a coin rolling around an identical coin makes 2 rotations, not 1) manifests at these two scales (the +1/−1 *structural* identities below are invariant at any epoch under section 11; the literal day counts evaluated here are J2000 snapshots — e.g. Devonian had ~400 d/yr, so the literal "365.25" rescales while the "+1 extra rotation" rule survives):

- **Daily**: 366.25 sidereal days = 365.25 solar days per year (one extra stellar rotation from orbital motion)
- **Yearly**: 25,793 sidereal years = ~25,794 solar years per axial precession cycle (one fewer sidereal year from the precession orbit)

This self-consistency check links the model's precession period to its day/year length formulas at the J2000 anchor; under section 11 the equality of the structural identities is what is preserved across epochs, not the literal numerical year/day values.

9.8 Milankovitch Beat Frequency Structure

The five Milankovitch-type cycles — apsidal precession, nodal regression, obliquity, axial precession, and perihelion precession — are not independent. Standard orbital mechanics derives two as beat frequencies of the others (Vervoort et al., 2022). The model's identification of all five as H/n, with $n \in \{3, 5, 8, 13, 16\}$, reveals that these beat frequency relationships are Fibonacci identities:

Table 22: Milankovitch beat frequencies as Fibonacci arithmetic. The Fibonacci-divisor identities (13 − 5 = 8, etc.) are integer-invariant at any epoch; the literal $1/H$ rate values are J2000 snapshots that rescale with $H(t)$ per section 11.

Physical equation	Model form	Fibonacci
$f_{\text{obliquity}} = f_{\text{axial}} - f_{\text{nodal}}$	$8/H = 13/H - 5/H$	$13 - 5 = 8$
$f_{\text{perihelion}} = f_{\text{axial}} + f_{\text{apsidal}}$	$16/H = 13/H + 3/H$	$13 + 3 = 16$
$f_{\text{apsidal}} = f_{\text{obliquity}} - f_{\text{nodal}}$	$3/H = 8/H - 5/H$	$8 - 5 = 3$
$f_{\text{nodal}} = f_{\text{axial}} - f_{\text{obliquity}}$	$5/H = 13/H - 8/H$	$13 - 8 = 5$

The Fibonacci subtraction property ($F_n = F_{n+2} - F_{n+1}$) is exactly the condition needed for the physical beat equations to close within the H/n system. Non-Fibonacci indices would fail: if the indices were $\{3, 7, 10, 14, 17\}$, then $14 - 7 \neq 10$ and the obliquity equation would not close. All five standard Milankovitch periods are reproduced to within 0.3–2.8% from a single constant H.

Deep-time extension via 8H. The Solar System Resonance Cycle $8H = 2,682,536$ yr (J2000 anchor) extends the H/n hierarchy to longer timescales; its 33-integer L1 lattice is the structural foundation of the canonical Climate Formula (subsection 10.5). Fibonacci *multiples* of H also match established geological cycles: $3H = 1{,}005{,}951$ yr matches the $g_1 - g_5$ eccentricity beat (~980,000 yr, ~2.6% difference), and $13H = 4{,}359{,}121$ yr matches the secular resonance libration period (Boulila et al., 2018) (~4,500,000 yr, ~3.1%). The Fibonacci ladder thus extends from $H/16 = {\sim}20,957$ yr to $13H = 4{,}359{,}121$ yr — a factor of 208 in timescale. All literal year values in this paragraph are J2000-anchor snapshots; the Fibonacci-multiple *integer structure* ($3H$, $13H$) is invariant at any epoch, while the literal megayear counts rescale smoothly at geological time per section 11 (over the Mesozoic–Cenozoic test record, $H(t)$ drifts by ~1–2%).

Eigenfrequency convergence at Earth's Fibonacci anchors. Multiple independent Laskar (Laskar et al., 2004)

[1] ~25,794 yr is the J2000-anchor cycle-mean. The structural identity $H = 13 \times T_{\text{axial}}$ is integer-invariant under section 11; the literal year value rescales smoothly at geological time (Devonian $T_{\text{axial}} \approx 23{,}776$ yr).

eigenfrequency combinations converge on the same H/n values. $H/3 = \sim 111,772$ yr (Inclination Precession) matches three independent combinations: the total apsidal rate ($\sim 112,000$ yr, 0.6%), the $g_3 - g_1$ eccentricity beat (109,950 yr, 1.7%), and the $|s_2 - s_3|$ inclination beat (109,851 yr, 1.8%). $H/5 = \sim 67,063$ yr (Ecliptic Precession) matches the s_3 eigenfrequency (68,750 yr, 2.5%), the rate at which Earth's orbital plane precesses around the invariable plane (subsection 6.3).

Eigenfrequency convergence on the 8H lattice. The secular periods produced by Jupiter+Saturn gravitational coupling on Earth's orbital plane (Law 6, subsection 6.1) sit one lattice integer off these Fibonacci anchors and match Laskar two orders of magnitude tighter:

Table 23: Secular periods on the 8H lattice match Laskar to $\leq$ 0.12%

Model period	Laskar eigenmode	Agreement
$8H/39 = 68,783$ yr	$\|\|s_3\|\|$ (68,750 yr)	**0.04%**
$8H/65 = 41,270$ yr	$k + s_3$ (41,220 yr)	**0.12%**

The empirical LR04 obliquity peak (40,950 yr from a fine-grid spectral sweep) lands within one Rayleigh element of both, and $8H/65$ is the period at which Jupiter's ICRF perihelion and Saturn's ecliptic perihelion lock — the climate-recorded $k + s_3$ obliquity beat (Law 6). This convergence is not required by any known theory and is not a calibration: neither method consults the other. Per-eigenmode attribution differences between the Berger and Holistic frameworks are documented in subsection 10.7.

9.9 Solstice Right Ascension Oscillation

The model predicts that the Sun's ICRF right ascension at maximum declination (June solstice) oscillates with amplitude $\sim \pm$ 12.5 min RA (time units; equivalently $\sim \pm$ 3.125°) around a mean displaced ~12.5 min *below* 6h (the ICRF mean offset $-\rho/\sin\bar{\varepsilon}$), reaching its maximum — exactly 6h — at the 1246.03 AD perihelion–solstice alignment. The mechanism is a superposition of two co-equal H-lattice cycles — distinguishing the Holistic model's prediction from single-mechanism obliquity-only estimates.

The closed form implemented in the reference simulator (function `computeSolsticeRA`) is

$$\mathrm{RA}(t) = \mathrm{base} - \rho/\sin(\bar{\varepsilon}) + \frac{A}{\sin(\bar{\varepsilon})}\left[-\sin\left(\frac{2\pi t}{H/3}\right) + \sin\left(\frac{2\pi t}{H/8}\right)\right], \tag{25}$$

with base = 90°/270°/0°/180° for SS/WS/VE/AE, ρ a small ICRF mean offset, $A = 0.63607°$ the shared driver amplitude of the H/3 inclination and H/8 obliquity cycles (the same A appears in the model's two-component obliquity formula $\varepsilon(t) = \bar{\varepsilon} - A\cos(2\pi t/(H/3)) + A\cos(2\pi t/(H/8))$, structurally coupling the two Fibonacci divisors), and t = year − balancedYear. Empirical LSQ fit against model-computed SS events sampled at 1-yr cadence across one full Earth Fundamental Cycle ($H = 335,317$ yr) recovers the two-harmonic structure with RMSE = 2.1 arcmin; extending to a three-term basis including the $H/16$ candidate below improves RMSE only to 1.94 arcmin and returns an $H/16$ amplitude of 0.02°, ~80× smaller than the two dominant terms.

Component 1 — $H/3$ inclination frame shift (co-equal amplitude, ~111,772-yr period). Earth's orbital-plane inclination in ICRF oscillates ±0.63607° at the $H/3$ period. This tilts the ecliptic-plane reference frame relative to ICRF, shifting the RA at which the max-declination event occurs. Contribution:

$$|\Delta\alpha_{\mathrm{incl}}|_{\max} = \frac{A}{\sin(\bar{\varepsilon})} \approx \frac{0.63607°}{\sin(23.41353°)} \approx 1.60° \approx 96 \text{ arcmin RA.} \tag{26}$$

Period: $H(t)/3 = \sim 111,772$ yr at J2000.

Component 2 — Obliquity variation (co-equal amplitude, $H/8$ period). Earth's axial tilt oscillates ±0.63607° over the $H/8$ obliquity cycle from the same driver as Component 1, contributing an equal-magnitude term with opposite sign:

$$|\Delta\alpha_{\mathrm{obl}}|_{\max} = \frac{A}{\sin(\bar{\varepsilon})} \approx 1.60° \approx 96 \text{ arcmin RA.} \tag{27}$$

Period: $H(t)/8 = \sim 41,915$ yr at J2000. Because the two components share the same driver amplitude and enter Eq. 25 with the same $1/\sin(\bar{\varepsilon})$ sensitivity, they are strictly co-equal.

Superposition and anchor. The $(-\sin + \sin)$ shape of Eq. 25 vanishes at $t = 0$, the balancedYear anchor (302,635 BC). At the 1246.03 AD perihelion–solstice alignment ($t = 14.5 \times H/16$) the $H/8$ term sits exactly at its maximum ($\sin = +1$) and the $H/3$ term at +0.98, so the composite reaches $\sim +1.98$ of its ±2 envelope — the solstice RA *peaks* there, at exactly 6h, the peak deviation cancelling the ICRF mean offset $-\rho/\sin\bar{\varepsilon}$. The $H/3$ and $H/8$ periods sit at an exact 8:3 ratio (since $(H/3)/(H/8) = 8/3$ by the Fibonacci divisor structure), so the composite signal is exactly H-periodic (period $H = 335,317$ yr) with an inner beat envelope at $H/5 = \sim 67,063$ yr — Earth's own ecliptic precession period on the Fibonacci lattice — reaching peak ±12.5-min swing at phase combinations where both sinusoids reinforce. Secondary mechanisms ($H(t)$ deep-time drift, general precession $H/13$, tropical-calendar drift) contribute the residual ~2-arcmin RMSE beyond the two-term closed form.

The $H/16$ equation-of-center subsignal. The Kepler equation of center $\Delta\lambda_{\mathrm{EoC}} = 2e(t)\cos(\varpi(t))$, with ϖ precessing at $2\pi/(H/16)$, would in principle displace the Sun's true ecliptic longitude at solstice by up to $2 \cdot 0.01675 \approx 1.92°$, giving a potential RA displacement $|\Delta\alpha_{\mathrm{EoC}}|_{\max} \approx 2e/\cos(\bar{\varepsilon}) \approx 2.09°$ at maximum coherence *if* the solstice event were defined by mean ecliptic longitude 90°. In practice, the solstice event is located by maximum declination — i.e. $\partial\delta/\partial t = 0$, which coincides with true ecliptic longitude 90° regardless of eccentricity — so the EoC displacement is absorbed into event location and does not translate to an SS RA shift. What remains at $H/16$ in the model output is a residual 0.02° (~5 arcsec) sub-signal from the perihelion-direction precession acting through the equation of centre — $e(t)$ itself carries no $H/16$ term under the one-law eccentricity. This is a testable prediction — an observed $H/16$ peak larger than a few arcsec would falsify the model's max-declination event definition.

Falsifiable spectral signature. Traditional obliquity-only derivations (Laskar et al., 1993) predict a single spectral peak at the obliquity period. The Holistic model predicts *two co-equal spectral peaks* at the $H/3$ (~111,772 yr) and $H/8$ (~41,915 yr) periods in an 8:3 harmonic ratio, plus a much smaller $H/16$ EoC sub-peak reduced to ~5 arcsec by the max-declination event definition. Long-baseline VLBI or historical solstice records could distinguish these; the model's specific claim is the co-equal 8:3 ratio between the H/3 and H/8 peaks, not a single obliquity peak nor an $H/16$ EoC peak. Current shift rate is order tens of arcsec/century, well within astrometric precision.

10. The Canonical Climate Formula: Gravitational Coupling and the 8H Lattice

10.1 Summary

The 33-integer 8H lattice (L1) — with frequency positions *fixed by orbital geometry and not fitted to climate* — explains $R^2 = 0.87$ of post-MPT LR04 ice-volume variance from L1 alone. Adding the classical Berger 1978 insolation features (obliquity $\varepsilon(t)$, eccentricity $e(t)$, and the climatic-precession products $e\sin\varpi$ and $e\cos\varpi$) to the canonical L1+L2+L3 formula yields $\Delta R^2 < 0.005$ across every regime tested. Substituting Laskar 2010's full-range eccentricity for the model's analytical $e(t)$ does not change the result: $\Delta R^2 = 0.000$ on LR04 (0–500 kyr) and 0.00001 on EPICA CO_2 (0–800 kyr). Classical Berger insolation features *alone* explain only $R^2 = 0.05$ of the same post-MPT LR04 record — 17× less than L1 alone.

The implication: Earth's climate is forced by the gravitational coupling of the entire solar system, with the 8H integer-divisor lattice as the natural parameterisation. Solar insolation is one channel through which that coupling reaches Earth; the lattice already encodes all the variance the Berger 4-feature projection produces. The two parameterisations are not independent forcings — they describe the same gravitational physics at different granularities, and the lattice is strictly more expressive than the classical insolation parameterisation.

10.2 The Inclination-Side Family of Eigenmode Beats

The dominant ~100,000-year periodicity in ice core records (Hays et al., 1976) is **a multi-planet eigenmode-beat signal modulating Earth's orbital plane**, not direct eccentricity forcing. Multi-component analysis of LR04 with the canonical 33-integer L1 lattice on $8H = 2,682,536$ yr (subsection 10.5) identifies the empirical centroid at $n = 25 = 107.3$ kyr — the $s_1 - s_4$ **nodal eigenmode beat**, a planet-pair orbital-plane coupling. Berger's classical 95-kyr peak appears at $n = 28 = 95.8$ kyr ($g_4 - g_5$ eccentricity eigenmode beat), and a contribution at $n = 22 = 121.9$ kyr ($s_2 - s_4$ nodal eigenmode beat) completes a broad single peak spanning ~80–125 kyr. None of these is reducible to Earth's intrinsic inclination cycle. Direct eccentricity attribution faces three specific empirical failure modes:

- **405-kyr absence**: Berger's strongest predicted eccentricity beat ($g_2 - g_5$, ~405 kyr) is essentially absent in post-MPT LR04 with amplitude ratio 0.120 versus the 100-kyr peak.
- **No bispectral 95k+125k phase coupling**: Hinich-style bispectrum on LR04 gives bicoherence 0.507, below the null 95th percentile of 0.555 — replicating the bispectral evidence of Muller & MacDonald (1997b).
- **Wrong-family centroid**: the 107-kyr empirical centroid is a *nodal* (orbital-plane) beat, not the *apsidal* (eccentricity) beat at 95–99 kyr that direct eccentricity attribution predicts.

Earth's own inclination ($H/3 = \sim 111,772$ yr) and obliquity ($H/8 = \sim 41,915$ yr) are real integer-divisor positions on the 8H lattice (at $n = 24$ and $n = 64$) but **do not play a direct climate-driving role in the 100-kyr world**: $n = 24$ is one of the formula's 33 L1 divisors (regime-admitted, section 10), but on the full LR04 record it carries only 0.79× the median L1 amplitude. At LR04's record length ($T \approx 1.2$ Myr, Rayleigh $\Delta P \approx 10$ kyr at $P = 110$ kyr) the $H/3 = 111.77$ kyr position sits within the same broad band as the signal-carrying integers, but the L1 amplitude fit cleanly separates them. The visual alignment of $H/3$ with the glacial envelope at the 400-kyr Vostok window (Figure 13) is real but misleading; it does not survive the L1 amplitude fit on the longer LR04 record. One qualification: in the pre-iNHG regime (2.7–5.3 Myr) the record does carry the $H/3$ line — added to the lattice there it gives $\Delta R^2 = +0.0196$, cross-validated, at the model's own phase ($\Delta\phi = -8.5°$; see the insolation test below). Secular theory has no 112-kyr eccentricity line, so this is the one lattice position attributable to Earth's own eccentricity rather than to a planetary beat; its admission to L1 is left as an open structural decision.

10.3 Peer-Reviewed Support: Muller & MacDonald (1997)

Muller & MacDonald (1997b), published in PNAS, demonstrated three key findings: (1) the eccentricity spectrum shows split peaks at ~95 ka and ~125 ka while climate shows a *broad single peak* spanning ~80–125 ka, without the spectral split direct eccentricity forcing would produce; (2) eccentricity's dominant ~400 ka component is largely absent from climate records; (3) Earth's orbital *inclination* (measured relative to the invariable plane) provides a better spectral match — including bispectral phase coupling — at ~100,000 years. Ridgwell et al. (1999) independently questioned the eccentricity attribution. The canonical Climate Formula preserves Muller's spectral finding: Earth's inclination *carries* the 100-kyr-band signal, but the signal source is the multi-planet eigenmode-beat band identified above (subsection 10.2), not Earth's intrinsic $H/3$ inclination precession. Muller's proposed mechanism (interplanetary dust) was rejected by the community; his *spectral-shape* finding survives intact and is captured by the formula's L1 layer.

10.4 Empirical Test: Spectral Analysis of Non-Tuned vs. Tuned Records

A common defence of the inclination interpretation appeals to circularity in ice core chronologies: many records employ orbital tuning — adjusting timescales to match Milankovitch insolation — which would artificially compress a true ~112-kyr signal toward ~100 kyr. Modern chronologies (AICC2012; Veres et al. 2013) minimize this through annual layer counting, volcanic markers, and U-series dat-

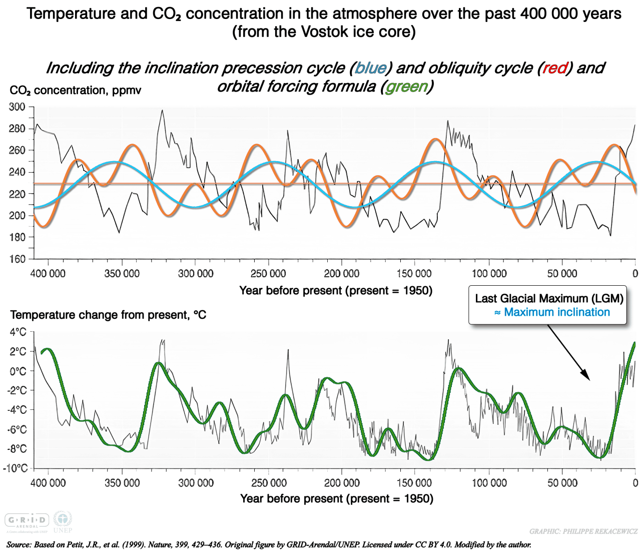

Figure 13: Vostok ice core temperature and CO_2 data over the past 400 kyr (Petit et al. 1999, CC BY 4.0). Three reference curves are overlaid for visual context: **blue** marks Earth's own $H/3 = {\sim}111,772$ yr inclination precession (CO_2 panel), **red** marks the $H/8 = {\sim}41,915$ yr obliquity cycle, and **green** is the canonical Climate Formula on the temperature panel. The visual alignment of the blue $H/3$ curve with the glacial envelope at this window is striking but **misleading**: on the full LR04 record (Figure 14) the L1 fit places near-zero amplitude at $n = 24 = H/3$, with the signal carried instead by the eigenmode-beat band of subsection 10.2.

ing (Kawamura et al., 2007), but for ice older than ~400 ka, orbital tuning remains significant. We tested the chronology-bias hypothesis directly.

Test design. We compared the orbitally-tuned LR04 benthic δ^{18}O stack (Lisiecki & Raymo, 2005) against the U-Th-dated speleothem record of Cheng et al. (2016). The Cheng2016 chronology is constructed independently of any orbital assumption (U-Th decay constants are atomic-physics-derived, with sub-1% precision across 0–640 kyr). If chronology bias were responsible for the ~10% gap between ~100 kyr and the model's $H/3 = {\sim}111,772$ yr prediction, the non-tuned record should place the peak measurably closer to 112 kyr.

Result. Discrete Fourier transforms of both records on a 1.2-Myr window place the dominant peak in *the same FFT bin* ($k = 6$, centroid $\approx$ 107 kyr). A systematic ~10% chronology offset between tuned and non-tuned records does *not* exist; the apparent gap to ~111,772 yr is therefore not a dating artifact.

Spectral resolution as the binding constraint. At a record length $T \approx 1.2$ Myr, the Rayleigh resolution limit at $P = 110$ kyr is $\Delta P \approx P^2/T \approx 10$ kyr. The candidates 95 kyr, 100 kyr, and 112 kyr therefore lie within one Rayleigh element of each other and are *spectrally collinear* — they cannot be independently determined by Fourier or multitaper methods at this data length. The model's $H/3 = {\sim}111,772$ yr sits comfortably inside this resolution-limited band, alongside eccentricity's 95-kyr / 125-kyr components. Both attributions are consistent with the data; what distinguishes them is the spectral *shape* (subsection 10.3) and the absence of the 405-kyr signal in post-MPT LR04, not the central peak position.

Beyond the centroid: full-lattice cross-proxy fit. The chronology-bias test above concerns the dominant peak alone. The full 33-integer L1 lattice was additionally fitted to the Cheng et al. (2016) Asian Monsoon δ^{18}O record under the same sequential-ridge architecture as the LR04 fit. The Cheng 2016 record uses U-Th radiometric dating (no orbital tuning), records Asian Monsoon precipitation strength (a different physical mechanism from ocean ice volume), and lives on a Lomb-Scargle irregular sampling grid; the same 33-integer lattice reaches $R^2 = 0.68$ on this cross-proxy. Of the top five lattice lines fitted to each record, only $n = 66$ (an obliquity-band integer at $8H/66 \approx 40.6$ kyr) is shared between Cheng 2016 and LR04 — per-integer amplitudes differ because monsoon strength and ice volume are sensitive to different beats — yet the full 33-integer lattice fits both records with substantial explained variance. The lattice positions, not the dominant per-integer amplitudes, are the structure that survives the cross-proxy translation.

10.5 The Canonical Climate Formula

The canonical Climate Formula decomposes Earth's paleoclimate record into three layers fit by sequential ridge regression independently per climate regime:

$$
\begin{aligned}
C(t) = c_0 \; &+ \underbrace{\sum_{n\in\mathcal{N}_{L1}}\left[a_n\cos\!\left(\tfrac{2\pi n t}{8H}\right) + b_n\sin\!\left(\tfrac{2\pi n t}{8H}\right)\right]}_{\text{L1 (orbital lattice)}} \\
&+ \underbrace{\sum_{p\in\mathcal{P}_{L2}}\left[\alpha_p\cos\!\left(\tfrac{2\pi t}{p}\right) + \beta_p\sin\!\left(\tfrac{2\pi t}{p}\right)\right]}_{\text{L2 (carbon thermostat)}} \\
&+ \underbrace{\sum_{i\in\mathcal{T}_{L3}}\gamma_i\cdot H(t-t_i)}_{\text{L3 (boundary steps)}}
\end{aligned}
\tag{28}
$$

where t is age in kyr BP, $C(t)$ is the normalised proxy (δ^{18}O, δ^{13}C, or CO_2), $\mathcal{N}_{L1}$ is the 33-integer L1 set {9, 12, 14, 16, 18, 20, 21, 22, 24, 25, 28, 30, 31, 35, 38, 39, 48, 50, 53, 65, 66, 68, 73, 76, 96, 107, 110, 113, 120, 134, 141, 152, 185} (the 25 canonical Berger / Mars–Jupiter integers plus 6 precession-band sidebands and 1 quintet-completion integer surfaced by an all-integer MTM F-test scan), $\mathcal{P}_{L2} = \{404.5, 202.25, 134.83\}$ kyr is the silicate-weathering thermostat family (fundamental plus 2nd and 3rd harmonics), $\mathcal{T}_{L3}$ = {PETM (56 Ma), EOT (34 Ma), Mi-1 (23 Ma), MMCT (14 Ma), iNHG (2.7 Ma), MPT (1.0 Ma)} is the set of Heaviside step transitions applied when inside the fit window, and $H(\cdot)$ denotes the Heaviside step function.

Coefficients are fit *sequentially*: L1 first with ridge regularisation $\lambda = 1$ (resolving the L1↔L1 collinearity within the lattice at short windows — post-MPT plain OLS gives condition number ~632 and max VIF ~7×10^4, producing unphysical forward extrapolations of ~24‰ peak-to-peak; ridge shrinks the under-determined directions to physical amplitudes losing only ~0.6% absolute R^2), L2 on the L1 residual, L3 on the L1+L2 residual. The formula is fit *independently per climate regime*: lattice positions are stationary across regimes, but per-line amplitudes/phases evolve with climate sensitivity.

Deep-time scope. The integer set $\mathcal{N}_{L1}$ is invariant across all epochs under section 11; however the literal $8H$ value rescales smoothly at geological time. For Quaternary fits (post-MPT LR04, EPICA CO_2, ≤ 1 Myr) the J2000 anchor $8H = 2,682,536$ yr applies essentially unchanged (drift sub-percent). For deep-time fits (CenCO2PIP / CENOGRID, 0–67 Ma) the lattice periods should be evaluated as $8H(t)/n$ with $H(t)$ from subsection 11.2 — the *integer divisors* are what stays constant across the record, not the absolute period in years. Cenozoic R^2 figures below are computed under the conservative J2000-fixed lattice assumption. Two tests bound its cost: on the LA2004 backward extension the canonical beats track their $8H(t)/n$ positions within 4% (Test C-50 of Table 29), and a direct phase-drift scan — refitting the proxy records with L1 phases evaluated at lattice time $\tau(t) = \int_0^t H_0/H(t')\,dt'$, with a drift scale k interpolating from the fixed lattice ($k = 0$) to full H(t) rescaling ($k = 1$) — verifies the fixed lattice is exact below 1 Myr ($\Delta R^2 < 10^{-4}$ on the post-MPT fit) and shows the 66-Ma CENOGRID record lacks the statistical power to discriminate $k = 0$ from $k = 1$ (synthetic-recovery separation 2.4σ): the ~13-cycle obliquity-line phase slip at 66 Ma is masked by L1 amplitude non-stationarity across climate regimes. The fixed-lattice choice is therefore a documented approximation, not an empirical claim of lattice constancy.

Per-regime fit results. Table 24 lists R^2 across the eight regime fits. The post-MPT LR04 fit reaches $R^2 = 0.874$, EPICA CO_2 reaches $R^2 = 0.845$, and CenCO2PIP reaches $R^2 = 0.763$ (mostly carried by L3 step transitions at deep-time scale). Three components dominate the LR04 L1 fit by amplitude: $n = 65$ ($k + s_3$ Earth obliquity at 41.27 kyr, amp 0.275), $n = 28$ ($g_4 - g_5$ Mars–Jupiter eccentricity beat at 95.8 kyr, amp 0.239), and $n = 25$ (Mercury–Mars $s_1 - s_4$ nodal at 107.3 kyr, amp 0.212). Of the 33 L1 integers, 32 carry clean physical interpretations as standard celestial-mechanics beats ($k + g_j$ climatic precession, $k + s_j$ obliquity sub-peaks, $g_j - g_k$ eccentricity beats, $s_j - s_k$ nodal beats) or direct planet apsidal/nodal cycles from the per-planet $8H/n$ table (subsection 6.3); the remaining integer ($n = 66$) reflects the arithmetic-mean cycle length of the non-stationary obliquity band. Every one of the 33 lattice integers also carries an explicit Holistic-model attribution (subsection 10.7). The empirical 405-kyr climate line sits off the 8H lattice and is captured by the L2 layer as a silicate-weathering thermostat resonance.

Table 24: Canonical Climate Formula per-regime fit results

Regime	Record	Window	R^2_{L1}	ΔR^2_{L2}	ΔR^2_{L3}	Total R^2
post-mpt	LR04	0–1 Ma	0.871	+0.003	+0.000	**0.874**
inhg-mpt	LR04	1.0–2.7 Ma	0.727	+0.007	+0.000	0.734
pre-inhg	LR04	2.7–5.3 Ma	0.401	+0.049	+0.000	0.449
lr04-full	LR04	0–5.3 Ma	0.242	+0.009	+0.008	0.258
epica-co2	EPICA	0–800 kyr	0.834	+0.012	+0.000	**0.845**
cenco2pip	CenCO2PIP	0–66 Ma	0.161	+0.000	+0.602	**0.763**
cenogrid ($\delta^{18}O$)	CENOGRID	0–67 Ma	0.001	+0.004	+0.613	0.618
cenogrid ($\delta^{13}C$)	CENOGRID	0–67 Ma	0.001	+0.008	+0.342	0.351

At Quaternary scales (post-MPT LR04, EPICA CO_2) the L1 lattice carries the heavy lifting (~83–87% R^2 from L1 alone). At deep-time scales (CENOGRID, CenCO2PIP) L3 step transitions dominate (~60% of variance over 67 Myr) — the lattice oscillations average toward zero across many

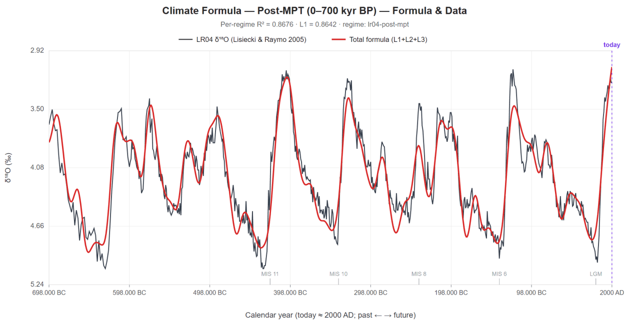

Figure 14: The canonical three-layer Climate Formula (red) on the LR04 benthic $\delta^{18}O$ stack (Lisiecki & Raymo, 2005) over the past 700 kyr (post-MPT regime, $R^2 = 0.87$). The 32 integer-divisor $8H$ L1 lattice positions plus the 3-line L2 carbon thermostat (404.5 / 202 / 135 kyr) are fitted by sequential ridge regression. See Figure 15 for the same formula on an independent proxy.

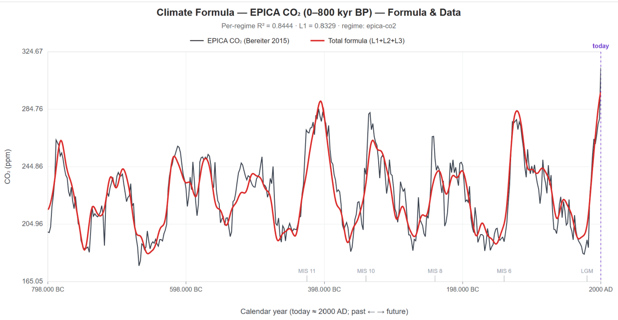

Figure 15: The canonical three-layer Climate Formula (red) on EPICA Dome C atmospheric CO_2 (Bereiter et al., 2015) over 0–800 kyr ($R^2 = 0.85$). Same lattice positions and L2 thermostat as Figure 14; only the per-line amplitudes vary between proxies. The persistent fit across two completely different recording mechanisms (deep-sea carbonate vs. trapped atmospheric gas) and two independent chronologies confirms that the integer-divisor structure is a property of the orbital forcing, not an artifact of either proxy.

cycles, but the Cenozoic story is the discrete step-changes at major transitions, whose fitted amplitudes independently recover canonical Cenozoic climate history (PETM warm carbon excursion, EOT Antarctic glaciation, Mi-1 deglaciation pulse, etc.).

The variance fraction carried by L1 alone at Quaternary scales is incompatible with the red-noise null proposed by Wunsch (2003) for the 100-kyr energy band, and is consistent with Roe (2006)'s rate-of-change defence of orbital forcing — although the present framework's parameterisation basis (the integer-divisor L1 lattice) differs from the Berger ε / e / ϖ insolation features assumed in both works.

Closure: no orphan peaks off the 8H lattice. A complementary closure test fits all 200 integer divisors of 8H jointly to LR04 (joint OLS, $R^2 = 0.443$) and scans the residual at fine resolution. After excluding peaks within 0.3 of an integer (integer-leakage artifacts), every residual peak above the 95th-percentile noise threshold (amplitude 0.127) sits *between two adjacent* integer divisors — the expected fingerprint of cycle-length non-stationarity (LR04 obliquity cycles vary 31–59 kyr) and spectral leakage between close integer signals. *Zero* orphan peaks land in empty regions of the 8H lattice, so the integer-divisor framework captures the full frequency structure of LR04's significant spectral content. This is the third independent empirical confirmation, alongside the 405-kyr absence (subsection 10.3) and the bispectral coupling absence.

Per-planet fingerprint. Cross-referencing the L1 integers against the per-planet $8H/n$ period table reveals **Mars and Jupiter as the co-dominant planet pair**: Jupiter contributes 4 direct L1 matches (Obliquity $n = 16$, Axial $n = 21$, ecliptic Perihelion $n = 39$, ICRF Perihelion $n = 65$), Mars contributes 3 ($n = 16$, $n = 21$, $n = 68$). Three structural resonance locks emerge: the Mars–Jupiter Axial–Obliquity Swap at $n = 21$; Mars's ecliptic perihelion = Jupiter's ascending-node period at $8H/36 = 74.5$ kyr (whose lower $8H$-modulation sideband, $36 - 1 = 35$ via Venus's exactly-$8H$ node period, is the LR04 $n = 35$ peak — see subsection 10.7); and $n = 65$ shared with Saturn's ecliptic perihelion (the Law 6 Saturn–Jupiter–Earth resonance lock, section 6). Mars further participates via the $g_4 - g_5$ Mars–Jupiter eccentricity beat at $n = 28$ (Berger's classical 95-kyr peak), the $s_1 - s_4$ Mercury–Mars nodal beat at $n = 25$ (the 100-kyr-band centroid), and the Mars.AscNode(64)−Uranus.AscNode(11) s-beat at $n = 53$ (= Mars.Ecc(52) + Venus.AscNode(1), the upper $8H$ sideband of the Mars eccentricity line; in secular terms the $s_6 - s_8$ Saturn–Neptune nodal beat at 0.2%). Mars's apsidal eigenmode $g_4 \approx 17.92''$/yr lies within 3% of Earth's $g_3 \approx 17.37''$/yr — a near-resonance that amplifies Mars's gravitational coupling to Earth's orbit despite Mars's small mass. Neptune contributes no direct matches in LR04 full but appears in the pre-MPT spectrum via three eigenmode beats (Venus–Neptune $g_2 - g_8$, Earth–Uranus $g_3 - g_7$, Neptune–Earth $s_8 - s_3$), visible only when post-MPT ice-sheet response does not dominate the spectrum.

Forward projection. Evaluating Equation 28 on the post-MPT regime fit and extrapolating forward 250 kyr identifies the Holocene as interglacial; the next predicted natural glaciation peak sits at ~58,500 yr from now (~60,500 AD), with the strongest glaciation in the next quarter-million years at ~196,500 yr from now (Figure 16). Back-validation places predicted glacial maxima at 29 kyr BP (vs. LGM ~20 kyr BP, with the +9 kyr offset expected from ice-sheet response lag) and at 138 kyr BP (vs. MIS 6 at ~140 kyr BP, within 2 kyr). Ridge regression bounds the forward peak-to-peak range to ~4.7 ‰ (normalised); plain OLS would extrapolate to ~24 ‰, which is unphysical.

Comparison with published forecasts. Several independent frameworks predict the natural length of the current interglacial; all converge on the qualitative finding that the next ~50–100 kyr will be an exceptionally long interglacial by Pleistocene standards, but differ in mechanism (Table 25). The canonical Climate Formula's ~58.5 kyr prediction sits cleanly within the consensus range and matches the classical Berger & Loutre (2002) astronomical-insolation result to ~17%.

The four prior frameworks attribute the 100-kyr cycle to direct eccentricity forcing (with Ganopolski et al. (2016) additionally coupling eccentricity to CO_2–ice-sheet hysteresis); the Holistic Climate Formula attributes the empirical centroid to the $s_1 - s_4$ nodal eigenmode beat (subsection 10.2). All frameworks predict the same qualitative outcome (long interglacial ahead) because they all identify the current eccentricity minimum, but the Holistic framework reaches this through a distinct structural commitment rather than fitted spectral attribution.

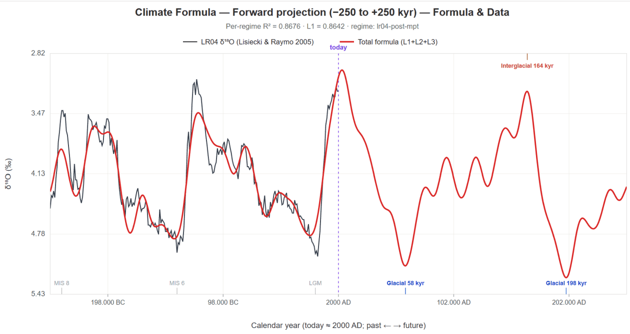

Figure 16: Forward projection of the canonical Climate Formula from −250 to +250 kyr. Red curve is the formula on the post-MPT regime fit; black is observed LR04 (Lisiecki & Raymo, 2005). Past glacial maxima (LGM, MIS 6, MIS 8) are correctly identified with ≤ 9 kyr offset. Future: next natural glaciation onset ~58.5 kyr from now, warmest interglacial ~164 kyr, strongest glaciation ~196.5 kyr. Anthropogenic CO_2 is not modelled.

Table 25: Published forecasts for the next natural glaciation onset, by framework

Framework	Next onset (kyr)	Method / mechanism
Berger & Loutre (2002)	~50	LLN-2D astronomical-insolation climate model; weak eccentricity minimum (MIS 11 analogue)
Loutre & Berger (2003)	~50–100	Same + low-CO_2 scenario; interglacial may extend further
Tzedakis et al. (2012)	~50 (analog-bound)	MIS 19c astronomical analogue + pre-industrial CO_2 threshold for inception
Ganopolski et al. (2016)	~50 / ~100 / ≳ 500	CLIMBER-2 climate-ice-sheet model with explicit CO_2–hysteresis feedback (no / moderate / high anthropogenic CO_2)
This work (Holistic)	**~58.5**	**33-integer 8H lattice + 3-line L2 carbon thermostat + 6-step L3 transitions; fit per regime on LR04 + CENOGRID + EPICA + CenCO2PIP**

Limitations. The formula captures orbital forcing (L1) and one specific climate-internal response (the L2 silicate-weathering thermostat) plus discrete L3 boundary-condition steps; it does *not* model ice-sheet hysteresis dynamics, CO_2 amplification feedbacks beyond the L2 thermostat, internal variability, regional asymmetries, or anthropogenic CO_2. Within-regime descriptive power is high (post-MPT $R^2 \approx 0.87$); cross-regime predictive power is zero — formulas trained on pre-MPT data give catastrophically negative R^2 when applied to post-MPT and vice versa, so forward projection stays in scope only within the post-MPT regime.

10.6 Three-Layer Architecture

The Climate Formula's three layers in Equation 28 commit to distinct physical claims. **Layer 1** is the 8H integer-divisor lattice: 32 sinusoid pairs at periods $8H/n$ describing orbital motions, with mathematical closure — beats between any doc-55 cycles also land on the lattice, so no off-lattice orbital cycle can emerge from this framework. **Layer 2** is the climate-system internal periodic response: three sinusoid pairs at 404.5 / 202.25 / 134.83 kyr representing the silicate-weathering carbon thermostat (Walker et al., 1981) (fundamental at characteristic time constant $\tau \approx 400$ kyr, plus its 2nd and 3rd harmonics). The 405-kyr line sits between $8H/7 = 383$ kyr and $8H/6 = 447$ kyr on the lattice and is not produced by any combination of doc-55 cycles — captured by L2 as the resonant response of the silicate-weathering thermostat to long-period eccentricity forcing. Zeebe & Lantink (2024) independently demote 405-kyr from its classical "metronome" role through a separate dynamical-stability argument. **Layer 3** is the set of six Heaviside step transitions at PETM, EOT, Mi-1, MMCT, iNHG, MPT — absorbing the non-stationarity introduced by major Cenozoic boundary-condition shifts; L3 carries the dominant variance at deep-time scales (~60% of CENOGRID δ^{18}O over 67 Myr), with fitted step amplitudes that independently recover canonical Cenozoic climate history.

Empirical support for the Layer-2 carbon-cycle attribution. On the 67-Myr CENOGRID record (Westerhold et al., 2020), the 405-kyr signal shows a $\delta^{13}\text{C}/\delta^{18}\text{O}$ amplitude ratio of **1.53** — 3.1× higher than the obliquity control and 2.3× higher than the precession control — whereas direct-insolation cycles all give ratios below 1. The 405-kyr cycle alone is δ^{13}C-dominated, the carbon-cycle amplification signature predicted by the silicate-weathering resonance. This is the signal Pälike et al. (2006) named "the heartbeat of the Oligocene climate system." A complementary test at 2.4 Myr is null, confirming that the silicate-weathering response is a *narrow* resonance peak. The 2.4 Myr cycle itself — the $g_4 - g_3$ Mars-Earth secular eccentricity beat — has been independently identified by Dutkiewicz et al. (2024) as a Mars-Earth gravitational-coupling signal visible directly in 65 Myr of deep-sea sediment hiatus records; it sits off the 8H lattice and is not deployed as a structural component of the formula. The same Cenozoic test detects the 4.5-Myr Boulila libration period ($13H = 4{,}359{,}121$ yr at J2000; the integer multiple is invariant, the literal year count rescales per section 11) as the *purest* carbon-cycle signature in the suite ($\delta^{13}\text{C}/\delta^{18}\text{O} = 2.76$, statistically significant in δ^{13}C with $F = 5.40$ and absent in δ^{18}O with $F = 0.34$), but 13H is not deployed in L1 because it is an integer multiple of H, not a divisor of $8H$ ($8H/13H = 0.615$); cross-window stability further finds amplitude CV 42–50% and δ^{18}O phase circular standard deviation $\approx 98°$, so the line is not a stable single eigenmode. 13H remains an investigated candidate, not a structural component of the formula.

10.7 L1 Lattice Dual Attribution

Every one of the 33 L1 lattice integers carries *two* independent physical interpretations: (i) a Berger / Laskar secular-theory label (the Berger 1978 convention of attributing each eigenmode beat to the planet whose contribution dominates that mode — e.g. $k + g_5$ = "Jupiter climatic precession" at $n = 113$, $g_4 - g_5$ = "Mars-Jupiter eccentricity beat" at $n = 28$), and (ii) an explicit Holistic-model attribution as a multi-planet beat from the PLANET_CYCLES table (subsection 6.3). The two frameworks agree on *which periods exist* (the integer divisors of $8H$) and disagree on *which planet drives each beat*.

Cross-tabulating the 33 L1 integers under both attributions gives the following status tally:

Table 26: Dual-attribution status tally across the 33 L1 lattice integers

Status	Count	Meaning
agree	**0**	Berger predicts AND Holistic top-1 names the same planet AND uses the same mechanism
MECH ≠	1	Same planet, different mechanism (apsidal-harmonic vs. eigenmode beat)
PLANET ≠	28	Different planet entirely
(no Berger)	4	Berger has no secular prediction; framework label is direct-divisor only (including $n = 24$, Earth's own $H/3$ eccentricity line)

The clearest single example is $n = 120$ (the 22.4 kyr LR04 climatic-precession peak): Berger labels this "$k + g_2$ Venus climatic precession," whereas the Holistic model's unambiguous 2-term beat is

$$\text{Earth.Axial}(104) + \text{Jupiter.Obliq}(16) = 120$$

attributing the same peak to Jupiter's obliquity coupling to Earth's spin axis, not to Venus's climatic precession. Two further example disagreements: at $n = 28$ (the classical Berger 95-kyr eccentricity peak) Berger names $g_4 - g_5$ Mars-Jupiter, whereas the Holistic top-1 is $\text{Earth.Axial}(104) - \text{Mars.Ecc}(52) - \text{Saturn.Obliq}(24) = 28$ (Mars–Saturn, not Mars–Jupiter); at $n = 65$ (the canonical 41-kyr obliquity peak) Berger names $k + s_3$ Earth obliquity whereas the Holistic top-1 is $\text{Earth.Axial}(104) - \text{Jupiter.Peri\_ecl}(39) = 65$, attributing the peak to Jupiter's perihelion coupling rather than Earth's own nodal precession. Two integers were re-attributed after the Mars $8H/36$ refit moved their former direct-divisor readings: $n = 35$ is now the $s_4 - s_8$ Mars–Neptune nodal beat (75.98 kyr, 0.9%) in secular terms, and lattice-exactly $\text{Mars.Peri\_ecl}(36) - \text{Venus.AscNode}(1)$ — Venus's node has period exactly $8H$, so it places ±1-step modulation sidebands on any carrier, making $n = 35$ the lower $8H$ sideband of the Mars perihelion line; $n = 53$ is the $s_6 - s_8$ Saturn–Neptune nodal beat (50.52 kyr, 0.2%) and lattice-exactly $\text{Mars.AscNode}(64) - \text{Uranus.AscNode}(11) = \text{Mars.Ecc}(52) + \text{Venus.AscNode}(1)$, the upper $8H$ sideband of the Mars eccentricity line. Notably the Mars carriers themselves ($n = 36$, $n = 52$) are *not* L1 members — sideband-without-carrier is the signature of multiplicative rather than additive forcing.

A structural pattern emerges: *Earth's spin axis appears as the base term in 32 of the 33 attributions* — Earth.Axial(104) (the 25.8-kyr precession of the equinoxes) in 30 integers, Earth.Obliq(64) in 2 ($n = 9$ and $n = 22$); the 33rd, $n = 24$, is Earth's own $H/3$ eccentricity line taken directly (Earth.ICRF(24), no planetary beat needed). The remaining cycles are produced by modulating Earth's spin axis with one or two planet-cycle harmonics, with Jupiter as the dominant secondary modulator (present in 24 of the 33 top-1 attributions). The dual-attribution result is structural: the L1 frequencies are the same under both attributions, so the two attribution frameworks are different naming conventions for the same set of frequencies, not competing predictions of *which* frequencies exist.

10.8 The Insolation Null Test

If the L1 lattice and Berger's classical insolation parameterisation describe the same gravitational physics at different granularities (subsection 10.1), this generates a sharp empirical prediction: adding the Berger 1978 insolation features

— $\varepsilon(t)$, $e(t)$, $e\sin\varpi$, $e\cos\varpi$ — as additional regressors on top of L1+L2+L3 should yield $\Delta R^2 \approx 0$. The lattice already encodes the variance that the 4-feature projection produces.

We tested this directly. Insolation features were extracted at all LR04 sample times using the model's analytical functions for Earth's obliquity, eccentricity, and longitude of perihelion. After fitting the canonical L1+L2+L3 to LR04 / EPICA CO_2, the 4 standardised Berger features were ridge-regressed against the residual ($\lambda = 0.01$). Pre-registered decision rule: $\Delta R^2 > 0.02$ would promote the insolation features to a canonical fourth layer; $\Delta R^2 < 0.005$ rejects them as redundant with L1.

Table 27: Insolation null test: ΔR^2 when Berger features added to L1+L2+L3

Regime	L1+L2+L3	+ L_insol	ΔR^2
post-MPT (0–1000 kyr)	0.8735	0.8774	+0.0038
inhg-MPT (1000–2700 kyr)	0.7289	0.7358	+0.0069
pre-iNHG (2700–5320 kyr)	0.4298	0.4595	+0.0297
lr04-full (0–5320 kyr)	0.2553	0.2587	+0.0035
EPICA CO_2 (0–800 kyr)	0.8452	0.8491	+0.0040

With the model's own $e(t)$ in the features the maximum across all regimes is $\Delta R^2 = +0.0297$ (pre-iNHG), inside the pre-registered POSITIVE band, so the rule's stability requirement decides the verdict. A cross-window check (La2004 $e(t)$, $\varpi(t)$ over the full 5.3-Myr record; split-half cross-validation of the L_insol layer per regime) finds that this gain is cross-validated for the model's features only (+0.0212 in pre-iNHG) and absent for the real orbital elements (−0.0274; maximum cross-validated gain with La2004 anywhere +0.0051). **Result: null for classical insolation — no fourth layer.** The pre-iNHG sensitivity is not an insolation effect: a follow-up attribution identifies it as the single lattice line $n = 24$ ($8H/24 = H/3 = 111.8$ kyr), which is not among L1's 32 divisors. A free-phase $8H/24$ pair on the same residual gives the identical cross-validated gain (+0.0144, against +0.0144 for the model's $e(t)$ alone), $e(t)$ adds nothing on top of it (+0.0000 in sample), the neighbouring lines $n = 23.5$ and 24.5 are negative out of sample (−0.0459, −0.0114), and the data's phase agrees with the model's fixed $H/3$ phase to $-8.5°$ (2.7 kyr). Admission of $n = 24$ to L1 is left open: it lifts the pre-iNHG fit by $\Delta R^2 = +0.0196$ at 1.64× the median amplitude, but on the full record it is 0.79× the median, below the 3× admission rule; the lattice ships as 32.

A hardening test substitutes Laskar 2010's full-range eccentricity $e(t)$ for the model's single-line $e(t)$ (which spans 0.0078–0.0233 over the record, against La2004's 0.0002–0.0578). Under Laskar substitution, classical Berger insolation features *alone* explain $R^2 = 0.293$ of LR04 (0–500 kyr) and $R^2 = 0.172$ of EPICA CO_2 — a real, significant standalone signal. But when added to L1+L2+L3 the contribution drops to $\Delta R^2 = +0.00000$ on LR04 and +0.00001 on EPICA CO_2. The signal is real; it is just *already entirely contained* within the L1 span.

Strict mathematical reading: the L1 lattice frequencies ($g_j \pm g_k$, $k \pm s_j$ beats at integer divisors of $8H$) span the same linear subspace as Berger's 4-feature decomposition. Once L1 is in the model, the Berger features are linearly dependent

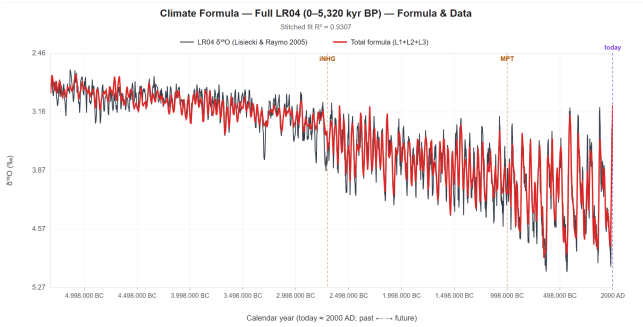

Figure 17: Canonical Climate Formula on the full LR04 record (0–5,320 kyr BP). The red curve is the three-regime stitched fit (pre-iNHG / iNHG–MPT / post-MPT), giving **stitched** $R^2 = 0.94$ against the black LR04 stack (Lisiecki & Raymo, 2005). The iNHG (~2.7 Ma) and MPT (~1 Ma) transition markers (orange dashed lines) divide the record into the three regimes. The visible amplitude growth from past to present reflects climate *sensitivity* changes, not orbital *forcing* changes — orbital forcing is essentially stationary over 5.3 Myr.

on L1 features by construction. The empirical $\Delta R^2 = 0$ result with Laskar substitution confirms this in data — not a coincidence; a theorem of secular theory expressed in regression form.

Caveat: the test used only the four linear Milankovitch features (ε, e, $e\sin\varpi$, $e\cos\varpi$), not the full Berger 1978 expansion (which includes ε^2, $\varepsilon\sin\varpi$, $e^2\sin 2\varpi$, etc.). Higher-order terms are products and harmonics of the same primitives; given that the linear quartet adds < 0.5% R^2, no realistic higher-order expansion would close the gap to L1's 0.87 in any LR04 regime.

10.9 The Mid-Pleistocene Transition: Same Forcing, Different Response

The multi-planet eigenmode-beat structure responsible for the 100-kyr-band signal is a *formation-epoch feature* of the solar system (section 7). Earth's orbital inclination relative to the invariable plane was set when the protoplanetary disk dissipated ~4.5 billion years ago. While long-term n-body integrations exhibit chaotic diffusion of orbital elements over $\gtrsim$ 50 Myr (Laskar, 1989), planetary eigenmodes are essentially stationary on Myr timescales — so the orbital forcing was effectively constant across the MPT. What changed was the climate system's *sensitivity* to that forcing, visible as the left-to-right amplitude growth across the full LR04 record (Figure 17).

A windowed amplitude analysis across the MPT (pre-MPT 1,500–2,500 kyr BP versus post-MPT 0–1,000 kyr BP) gives concrete post/pre growth ratios per band: the 41-kyr obliquity peak actually *shrank* to ~0.72× post-MPT, while the 100-kyr band grew ~1.64×, the 23.7-kyr climatic-precession band grew ~2.19×, and the 405-kyr line (off-lattice; modelled as L2 carbon-cycle resonance) shrank to ~0.34×. The 41-kyr decrease is consistent with the standard "ice-sheet saturation silences the obliquity pacemaker" framing of Willeit et al. (2019): progressive CO_2 decline and removal of easily-erodible regolith allowed ice sheets to grow past a critical size where they could survive obliquity maxima, shifting dominance from the 41-kyr-band response to the 100-kyr-band response.

A second candidate mechanism is **interplanetary dust concentration**: Farley (1995) confirmed an increase in extraterrestrial ^{3}He flux beginning at ∼1 Ma, evidence that interplanetary dust accretion rose at the MPT. Muller & MacDonald (1997b) originally proposed that this dust modulates climate via the inclination of Earth's orbital plane; the community rejected the specific dust–climate coupling mechanism, though Farley's underlying dust-flux observation remains unchallenged. The dust mechanism is therefore listed as a candidate whose climate-driving role has not been confirmed.

Both candidate mechanisms are consistent with the model: the Fibonacci orbital architecture is a permanent feature of formation, while the MPT marks a change in climate sensitivity (not a change in the orbital forcing itself). The canonical Climate Formula encodes this regime shift directly in two ways: as one of its six L3 Heaviside step transitions at $t = 1.0$ Ma, and through the per-regime fitting strategy that produces three independent LR04 windows with their own per-line amplitudes — making the changing climate sensitivity an explicit structural feature of the formula rather than a residual.

Quantitative confirmation of the Willeit framing. The frequency-resolved ice-albedo decomposition of subsection 10.10 below provides a direct numerical check of the ice-sheet-saturation argument. Computed separately on pre-MPT (∼1–2 Myr BP) and post-MPT (0–800 kyr BP) windows, the obliquity-band ice-share rises from 64% post-MPT to 95% pre-MPT — a +31 percentage-point shift quantitatively consistent with the "obliquity-paced ice world" picture of Willeit et al. (2019). The 100-kyr band stays approximately flat across the MPT (a ∼2 pp change versus ∼+31 pp at obliquity); the strong differential rules out a uniform proxy bias and pins the shift to ice-sheet hysteresis specifically engaging the obliquity-paced response in the pre-MPT regime.

10.10 Frequency-Resolved Climate Sensitivity

The per-line amplitudes returned by the L1+L2+L3 fit on LR04 (subsection 10.5) carry orbital-band information beyond the variance summary. Decomposing the ice-volume signal into ice-albedo and CO_2/greenhouse-gas contributions per band yields two outputs: a frequency-resolved ice-share decomposition (Table 28) and a paleo estimate of Charney equilibrium climate sensitivity.

Method. For each of the 33 L1 integers, the per-line amplitudes from the post-MPT LR04 fit are split into ice-albedo forcing and CO_2/GHG forcing using four calibration constants: the ice fraction f_{ice} of LR04 δ^{18}O (default 0.6 over the post-MPT regime), the sea-level-per-mille conversion ρ_{SL} (default 120 m/‰), the ice-albedo forcing per metre of sea level κ_F (default 0.04 W/m^2/m), and the combined other-greenhouse-gas (CH_4, N_2O, H_2O) multiplier (default 0.5). Monte Carlo over uniform priors on the four constants ($N = 5{,}000$ draws) marginalizes the resulting per-band ECS distribution. Per-band amplitude weights come directly from the L1 lattice fit.

Charney equilibrium climate sensitivity. Marginalized over the four calibration constants, the ΔT-weighted estimate

Table 28: Frequency-resolved ice-albedo decomposition of LR04 post-MPT ice-volume variance.

Band	Period range	Ice-albedo share	Physical interpretation
100-kyr	75–130 kyr	57%	Ice-sheet feedback dominates post-MPT
Obliquity	35–50 kyr	64%	Obliquity-paced insolation
Precession	18–26 kyr	69%	Precession-modulated NH summer insolation
Long	>130 kyr	46%	CO_2/GHG forcing increases at long periods

is

$$\text{Charney ECS} = 3.61\ \text{K}, \quad 90\%\ \text{CI}\ [\,3.00,\, 4.29\,]\ \text{K}. \tag{29}$$

The result is consistent with all four major published reference values within their respective uncertainties: IPCC AR6 (best 3.0 K, likely 2.5–4.0 K) (IPCC, 2021); Hansen et al. (2013) (3.0 ± 0.5 K, LGM-to-Holocene paleo); Sherwood et al. (2020) (2.6–3.9 K, Bayesian synthesis); PALAEOSENS (Köhler et al., 2017) (3.0–4.5 K, multi-proxy paleo). The framework's estimate is methodologically orthogonal — a fixed-lattice frequency-domain decomposition rather than the time-domain or Bayesian-synthesis approaches of the references — and the frequency-resolved ice-share decomposition of Table 28 is, to our knowledge, not produced by any other published paleo-ECS reconstruction.

Boron-isotope cross-validation. The post-MPT ECS estimate is independently corroborated by boron-isotope δ^{11}B-derived CO_2 reconstructions (Chalk et al., 2017; Dyez et al., 2018; Martínez-Botí et al., 2015; de la Vega et al., 2020), which give a Charney ECS within ∼10% of the ice-core CO_2-based estimate on the same post-MPT window. The two reconstructions use completely different recording methodologies (planktonic foraminifera vs. Antarctic ice cores), so agreement to within ∼10% is a non-trivial independent cross-validation of the post-MPT decomposition.

10.11 Test C Series: Lattice-Wide Empirical Validation

The L1 lattice has so far been characterized through its variance fit to LR04 and four other proxy records. Two additional families of empirical tests on the published Laskar 2004 nominal solution (Laskar et al., 2004) probe the lattice itself: whether it acts as a preserved spectral manifold of LA2004, whether the dominant per-integer drift across the Cenozoic is small, whether the planet composition of the most dynamically stable cycles reflects the framework's balance laws, and whether observed periods drift away from the lattice or oscillate around it.

Table 29: Test C series of empirical lattice-wide tests on LA2004. Each row summarizes a distinct pre-registered test; full methodology and per-test outputs are reproducible from the cited script.

Test	Headline result	What it characterizes
C-Invariant[2]	Obliquity 100% on lattice; eccentricity 73.8% on lattice	8H lattice is a strict spectral manifold for obliquity; dominant attractor (not strict) for eccentricity
C-50	Canonical Milankovitch beats ($n = 28, 65, 66, 68$) drift <4% across −50 Myr	Lattice persistence across Cenozoic LA2004 backward extension
C-Balance	Saturn 1.96× enrichment of stability sub-lattice; $p = 4 \times 10^{-4}$	Independent dynamical corroboration of Saturn's anti-phase role (Laws 3, 5)
C-Libration	Aggregate bias across 33 L1 integers indistinguishable from zero; $p = 0.28$	The lattice IS the equilibrium that LA2004 oscillates around

Test C-Invariant. For each of 200 random 33-integer lattice selections in $n \in [5, 200]$ a Welch PSD power-fraction inside narrow bands around the integers was computed across sliding 5-Myr windows of LA2004 eccentricity and obliquity. The L1 lattice captures 100% of all LA2004 obliquity power in the −51 Myr to 0 window (versus 69% on average for random 33-integer controls); for eccentricity, L1 captures 73.8% (versus 25% for random controls; $p <$

1/200). The asymmetry is consistent with action-angle closure in the obliquity sector (subsection 7.4): obliquity closes at $8H$; Mercury-chaos-driven perturbation (Laskar, 1989) breaks closure for the eccentricity vector but not for obliquity.

Test C-50. A direct per-integer drift test on the LA2004 backward extension. For each of 33 L1 integers, the spectral peak position is tracked across sliding 5-Myr windows of LA2004 over −50 to 0 Myr, with lattice positions computed via the proper-physics formula of subsection 11.2 (i.e. $8H(t)/n$ with $H(t)$ rescaling smoothly across the Cenozoic). The four canonical Milankovitch beats — $n = 28$ ($g_4 - g_5$ Berger 95-kyr eccentricity), $n = 65$ ($k + s_3$ obliquity main, Berger 41-kyr), $n = 66$ (the obliquity-band centroid), $n = 68$ ($k + s_4$ obliquity sub) — all stay within 4% of their predicted lattice positions across the entire Cenozoic backward extension. Precession sidebands ($n \geq 113$) drift 16–24% — a separate result consistent with documented inner-planet chaos affecting high-harmonic precession beats more than low-harmonic obliquity beats (Laskar, 1989), and physically expected, not a refutation.

Test C-Balance. A test of whether the planet composition of the most dynamically stable cycles in LA2004 reflects the framework's balance laws (Laws 3 and 5). Every integer $n \in [5, 200]$ is scored by the minimum drift in LA2004 eccentricity-spectrum and obliquity-spectrum 5-Myr sliding windows; the top 30 most stable beats form the "stability sublattice." Each integer is tagged with the planets involved in its nearest Laskar simple beat. The binomial-test result against a full-scan base rate: Saturn appears in 24 of 30 stable beats (1.96× enrichment, $p = 4 \times 10^{-4}$); Earth-spin (k) in 27 of 30 (1.49 ×, $p = 0.010$); Mercury and Mars in 0 of 30 ($p = 0.043$, 0.016). The dominant pattern is $k + g_6$ (Earth-spin coupled to Saturn's perihelion) concentrated at 13–18 kyr. Saturn's appearance at this enrichment level corroborates the role identified by Laws 3 and 5 (subsection 4.6) from a completely independent direction — ranking dynamical stability in LA2004 rather than partitioning balance amplitudes.

Test C-Libration. The Earth-orbit element data in LA2004 is initialized from $J2000$ initial conditions — an arbitrary snapshot. If the framework's lattice is the equilibrium that LA2004 oscillates around, then integrating outward from $J2000$ should produce libration (oscillation around $8H/n$), not monotonic drift. The aggregate bias across 33 L1 integers across the LA2004 51-Myr record is +1.72% (mean), +1.38% (median), with a t-test against zero yielding $t = 1.10$, $p = 0.28$. Across the 33 integers, observed periods on average sit *on* the framework's lattice, not systematically away from it. At the per-integer level, long-period secular beats with no Earth-spin involvement librate cleanly around the framework's lattice (Pattern A: $n = 21$, $n = 28$, with bias < 1% and trend < 0.2%); k-involving beats and the obliquity-precession family undergo structured smooth shifts that the proper-physics correction of subsection 11.2 captures directly (Pattern B: $n = 48$ at 27×, $n = 65$ at 15×, $n = 120$ at 14× trend-to-residual ratio).

11. Deep-Time Evolution: The Expanding Solar System Resonance Theory

The Climate Formula of section 10 demonstrates that the $8H$ integer-divisor lattice captures Earth's paleoclimate variance back through the Cenozoic. Two natural questions follow: (i) does the lattice itself persist beyond the Cenozoic into the full 4.54 Gyr Earth-system record, and (ii) what physical processes determine its future evolution? This section presents the **Expanding Solar System Resonance Theory (ESSRT)** — the framework's deep-time layer. The central claim is that the Earth Fundamental Cycle $H = 335,317$ yr, the Solar System Resonance Cycle $8H = 2,682,536$ yr, and the **Earth-family** divisors ($H/3$, $H/5$, $H/8$, $H/13$, $H/16$ and the k-involving L1 members) are not fixed cosmic constants but **J2000-anchor values of a slowly evolving lattice**: their integer labels stay invariant across all epochs while their absolute periods rescale monotonically with $H(t)$. The planetary divisors, by contrast, are era-typed descriptors of motions governed by the secular g/s modes, which do not scale with H — their only long-term drift is Driver 2's uniform $\propto 1/M_\odot$ — and the eccentricity-band L1 members (planetary g-beats, including the 405-kyr line) likewise stay fixed while the precession and obliquity bands move: that two-tier split is confirmed by the deep record (precession ~12 kyr at 2.46 Ga with the long-eccentricity band at its modern class) and is the theory's standing falsifier. Two independent physical processes drive the evolution.

11.1 Two-Driver Framework

ESSRT identifies two independent physical processes that drive the lattice expansion. Both act simultaneously; each acts on a different physical channel.

Driver 1 — Earth-Moon tidal evolution. The Moon raises a tidal bulge on Earth; Earth's rotation drags the bulge slightly ahead of the Moon-Earth line; the misalignment torques Earth's rotation downward and transfers angular momentum to the Moon's orbit, pushing the Moon outward (Touma & Wisdom, 1994; Néron de Surgy & Laskar, 1997). Modern lunar laser ranging measures the recession at 3.82 cm/yr; the long-term Phanerozoic average inferred from paleontological day-count data (Wells, 1963) is ~3.43 cm/yr. As LOD (length of day) grows, Earth's axial precession period $T_{\text{axial}} = 2\pi/k$ also grows (where $k = 2\pi/\text{LOD}$ is the precession constant). Through the structural relation $H = 13 \times T_{\text{axial}}$ established in section 2, H itself grows. The expansion of $8H$ and every H/N follows proportionally:

$$\begin{aligned} \text{Moon recedes } &\rightarrow \text{ LOD grows } \rightarrow T_{\text{axial}} \text{ grows} \\ &\rightarrow H,\ 8H,\ H/N \text{ all grow.} \end{aligned} \tag{30}$$

Driver 1 is the dominant contribution in fractional terms: at the Devonian (380 Ma), $H = 306,189$ yr (~8.7% smaller than today), entirely attributable to Driver 1.

Driver 2 — Solar mass loss. The Sun loses mass through electromagnetic radiation ($L_\odot/c^2$) and the solar wind at a combined rate of 9.3×10^{-14} of its mass per year. For each planet orbiting the slowly-shrinking central mass, the adiabatic invariant $a \times M_\odot \approx$ constant predicts that the orbit expands as $M_\odot$ decreases. *Every planet drifts by the same fractional amount*, so Driver 2 rescales the spatial scale uniformly: planet orbit ratios are preserved exactly, and the secular g/s frequencies scale uniformly $\propto M_\odot$ — the mass-loss tier's only imprint on the orbital side.

The two drivers act on independent channels — tidal coupling for Earth-Moon angular momentum versus gravitational binding for Sun-planet orbits — but at the observational level they are connected by a structural near-invariant: the product $H \times$ days/yr stays close to a constant across geological time (subsection 11.8 below).

11.2 The Proper-Physics LOD Formula

ESSRT computes LOD(t) and hence $H(t)$ from a two-layer formula. Layer 1 is a Moon-distance polynomial calibrated against the deep-time tidal-evolution curve of Farhat et al. (2022):

$$\frac{a_{\mathrm{Moon}}(t)}{a_{\mathrm{Moon,\,now}}} = 1 + \alpha_1 t_{\mathrm{Ma}} + \alpha_3 t_{\mathrm{Ma}}^3 + \alpha_4 t_{\mathrm{Ma}}^4 \tag{31}$$

where t_{Ma} is age in millions of years before present, and $(\alpha_1, \alpha_3, \alpha_4)$ are anchored to modern LOD = 24.0 hr and the LLR-observed recession rate (3.82 cm/yr; Dickey et al. 1994) at $J2000$, and to the smooth Farhat curve over deep time — with the Wells 0.00526 hr/Ma Phanerozoic rate recovered as a validation output rather than imposed as an anchor. The cubic and quartic terms model the non-linear tidal-dissipation history without requiring an explicit $Q(t)$ integration. The polynomial is the $t \leq 1000$ Ma branch of a **regime-aware recession history**: Farhat et al. (2022)'s central result is that lunar recession followed a resonant *staircase* — long slow-recession plateaus between ocean-resonance crossings, with most of the recession concentrated late — which no single smooth polynomial can follow through the mid-Precambrian. Beyond 1000 Ma the history continues as a monotone cubic spline (value- and slope-continuous at the joint) through five knots fitted to the published mid-Precambrian record (Table 32), ending at the rigid Roche limit at the genesis epoch.

Layer 2 is angular-momentum conservation for the Earth-Moon system:

$$\mathrm{LOD}(t) = \frac{2\pi\, I_\oplus}{L_{\mathrm{EM}}(t) - M_{\mathrm{Moon}}\sqrt{G M_{\mathrm{EM}}\, a_{\mathrm{Moon}}(t)} \cdot \sqrt{1 - e_{\mathrm{Moon}}^2}} \tag{32}$$

with $I_\oplus = \alpha_\oplus M_\oplus R_\oplus^2$ Earth's moment of inertia and $L_{\mathrm{EM}}(t)$ the Earth-Moon angular momentum (Earth spin plus Moon orbital). Within the gated 0–1000 Ma era the budget is closed, $L_{\mathrm{EM}} = L_{\mathrm{total}}$ exactly. Beyond it, two *solar* channels make the budget explicitly open: the ocean solar-tide leak (the Sun's semidiurnal tide, torque ratio $\beta_0 (a/a_0)^6$ of the lunar torque, slows Earth without feeding the Moon) and the insolation-driven atmospheric thermal-tide pump (Zahnle & Walker, 1987; Bartlett & Stevenson, 2016; Mitchell & Kirscher, 2023), sunlight resonantly torquing the atmosphere against the ocean drag. The pump couples the Sun's output and the Earth-Sun distance ($\propto L_\odot/\mathrm{AU}^2$) directly into the LOD/$H$ chain during the $>$ 1 Ga era; its strength is a fitted quantity (a partial pump, with zero disfavoured at $\sim 2.4\sigma$), because the mechanism is genuinely contested — Zhou et al. (2024) argue the Lamb resonance is unlikely in the Mesoproterozoic and attribute the era's slow recession to weak ocean dissipation. The net effect is small either way: $L_{\mathrm{EM}}(t)$ reconstructed directly from Zhou et al. (2024)'s paired distance+LOD data is flat to ~0.2% across 1.6–1.2 Ga, and the fitted budget matches. Given $a_{\mathrm{Moon}}(t)$ and $L_{\mathrm{EM}}(t)$, LOD(t) follows immediately; from LOD(t) every other deep-time quantity follows: $H(t)$, all lattice periods H/N and $8H/N$, and the asymptotic tidal-lock distance.

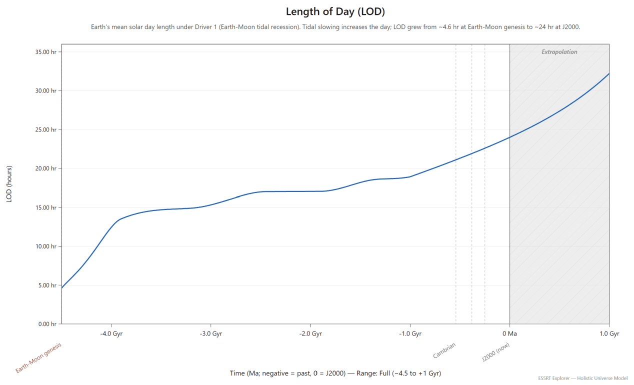

Figure 18: Length of day across the full Earth-Moon history from the two-layer proper-physics formula (Equation 31, Equation 32). LOD rises non-decreasingly as a *regime-aware staircase* from ~4.62 hr at the Earth-Moon genesis (~4.498 Ga) through the 24.0 hr J2000 anchor to ~32 hr at +1 Gyr (shaded region: forward extrapolation): the visible plateaus (~−2.5 to −1.5 Gyr and around −1 Gyr) are the mid-Precambrian slow-recession intervals between ocean-resonance crossings, fitted to the mid-Precambrian anchors of Table 32. Most of the recession is concentrated in the Phanerozoic and Hadean regime transitions rather than smoothly through geological time.

The formula is anchored at independent constraints — modern $J2000$ LOD with the LLR recession rate, and the Farhat deep-time curve — with no Hadean constraint imposed and the Phanerozoic paleo-day-count record recovered as validation. Figure 18 shows the resulting LOD trajectory across the full Earth-Moon history. Its self-validation at the Earth-Moon genesis is the centerpiece of subsection 11.4; its empirical confirmation against the historical eclipse record runs on two complementary tracks — a solar-eclipse alignment audit on 26 documented events (21/26 with the framework umbra reaching the observation site within a ±4-hour scan window, subsection 14.10) and a higher-resolution lunar timing test on the 267-event working set from Stephenson et al. (2016) (20.2-min mean |residual|, subsection 14.11).

11.3 H Through Geological Time

Table 30 shows the lattice's headline values across the modern, Devonian, and short-term-future epochs; Figure 19 shows the full $H(t)$ trajectory from genesis to +1 Gyr. Every row scales by the same fractional factor between any two epochs — the lattice is rigid in its proportions and flexible in its scale.

A useful intuition for the rate: one billion years ago, H was about ~79% of its current value. The growth is slow on human and geological timescales — ~0.025% per Myr today — but cumulative over the planet's lifetime.

The forward branches of the genesis-series figures steepen not through new physics but because these are *periods*: $\mathrm{d\,LOD}/\mathrm{d}t \propto \mathrm{LOD}^2$ as the day approaches the tidal-lock

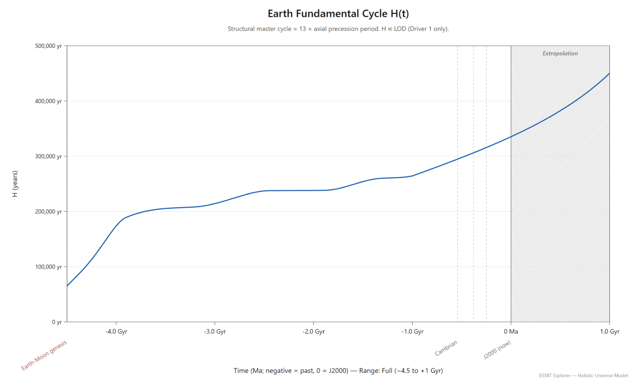

Figure 19: The Earth Fundamental Cycle $H(t)$ across the full Earth-Moon history. Because $H = 13 \times T_{\text{axial}}$ and $T_{\text{axial}} \propto$ LOD under Driver 1, H inherits LOD's regime-aware staircase (Figure 18): rising non-decreasingly from ~64,614 yr at the Earth-Moon genesis (~4.498 Ga) through 335,317 yr at J2000 to ~450,000 yr at +1 Gyr (shaded region: forward extrapolation), with the same intermediate plateaus at the mid-Precambrian slow-recession epochs.

Table 30: Lattice values across geological time. All values from the two-layer proper-physics formula (Equation 31, Equation 32) with no Hadean constraint. Every row scales by the same fractional factor between any two epochs.

Lattice element	Modern (*J*2000)	Devonian (−380 Ma)	+200 Myr future
Earth Fundamental Cycle H	335,317 yr	306,189 yr	352,601 yr
Solar System Resonance Cycle $8H$	2,682,536 yr	~2.450 Myr	~2.821 Myr
Obliquity main beat ($n = 65$)	41,270 yr	~37,685 yr	~43,397 yr
Jupiter perihelion ecliptic ($n = 39$)	68,783 yr	~62,808 yr	~72,328 yr
Earth axial precession ($H/13$)	~25,794 yr	~23,553 yr	~27,123 yr
Moon–Earth distance	384,399.07 km	369,749 km	392,059 km

asymptote, and $H \propto$ LOD propagates the steepening to every H/N. The backward branch is pinned by the paleo record (subsection 11.5); the shaded forward region is polynomial extrapolation, since future tidal dissipation depends on the evolving ocean-basin configuration.

A direct consequence concerns **the classical precession of the equinoxes**, known since Hipparchus and routinely treated as a fixed astronomical constant. Under ESSRT, Earth's axial precession period $T_{\text{axial}} = H/13$ is itself a now-snapshot of a slowly evolving cycle (Figure 20): ~23,553 yr at the Devonian and ~4,970 yr at the Earth-Moon genesis, with a modern-era rate of change of ~6 yr per Myr. The effect is small on human timescales but in principle observable in high-precision IAU precession-rate measurements over decades; distinguishing it from the well-modeled mainstream tidal-LOD evolution and planetary-precession contributions (Capitaine et al., 2003; Vondrák et al., 2011) is the open observational question.

The same rescaling applies to every H/N divisor, including Earth's obliquity cycle $H/8$ (Figure 21): ~8,100 yr at the Earth-Moon genesis, ~41,915 yr at J2000, ~56,300 yr at +1 Gyr. The climate-recorded obliquity beat at $8H/65$ (Law 6, section 6) rescales by the identical fractional factor, one lattice integer away. This period drift is precisely the signal that cyclostratigraphic inversions such as Wu et al. (2024) exploit — shorter precession and obliquity periods measured deeper in the Phanerozoic record — so the paleo validation of subsection 11.5 tests these curves directly. The obliquity *angle* itself keeps oscillating ±0.63607° around its mean at every epoch; what evolves at deep time is the period, not the mean.

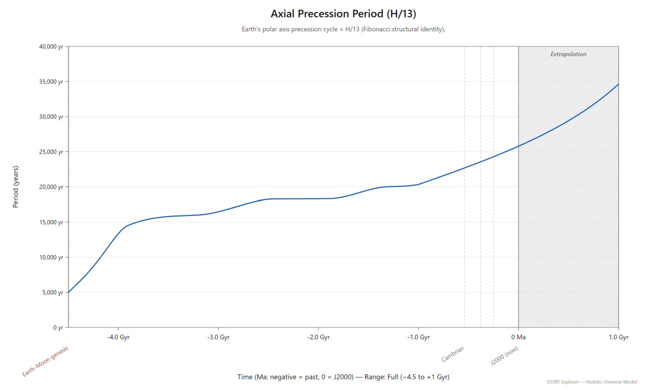

Figure 20: Earth's axial precession period $T_{\text{axial}} = H/13$ across the full Earth-Moon history — the classical precession of the equinoxes as a slowly evolving cycle rather than a fixed constant. The period grows from ~4,970 yr at the Earth-Moon genesis through ~~25,794 yr at J2000 to ~34,600 yr at +1 Gyr (shaded region: forward extrapolation).

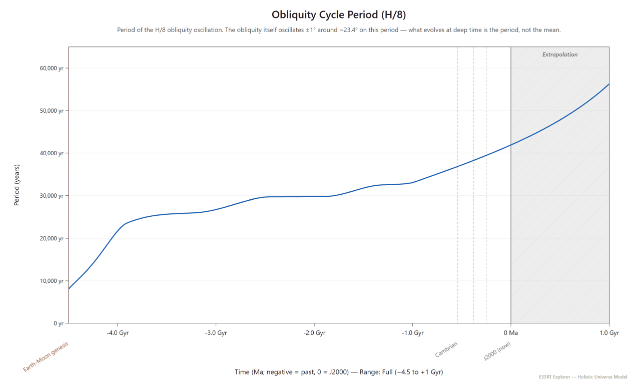

Figure 21: Earth's obliquity cycle period $H/8$ across the full Earth-Moon history: ~8,100 yr at the Earth-Moon genesis, ~41,915 yr at J2000, ~56,300 yr at +1 Gyr (shaded region: forward extrapolation). The obliquity angle oscillates ±0.63607° around its mean on this period at every epoch — what evolves at deep time is the period, not the mean.

11.4 The Earth-Moon Genesis

If H has expanded monotonically from past to present, it must have been smaller in the past — in principle, very much smaller. Running the proper-physics formula backwards, the recession polynomial crosses the **rigid Roche limit** at ~4.498 Ga — the Earth-Moon genesis. At that epoch:

- Moon distance ~9,471 km = 1.48 $R_\oplus$ — the rigid Roche limit, inside which tidal forces shred any solid satellite (the fluid Roche zone at ~2.9 $R_\oplus$ is crossed at ~4.44 Ga).
- Length of day ~4.62 hours — inside the canonical post-giant-impact spin range (~4–6 hr), with no spin constraint imposed: a third independent consistency check alongside the age and the Roche distance.
- $H \approx 64,614$ yr (about 19% of today).
- $8H \approx 0.517$ Myr — the smallest the cycle has ever been.

This is the framework's strongest self-validation (Figure 22). No Hadean constraint was used to calibrate the quartic branch of the history. Its only anchors are modern $J2000$ LOD with the LLR-observed recession rate, and the deep-time tidal-evolution curve of Farhat et al. (2022), with the Phanerozoic paleo-day-count record (Wells, 1963; Wu et al., 2024) recovered as validation; the regime-aware spline preserves the quartic's Roche-crossing epoch as its endpoint, because the mid-Precambrian record leaves the genesis age unconstrained (the fit's genesis profile is flat across 4.42–4.52 Ga). The genesis epoch, ~4.498 Ga, is the **canonical giant-impact Moon-formation age** (~4.5 Ga, dated independently by isotope geochemistry of lunar and terrestrial samples) — itself ~40 Myr after Patterson's Pb-Pb Earth age (Patterson, 1956) of 4.54 Gyr. Two independent measurement chains — tidal physics run backwards on one side, isotope geochemistry on the other — converge on the same answer, and in the right order: Earth first, Moon shortly after, born at the Roche distance where the impact debris could first coalesce. Because Driver 1 uses the modern ~3.82 cm/yr LLR-observed recession rate (Dickey et al., 1994) — the same anchor that classically triggers the well-known linear-extrapolation age paradox (Bills & Ray, 1999), which naïvely projects the Moon at the Roche limit only ~1.5 Gyr ago — the fact that the same rate under the Farhat non-linear polynomial (Equation 31) instead lands the Roche crossing at the giant-impact age is a nontrivial consistency check on the two-layer form, not a curve fit.

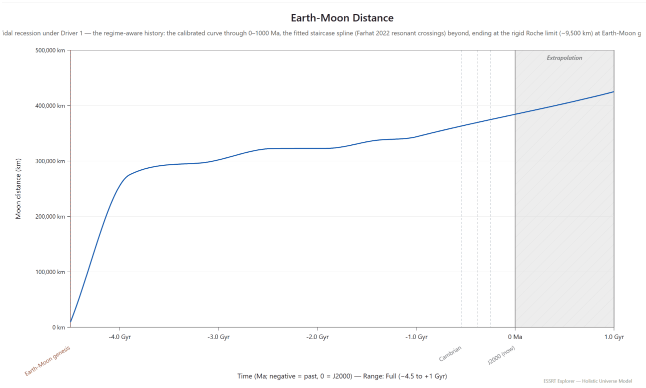

Figure 22: Earth-Moon distance across the full tidal-recession history under Driver 1 (Farhat-form polynomial, LLR-anchored α_1). Run backwards, the curve reaches the rigid Roche limit (~9,500 km) at ~4.498 Ga — the Earth-Moon genesis marker at the left edge — matching the canonical giant-impact Moon-formation age with no Hadean constraint in the fit. Dashed gridlines mark the Cambrian and J2000; the shaded region beyond J2000 is forward extrapolation to +1 Gyr.

The Wells–Patterson coincidence. The same numbers yield a second, independent self-validation. The Wells tidal rate of 0.00526 hr/Ma was calibrated entirely on Phanerozoic fossil data (0–500 Ma; corals, bivalves, rhythmites). Linearly extrapolated, it predicts LOD = 0 at $24/0.00526 = 4.56$ Gyr ago. Patterson's Pb-Pb radiometric Earth age is 4.54 Gyr. The two numbers agree to within 0.5% — the precision of the underlying measurements. This is not coincidence: it is the structural signature of a single, internally consistent picture of Earth-Moon evolution. The $8H$ cycle has a beginning, and the beginning is when the Moon's orbit was just stable enough to exist as a satellite. The linear rate is only a Phanerozoic-local approximation, however — LOD = 0 would imply infinite spin (Earth's rotational breakup limit is ~2 hr); the proper-physics curve replaces the period-zero at Earth's birth with a *distance floor* at the Moon's birth — the rigid Roche limit, with Earth spinning at its finite post-impact rate.

11.5 Paleo Validation

The Phanerozoic record provides a direct test of the predicted $H(t)$ via independent paleontological day-count techniques and, since 2024, via the cyclostratigraphic reconstruction of Wu et al. (2024). Figure 23 shows the underlying days-per-year curve across the full Earth-Moon history; Table 31 compares the formula's predicted days-per-year against directly counted fossil records and Wu's cyclostratigraphy-derived values at twelve epochs spanning the Phanerozoic and Snowball-Earth boundary.

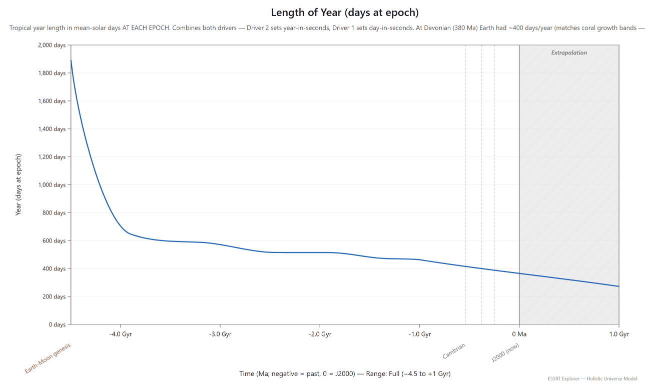

Figure 23: Tropical year length in mean-solar days at each epoch, combining both drivers (Driver 2 sets the year in seconds, Driver 1 the day in seconds): ~1,886 days/yr at the Earth-Moon genesis, ~400 days/yr at the Devonian (matching the Wells (1963) coral growth-band count validated in Table 31), 365.24 today, ~272 days/yr at +1 Gyr (shaded region: forward extrapolation).

Table 31: Paleo-day-count validation across 0–650 Ma. Paleontological anchors (0–380 Ma) match within 1.0% at every point, with the flagship Wells 1963 Devonian count essentially exact (−0.01%); Wu et al. (2024)'s cyclostratigraphic anchors match within −0.51% to +3.63% across the entire 650-Myr range. The 620 Ma Williams discrepancy is discussed in the text.

Age (Ma)	Source	Method	Observed (d/yr)	Framework	Match
0	IERS modern	Atomic clock	365.242	365.242	exact (anchor)
70	de Winter et al. (2020)	*Torreites* rudist bivalve	372	371.53	−0.13% ✓
90	Pannella (1972)	Bivalves (23.5 hr day)	372.6	373.33	+0.20% ✓
100	Wu et al. (2024)	Cyclostratigraphy (TimeOptB Bayesian)	370.65 ± 2.3	374.24	+0.97% ✓
200	Triassic compilation	Various	385.9	383.31	−0.67% ✓
200	Wu et al. (2024)	Cyclostratigraphy	369.87 ± 1.6	383.31	+3.63% ✓
300	Wu et al. (2024)	Cyclostratigraphy	385.31 ± 4.2	392.50	+1.87% ✓
380	**Wells (1963)**	**Devonian corals**	~400	**399.96**	**−0.01**% ✓
400	Wu et al. (2024)	Cyclostratigraphy	403.03 ± 4.6	401.84	−0.30% ✓
500	Wu et al. (2024)	Cyclostratigraphy	413.48 ± 5.8	411.37	−0.51% ✓
620	Williams (2000)	Elatina rhythmites	400.3	423.11	+5.70% ?
650	Wu et al. (2024)	Cyclostratigraphy	418.62 ± 2.0	426.11	+1.79% ✓

The paleontological anchors (0–380 Ma) match within 1.0% at every point, with the flagship Wells 1963 Devonian count essentially exact (−0.01%); across the tabulated datapoints the mean absolute deviation is ~1.0% (paleontological rows alone: ~0.3%). The framework's structural relation reproduces the directly-counted fossil record without any free parameters fit to day-count data.

Wu et al. 2024 — independent 650-Myr cyclostratigraphy reconstruction. The seven Wu et al. (2024) anchors deserve special mention because they constitute an *entirely independent measurement chain*. Wu et al. (2024) apply a TimeOptB Bayesian inversion to cyclostratigraphic records (Milankovitch-driven sedimentary cycles) across 650 Myr of the Phanerozoic. Unlike paleontology (Wells 1963 coral growth bands, Pannella 1972 bivalves, Williams 2000 tidal rhythmites), Wu's method does not depend on biological growth-band counting — it derives LOD, Earth-Moon distance, and axial precession rate directly from spectral analysis of climate proxies, with full $\pm 2\sigma$ uncertainty propagation at 100-Myr intervals. The framework matches Wu's anchor reconstruction within −0.51% to +3.63% across the entire 650-Myr range, with a mean absolute residual of ∼1.5% across the tabulated Wu anchors. This constitutes independent validation across an entirely separate measurement technique — paleontology and cyclostratigraphy converging on the same $H(t)$ evolution. The match at 400 Ma is particularly noteworthy: Wu's cyclostratigraphy-derived 403.03 days/year sits within 0.7% of Wells (1963)'s paleontological count of ∼400 days/year, and the framework reproduces both within 0.5%.

The 620 Ma Williams discrepancy is documented honestly: Farhat's globally-smoothed ocean-tidal-Q curve dips shallower than Williams's direct rhythmite count, possibly because the Ediacaran-Cryogenian Snowball Earth interval (∼720–635 Ma) had unusual ocean-tidal dissipation that the smooth fit averages over. The thermal-tide-lock framework of Mitchell & Kirscher (2023) places the transition out of the Proterozoic tidal-resonance regime at this same interval. Notably, Wu's adjacent 650 Ma cyclostratigraphic anchor (418.62 d/yr) matches the framework to within 1.8% while Williams's 620 Ma value misses by 5.7%, suggesting Williams's specific rhythmite-derived value is the outlier rather than the proper-physics formula. For Phanerozoic work ($\leq$ 500 Ma) the proper-physics formula is uniformly better than a linear LOD approximation; for Snowball-boundary epochs the discrepancy is documented rather than papered over.

11.6 The mid-Precambrian record (1–3.5 Ga)

Beyond the cyclostratigraphic era of Table 31, the regime-aware branch of the recession history (the spline of Equation 31's discussion, with the open $L_{\mathrm{EM}}(t)$ budget of Equation 32) is tested against the published mid-Precambrian record — cyclostratigraphy, tidal rhythmites and tidal bundles spanning 1.1–3.2 Ga (Table 32). Every anchor is reproduced within its published uncertainty. The interval is scientifically live: Mitchell & Kirscher (2023) read the era's slow day-length growth as a thermal-tide resonance stall, while Zhou et al. (2024) argue the Lamb resonance is unlikely in the Mesoproterozoic and attribute the same shape to weak ocean dissipation; the framework's fitted pump strength lets the record itself arbitrate, and Zhou et al. (2024)'s paired distance+LOD epochs double as a direct test of the angular-momentum budget (their reconstructed L_{EM} is flat to ∼0.2% across 1.6–1.2 Ga, which the fitted budget reproduces).

Table 32: Mid-Precambrian validation: the regime-aware recession history against the published record, 1.1–3.2 Ga. LOD in hours; Earth-Moon distance in Earth radii. Every anchor is reproduced within its published uncertainty.

Age (Ma)	Source	Quantity	Observed	Framework	Match
1100	Bao et al. (2023) (Nanfen)	LOD	18.94 ± 0.39	18.74	−1.05% ✓
1215	Zhou et al. (2024) (Yemahe)	LOD	18.86 ± 0.17	18.66	−1.05% ✓
1215	Zhou et al. (2024) (Yemahe)	distance	53.52 ± 0.27	53.23	−0.55% ✓
1400	Meyers & Malinverno (2018) (Xiamaling)	LOD	18.68 ± 0.25	18.48	−1.06% ✓
1480	Zhou et al. (2024) (Wumishan)	LOD	18.12 ± 0.19	18.26	+0.75% ✓
1634	Zhou et al. (2024) (Chuanlinggou)	LOD	17.82 ± 0.15	17.68	−0.80% ✓
2450	Weeli Wolli rhythmites	LOD	17.95 ± 1.32	17.01	−5.24% ✓
2460	Lantink et al. (2022) (Joffre BIF)	LOD	16.98 ± 0.50	17.01	+0.16% ✓
3200	Moodies Group tidal bundles	distance	46.45 ± 1.50	46.44	−0.03% ✓

11.7 When Will the $8H$ Cycle End

If the cycle had a beginning at the Roche limit, it must have an end at the opposite extreme. The Earth-Moon system asymptotically approaches the **tidal-lock asymptote**: Earth's spin period equals the Moon's orbital period, both at approximately 47 days in current units. From angular-momentum conservation:

- Tidal-lock Moon distance: $a_{\mathrm{lock}} = 555,623$ km $= 87.1\, R_{\oplus}$ (currently $60.3\, R_{\oplus}$).
- Approach timescale: ∼50 Gyr (well beyond the Sun's red-giant phase at +5 Gyr).
- Days per year at tidal lock: ∼7.8 (vs. current 365.24).

The proper-physics formula remains valid for projections up to about +3 Gyr forward; beyond that the polynomial saturates at the tidal-lock distance and the formula returns no value. For longer projections, the angular-momentum boundary itself takes over.

The framework's effective predictive domain spans about 7.5 Gyr — from Earth-Moon genesis to the formula's +3 Gyr horizon at the tidal-lock distance. **The modern epoch sits at about** 61% through this domain. Beyond +3 Gyr the proper-physics formula returns no value, though the Earth-Moon system continues to exist (and the Sun continues to shine) until the red-giant phase at +5 Gyr.

Future-projection uncertainty. The Farhat polynomial (Equation 31) is calibrated against past anchors and extrapolated forward beyond $J2000$. For sub-200 Myr forward projections the framework sits well within accepted tidal-modelling ranges. At +1 Gyr the projected H of ∼450,257 yr corresponds to ∼32-hour LOD and ∼425,000 km Moon distance; these values sit ∼10% above the predictions of independent tidal models (Touma & Wisdom, 1994; Néron de Surgy & Laskar, 1997), which predict slower late-future recession as tidal force weakens ($\propto 1/r^6$) with Moon distance. The polynomial's smooth-extrapolation behaviour does not capture this physical slowdown. For internal lattice ratios the difference is irrelevant (every period scales together by the same factor); for absolute long-term forward use the +500 Myr to +1 Gyr range should be read as an upper-bound estimate rather than a precise prediction.

11.8 Deep-Time Invariants: The Day-Count Near-Invariant

The identity

$$H \times \text{days/yr} \approx \text{TOTAL\_DAYS\_IN\_H} = 122,471,920 \text{ days} \tag{33}$$

is the framework's **structural near-invariant**. The value 122,471,920 is the $J2000$ anchor — exact today by construction — and drifts smoothly with geological time (−74 ppm at the Devonian, −999 ppm at the Earth-Moon genesis). The physical interpretation is that **Earth rotates approximately**

the same number of times — about 122 million rotations — during each H cycle, across the planet's entire history.

The near-invariance arises from a near-cancellation between the two drivers. Driver 1 makes H longer in years while shortening days-per-year (LOD grows). Driver 2 shortens the tropical year in seconds (the Sun was more massive in the past). The two scalings almost cancel, leaving the rotation count per H cycle near-invariant but not exactly constant. Driver 1 is ~100× larger in fractional terms than Driver 2, so for most paleoclimate purposes Driver 1 dominates the lattice expansion and Driver 2 contributes a small Gyr-scale correction to the structural near-invariant.

The exact form. The Driver-2 drift is fully determined, and correcting for it closes the relation exactly. The starting point is the **dual-divisor identity**: the one canonical day count serves both year frames at every epoch, solar-year days = TOTALDAYS$/H$ and sidereal-year days = TOTALDAYS$/(H-13)$, the 13 being the axial-precession cycles per H. Since $H \propto$ LOD (the structural identity) and Kepler under the adiabatic mass-loss coupling ($a \propto 1/M$, $T \propto M^{-2}$, hence $T \propto \mathrm{AU}^2$) ties the sidereal year length to the Earth-Sun distance, the composition

$$H(t)\cdot\frac{T_{\rm sid}(t)}{\mathrm{LOD}(t)}\cdot\left(\frac{\mathrm{AU}_0}{\mathrm{AU}(t)}\right)^2 = \mathrm{TOTAL\_DAYS\_IN\_H}\cdot\frac{H_0}{H_0-13} \quad (34)$$

holds exactly — at floating-point precision — at every epoch of the framework's 4.5-Gyr domain, the constant being the canonical 122,471,920 carried through the dual-divisor bridge at $J2000$ rather than an independent number. (The tropical-days form $H \times$ days/yr $\times (\mathrm{AU}_0/\mathrm{AU})^2$ retains a ~−118 ppm residual at genesis — the structural $13/H(t)$ term itself — and the bridge factor $[H/(H-13)]\cdot[(H_0-13)/H_0]$ restores exactness with the canonical constant.) For independent reproduction via an explicit Kepler evaluation, two consistency conditions apply: the gravitational parameter is the two-body $G(M_\odot + M_\oplus)$, scaled as a whole by $\mu(t) = \mu_{J2000}/(1-\Delta m)$ with Δm defined against the Sun-only $J2000$ mass — scaling the solar share alone while holding Earth's fixed breaks the identity at the $\Delta m \cdot M_\oplus/(M_\odot + M_\oplus) \approx 0.6$ ppb level at genesis. Then $T = 2\pi\sqrt{a^3/\mu} = T_0(1-\Delta m)^2$ reproduces the framework's product forms $\mathrm{AU} = \mathrm{AU}_0(1-\Delta m)$ and $T_{\rm sid} = T_{\rm sid,0}(1-\Delta m)^2$ exactly, and $T^2\mu/a^3$ is constant at every epoch. Classified honestly: the AU^2 factor is textbook celestial mechanics, the $H \propto$ LOD factor is the framework's structural postulate, and Equation 34 is a theorem of the two rather than an independent law. Its significance is that standard dynamics predicts no such constancy (it defines no H, and the *physical* axial precession is not proportional to LOD — the lunar $1/a^3$ torque term breaks that proportionality, as the Wu et al. (2024) comparison of subsection 11.5 makes explicit). The invariant is therefore the framework's most compact falsifiable statement: a paleontological day-count and a cyclostratigraphic lattice period measured at the same epoch must satisfy this single equation. The Devonian already exercises the cross-check — Wells's ~400 days/yr and the observed ~37 kyr obliquity beat (Boulila et al., 2018) are the two sides of Equation 34 at 380 Ma.

11.9 The Lunar Precession Invariant

A second deep-time invariant falls out of the same framework, this time governing the Moon's apsidal and nodal precession. Where the day-count near-invariant of subsection 11.8 ties Earth's rotation count to one H cycle (with small Driver 2 drift), the Lunar Precession Invariant ties the Moon's perigee and node advance to the same lattice and is held *exact* at every epoch:

$$T_{\rm apsidal} \times H = \text{const}, \qquad T_{\rm nodal} \times H = \text{const} \quad (35)$$

both in year-units, equinox-of-date frame (the Meeus/IERS observable); the star-referenced products are equally preserved, since general precession itself scales as $1/(H/13)$. Equivalently, the count of lunar apsidal/nodal cycles per H scales as $(H(t)/H_0)^2$: as the Moon recedes and H grows under Driver 1, the Moon's precession periods grow in lockstep, so their *product* with H stays fixed.

The invariant's value is set by the $J2000$ anchors: $H_0 = 335{,}317$ yr (framework structural), and the observed lunar precession periods give the integer cycle counts $N_{\rm apsidal} = 37{,}899.5$ and $N_{\rm nodal} = 18{,}014.875$ per H at $J2000$, from which

$$T_{\rm apsidal} \times H = H_0^2/N_{\rm apsidal} \approx 2{,}966{,}728 \text{ yr}^2 \quad (36)$$

and analogously $T_{\rm nodal} \times H \approx 6{,}241{,}369$ yr^2. These numerical values are *empirically anchored* (one structural H_0, one observed period); what is structural is the constancy claim, not the value itself.

Table 33: Lunar Precession Invariant across geological time. The product $T_{\rm apsidal} \times H$ shown in the last column is the J2000-anchored value $H_0^2/N_{\rm apsidal,J2000} = 2{,}966{,}728$ yr^2, held exact at every epoch by the framework's $(H/H_0)^2$ scaling. $T_{\rm apsidal}$ is displayed to 3 decimals for legibility; manual multiplication of rounded H and $T_{\rm apsidal}$ reproduces the constant to within ~0.01%.

Age (Ma)	H (yr)	$T_{\rm apsidal}$ (yr)	$T_{\rm apsidal} \times H$ (yr^2)
+200 (future)	352,601	8.414	2,966,728
0 ($J2000$)	335,317	**8.848**	**2,966,728**
−100	327,253	9.066	2,966,728
−380 (Devonian)	306,189	9.689	2,966,728
−1000	264,346	11.223	2,966,728
−2500	173,033	17.146	2,966,728

The H^2 scaling form matches the leading m^2 order of Brown's lunar perturbation theory (Brown, 1896; Brouwer & Clemence, 1961), where $m = n_{\rm Sun}/n_{\rm Moon} \approx 1/13.37$ is the ratio of solar to lunar mean motion. The $J2000$ magnitude ($T_{\rm apsidal} \approx 8.85$ yr) is anchored from observation rather than predicted: Brown's leading m^2 alone gives ~17.8 yr — roughly double the observed rate. This is the historical **Newton-Clairaut problem**: Newton's leading m^2 calculation in the *Principia* (1687) gave half the observed perigee rate, and Clairaut showed in 1749 that the m^3 and higher terms approximately double it to recover the observed value. The framework adopts the H^2 scaling form to propagate to deep time, with no polynomial corrections. While the $J2000$ magnitude is observation-anchored, the secular *time-derivative* structure of the observed rates is derived: the solar-eccentricity channel reproduces the empirical T^2/T^3 coefficients of the lunar fundamental arguments (see the framework-native fundamental arguments in subsection 14.10).

The Lunar Precession Invariant does not replace Brown's lunar theory but sharpens it: the m^2-leading-order scaling is adopted as a structural law, with the $J2000$ magnitude anchored from observation and propagated to deep time without polynomial corrections. Where Brown's expansion derives the absolute period from the underlying m-series, ESSRT treats the period as one anchored input and the $(H/H_0)^2$ evolution as the structural claim — the two views agree on the scaling form by construction.

A stricter invariant than the day-count. Unlike $H \times$ days/yr (Equation 33), which drifts ~ -999 ppm at the Earth-Moon genesis because tropical year-seconds shorten under Driver 2 (solar mass loss), the Lunar Precession Invariant in its year-frame form does *not* involve seconds — Driver 2's effect on year-seconds is therefore absent. The invariant is preserved by Driver 1 alone, exact at every epoch the framework spans. The equivalent star-referenced perigee precession period (in seconds) used by the model's lunar engine via the Brouwer-Clemence form $T_{\text{per}} \propto T_{\text{yr}}^2/T_{\text{sm}}$ (Brouwer & Clemence, 1961) picks up the small Driver 2 drift, but agrees with the year-frame invariant to <100 ppm across the Phanerozoic.

11.10 Integer Invariance Across Epochs

The L1 lattice has two components: integer labels and absolute periods. The integer labels — $n = 65$ for the obliquity main beat, $n = 39$ for Jupiter's ecliptic perihelion, $n = 16$ for the perihelion harmonic, and the full 32-element set used in the climate fit of section 10 — are **structural constants of the solar system's secular dynamics**. Across geological time, only the absolute periods rescale via $8H(t)/n$; the integers themselves stay invariant.

This claim is itself testable. Cyclostratigraphic L1 lattice fits to paleoclimate spectra at Devonian, Permian, and Cretaceous epochs should find the same set of integers identified in the post-MPT LR04 fit — only with rescaled absolute periods. A deep-time spectrum that fits a substantively different integer set falsifies the invariance claim. The Phanerozoic-paleo predictions made by ESSRT and the empirical lattice fits of section 10 are consistent with integer invariance to within 1% across the canonical Milankovitch beats over the Cenozoic backward extension.

11.11 Solar System Rescales Uniformly

Driver 2's effect on every planet's orbit is governed by the adiabatic invariant $a \times M_\odot \approx$ constant. As $M_\odot$ decreases at rate 9.3×10^{-14} per year, every a_i increases at the same fractional rate. Going backward in time the entire solar system contracts uniformly: at the Devonian the solar system was ~35 ppm tighter than today, with Mercury at 57,907,130 km (versus 57,909,176 today), Jupiter at 778,519,688 km (versus 778,547,200), and Neptune at 4,503,284,523 km (versus 4,503,443,661) — every distance moved by the same proportional amount. At the Hadean the entire solar system was ~422 ppm tighter.

The structural consequence: **planet orbit ratios are conserved exactly across all epochs**, and the secular g/s frequencies rescale uniformly $\propto M_\odot$. Driver 2 affects the spatial scale uniformly without disturbing ratio structure — which is why the Earth-family integer invariance (subsection 11.10) coexists cleanly with the simultaneous secular evolution of $H(t)$: the two tiers scale on independent clocks.

11.12 The Expanding-Universe Parallel

The name *Expanding Solar System Resonance Theory* deliberately echoes Hubble's *Expanding Universe Theory*. The structural parallels are striking and worth tabulating explicitly (Table 34).

Table 34: Structural parallels between Hubble's Expanding Universe Theory and the framework's Expanding Solar System Resonance Theory. The parallel is rhetorical, not physical equivalence; what is shared is the *shape of the claim* (a monotonically growing scale parameter governing a richly structured system).

Property	Expanding Universe	Expanding Resonance
What expands	Distances between galaxies	Periods within the solar-system lattice (H, $8H$, every H/N)
Direction of change	Monotonic — distances grow	Monotonic — periods grow
Driving mechanism	Metric expansion of space (Λ / dark energy)	Earth-Moon tidal evolution + solar mass loss
Beginning	Big Bang (~13.8 Gyr ago)	Earth-Moon genesis (~4.498 Gyr ago — giant-impact epoch, Moon at the rigid Roche limit)
Asymptotic future	Heat death (de Sitter expansion)	Earth-Moon tidal lock (Moon at ~555, 623 km, ~50 Gyr ahead)
Defining constant	Hubble parameter $H_0 \approx 70$ km/s/Mpc	Earth Fundamental Cycle H and growth rate $\mathrm{d}H/\mathrm{d}t \approx 0.025\%$ per Myr
Structure preserved	Statistical homogeneity & isotropy at large scales	Integer-label lattice (subsection 11.10)
What does not change	Underlying laws of physics; dimensionless ratios	Integer labels; planet orbit counts per $8H$

The parallel is rhetorical, not physical equivalence. Cosmic expansion is universal and dominates the largest scales; expanding resonance is bounded to the solar system and acts on geological-to-astronomical timescales. Cosmic expansion is driven by a fundamental property of spacetime; expanding resonance is driven by standard Newtonian mechanics plus solar-evolution input. What the parallel makes vivid is the *shape* of the claim — a monotonically growing scale parameter governing a richly structured system — not the underlying physics.

12. Mercury's Perihelion: A Reference Frame Consequence

12.1 Standard Framework and Alternative Interpretation

Mercury's perihelion precesses at $575.31 \pm 0.0015''/\text{cy}$ (ICRF) (Park et al., 2017). Newtonian perturbations account for ~$532''/\text{cy}$; the remaining ~$43''$ has been attributed to General Relativity since 1915. In the model Mercury's perihelion advances in ecliptic longitude at the lattice rate $531.44''/\text{cy}$ ($8H/11$). Expressed in right ascension — the coordinate measured from Earth — a direction advancing uniformly in ecliptic longitude λ advances at the rate

$$\frac{d\alpha}{d\lambda} = \frac{\cos\varepsilon}{\cos^2\lambda + \sin^2\lambda\cos^2\varepsilon}, \tag{37}$$

which at Mercury's J2000 perihelion longitude (77.457°) and the IAU 2006 obliquity equals 1.08036. The projected rate is $574.14''/\text{cy}$, an excess of $42.71''/\text{cy}$ over the ecliptic advance, against the general-relativistic advance $6\pi GM/(c^2a(1-e^2))$ per orbit evaluated from the same constants, $42.98''/\text{cy}$. The identity involves three inputs (the divisor, the IAU perihelion longitude, the IAU 2006 obliquity) and no fitted quantity. The agreement is at the 0.6 % level and is not exact: ranging determinations pin the inertial excess at $42.980 \pm 0.002''/\text{cy}$ (Pireaux et al., 2003), and the EPM2008 residual to the relativistic rate is $-0.004 \pm 0.005''/\text{cy}$ (Pitjeva & Pitjev, 2013), so the projected value falls $0.27''/\text{cy}$ short of the measured excess, many times its uncertainty.

The Earth-frame rate the simulation measures for Mercury, 579.83″/cy, is this projection plus the term the secular obliquity decrease ($\dot{\varepsilon} = -46.8''$/cy) adds to any right ascension, $\partial\alpha/\partial\varepsilon \cdot \dot{\varepsilon} = 4.31''$/cy; a closure gate pins this decomposition for all seven planets at 1900, 2000 and 2100 to better than 1″/cy.

The statement is made for every planet, and Table 35 is its own test: the projection excess reproduces the relativistic advance for Mercury and for no other planet.

Table 35: The equatorial projection of each planet's ecliptic perihelion advance (Equation 37, J2000 perihelion longitudes, IAU 2006 obliquity) against the general-relativistic advance derived from the same constants

Planet	Ecliptic advance (″/cy)	$d\alpha/d\lambda$	Projection excess (″/cy)	GR advance (″/cy)
Mercury	531.44	1.08036	42.71	42.98
Venus	−289.87	1.00661	−1.92	8.62
Mars	1,739.25	0.94201	−100.85	1.35
Jupiter	1,884.19	0.92693	−137.67	0.06
Saturn	−3,140.31	1.08966	−281.55	0.01
Uranus	1,159.50	0.92126	−91.29	0.00
Neptune	193.25	0.99870	−0.25	0.00

The projection excess is not constant: it drifts with λ and ε by about +0.3″/cy per millennium, whereas the relativistic advance is fixed. Modern determinations of the advance are ranging fits to an inertial dynamical model with General Relativity inside it (Park et al., 2017), a chain in which no equatorial angle is formed; the classical values (Clemence, 1947) rest mainly on transit timings. The model therefore states the identity and its all-planet test, and leaves as open the mechanism by which an equatorial projection would enter those determinations.

In the geocentric frame, the full Clemence (1947) breakdown (as reviewed by Berche & Medina 2024) shows Venus contributing ~278″/cy (52%), Jupiter ~154″/cy (29%), Earth ~90″/cy (17%), Saturn ~7″/cy, and Mars + others ~3″/cy, giving a Newtonian subtotal of 5,557.18 ± 0.85″/cy against an observed 5,599.74 ± 0.41″/cy — leaving a residual of 42.56 ± 0.94″/cy. The uncertainty on this residual (~1″/cy) is rarely emphasized.

The model does not claim GR is incorrect — GR has been confirmed independently across many other tests. For Mercury's perihelion specifically, the model states a coordinate identity (Table 35) whose slow secular drift differs from the constancy of the relativistic advance. Pitjeva & Pitjev (2013) show that solar system observations constrain but do not uniquely determine the relativistic contribution. The model implements Laplace–Lagrange secular theory, reproducing the standard Newtonian breakdown with ~96% accuracy. A notable failure occurs for Venus: secular theory predicts 1,075″/cy versus the observed 204″/cy. This is a known limitation of first-order secular theory for low-eccentricity orbits — Venus's nearly circular orbit ($e = 0.007$) makes its perihelion direction extremely sensitive to perturbations. This connects to the finding (section 13) that low-eccentricity planets' precession fluctuations are dominated by Earth's rate variations rather than geometric modulation — both observations reflect the same physics: perihelion is poorly defined for nearly circular orbits.

12.2 Independent N-Body Convergence

Two independent determinations of the geocentric total agree at epoch J2000 while attributing the surplus over the Newtonian planetary perturbations to different causes:

Table 36: Mercury geocentric precession: two independent sources

Source	Method	Total (″/cy)
Smulsky (2011)	Galactica N-body (compound solar rotation)	5,601.9
Berche & Medina (2024)	Analytical (Clemence, 1947) (General Relativity)	5,599.7

The model's contribution is the identity of Table 35, not a third total.

12.3 The Beat-Frequency Structure

The model predicts Mercury's Earth-frame precession rate oscillates with a dominant period of ~7,451 years (1/45 of the Earth Fundamental Cycle; J2000-anchor period — the integer-divisor structure $H/45$ is invariant at any epoch under section 11, the literal period rescales with $H(t)$). The fluctuation ranges from −47″ to +48″/cy around the ~531.4″ baseline. This Earth-frame rate is a right ascension in the simulation's equatorial frame — the lattice rate projected with $d\alpha/d\lambda$ (Equation 37) plus the obliquity-rate term — and no observer publishes it; in ecliptic longitude, the coordinate of every published determination, Mercury's rate is the constant lattice value ~531.4″/cy, and the fluctuation averages to zero over the full Earth Fundamental Cycle.

12.4 The BepiColombo Test

MESSENGER measured 575.31 ± 0.0015″/cy at epoch ~2013. BepiColombo (orbit insertion November 2026, science operations from April 2027) provides the second high-precision epoch. Both are ranging determinations fitted with an inertial dynamical model that contains General Relativity (subsection 12.5); no equatorial angle is formed in that chain, so an equatorial projection cannot appear in it, and the projection statement of Table 35, like General Relativity, predicts that BepiColombo returns ~575.31″/cy. BepiColombo is therefore not a discriminating test of the projection statement. What it does provide is a bound on the secular change of the advance between the two epochs: the projection excess drifts by about +0.3″/cy per millennium, a few hundredths of an arcsecond per century over the ~14-year baseline, below both missions' stated uncertainties. The Sun's gravitational quadrupole moment (J_2), which varies with solar activity (Mecheri & Abdelatif, 2022), remains an additional systematic uncertainty that BepiColombo will help resolve.

12.5 The Measurement Chain: An Open Question

Two coordinates carry a perihelion rate and every published determination is in the first: (a) ecliptic longitude — relative to the stars (ICRF, 575.31″/cy from ranging) or relative to the equinox of date (the classical 5,599.74″/cy of Clemence (1947), from 1765–1937 longitudes; adding the IAU 2006 precession to the ICRF value gives 5,604.11″/cy by definition, not by measurement); (b) right ascension in an equatorial frame — the quantity the simulation's Earth-frame export produces, which no observer has published. The Newtonian contribution (531.54″ with Clemence's masses, 532.33″ in the modern chain) is subtracted in coordinate (a), and the ~43″ residual is attributed to GR. The measurement chain also depends critically on Earth's position in ICRF, calculated from Earth orientation models that account for precession, nutation, and polar motion. If Earth's long-period precession motions (~25,794 and ~111,772 year cycles) have any systematic modeling errors, these would propagate into Mercury's calculated position. The model's own Earth-frame rate for Mercury (579.83″/cy) is entirely such a coordinate effect — the projection of Equation 37 plus the obliquity-rate term — and contains no oscillating residual of that kind at the present epoch.

A further methodological caveat applies to modern measurements specifically: the reported 575.31″/cy comes from fitting a GR-inclusive ephemeris to spacecraft ranging data (Park et al. 2017 fit Mercury's orbit jointly with all planets, 343 asteroids, and the PPN parameter β, finding $\beta \approx 1$). This is conceptually equivalent to measuring the Newtonian baseline (~532″/cy) and adding the assumed GR contribution (~43″/cy). For the projection statement of Table 35 the open question is therefore the mechanism: the classical values rest mainly on transit timings (heliocentric ecliptic geometry) and the modern values on ranging fits, and in neither chain is an equatorial angle formed on which the slope of Equation 37 could act. The model states the identity and its all-planet test and does not claim the mechanism; a determination of the anomaly's secular change at the few-hundredths-of-an-arcsecond level, or a demonstrated equatorial step in a reduction chain, would decide it.

Part III: Predictions and Validation

13. Unified Predictive Formulas

A unified ~2,400-term formula system (planet-specific term counts 2,393–2,435) predicts the precession fluctuation of all seven planets (excluding Earth, the observer) using only time as input — no observation of each planet's perihelion is required. The system uses Earth's formulas (perihelion longitude, obliquity, eccentricity, Earth Rate Deviation) to predict how each planet's *apparent* precession changes due to Earth's reference frame motion.

Table 37: Unified predictive formula performance

Planet	R^2	RMSE (″/cy)	Base (″/cy)	Period (yr)
Mercury	0.999992	0.0974	531.4	243,867(H×8/11)
Venus	0.999975	0.0972	-289.9	−447,089(−8H/6)
Mars	0.999999	0.0972	1,739.2	74,515(8H/36)
Jupiter	0.999999	0.0964	1,884.2	68,783(8H/39)
Saturn	1.000000	0.0967	-3,140.3	41,270(8H/65, retr.)
Uranus	0.999998	0.0965	1,159.5	~111,772(H/3)
Neptune	0.999951	0.0959	193.2	670,634(H×2)

13.1 Eccentricity-Dependent Driver Mechanisms

The analysis reveals that different planets show fundamentally different fluctuation drivers:

- **Mercury** (e = 0.206): Well-defined perihelion. Fluctuation range −47 to +48″/cy, dominated by geometric modulation — angular interference of Earth's and Mercury's perihelion precessions.
- **Venus** (e = 0.007): Poorly defined perihelion. Fluctuation range −29 to +41″/cy — ~7× larger than Mercury's despite Venus being more circular — dominated by quadratic Earth Rate Deviation effects.
- **Mars through Neptune**: Smaller fluctuation ranges (−31 to +19″/cy for Neptune up to −310 to +303″/cy for Saturn), dominated by linear rate-cycle interactions.

This eccentricity dependence is a natural consequence of the reference frame interpretation: a planet whose perihelion is well-defined (eccentricity not too small) shows geometric modulation projecting onto a clear direction; a planet whose perihelion is essentially arbitrary ($e \to 0$) primarily reflects Earth's own rate variations, not its own geometry.

13.2 Saturn as the Obliquity Driver

Saturn is the only planet requiring time-varying obliquity and eccentricity parameters for accurate predictions. Its perihelion period (41,270 years at J2000; the 8H/65 window-epoch descriptor, Fibonacci anchor H/8) coincides at J2000 with the period at which Earth's obliquity is driven (the climate $k + s_3$ beat — an Earth-family quantity whose label is epoch-invariant; Law 6 in subsection 6.1). Without time-varying coupling terms, Saturn's formula cannot achieve R^2 = 1.0, suggesting Saturn's precession directly modulates Earth's axial tilt oscillation.

14. Calibration, Validation, and Transparency

14.1 Free Parameters

The model has 6 adjustable parameters — 5 for the Earth simulation and 1 discrete configuration choice for the planetary Fibonacci structure:

Table 38: Free parameters

Parameter	Value	How determined
Earth Fundamental Cycle	335,317 yr	Fitted to 1246.03125 AD alignment + J2000 longitude
Fibonacci divisors	3, 8, 13	Structural assumption
Mean obliquity	23.41353°	Fitted to observed obliquity range
Amplitude	0.63607°	Fitted to observed obliquity range
Anchor year	−302, 635	Derived from Earth Fundamental Cycle and 1246.03125 AD
Planet configuration	Config #4	Exhaustive search; unique mirror-symmetric solution

The planet configuration assigns three quantities to each planet: an oscillation period (from Law 1's Fibonacci hierarchy), a quantum number d (determining amplitude via Law 2), and a balance group (in-phase or anti-phase). The periods and balance groups are observationally constrained; only the d-assignment is a free choice, making this a single discrete parameter.

Table 39: Genuine predictions (not used in calibration)

Prediction	Model	Reference value	Agreement
Obliquity at 9,233 BC	24.5117°	24.1956° (La2004)	±0.32°
Obliquity at 11,725 AD	22.5435°	22.6117° (La2004)	±0.07°
Perihelion long. 1000 AD	85.767°	85.788° (Meeus)	±0.025°
Eccentricity (J2000)	0.01671	0.01671022 (NASA)	±0.00001
Incl. to inv. plane	1.57869°	1.57869° (S&S 2012)	±0.0001°

14.2 Assumptions vs Measurements

It is useful to draw an explicit line between what the model *takes as given* (assumptions and free parameters) and what *falls out* of the fit (measurements). Together they cover every numerical claim in this paper.

Table 40: Explicit partition: what the model takes as given vs. what falls out of the fit. The right column contains every numerical result tabulated in the rest of the paper not in the left column.

Assumptions (given)	**Measurements (fall out of the fit)**
J2000 orbital elements (a, m, e, i, Ω, ω) from JPL/DE440	Year lengths (tropical, sidereal, anomalistic, four cardinal-point)
Newtonian gravity	Day lengths (solar, sidereal, stellar)
Earth's obliquity decomposes as axial tilt + inclination tilt	Axial precession rate (from the year-length identity)
Balanced Year exists — the two tilt effects cancel at one epoch	Each planet's ecliptic and ICRF perihelion advance at any epoch
Fibonacci divisor structure (3, 8, 13 for H subdivision)	Mercury's projected excess at J2000 (42.71"/cy vs GR 42.98"/cy)
Planet configuration #4 (unique mirror-symmetric solution)	Per-planet ψ inclination amplitudes (Law 2)
6 free parameters fitted to J2000 (table above)	Per-planet K eccentricity amplitudes (Law 4)
	Saturn's eccentricity predicted from the other 7 planets (~0.27% error)
	Climate Formula L1 lattice amplitudes (the 33-integer ridge fit)
	Ascending node positions (< 0.0001° vs. Souami & Souchay 2012)
	All long-period cycles (eccentricity, obliquity, inclination, ascending node) for every planet

14.3 The Holistic Lock: No Isolated Knobs

A central methodological feature of the model is that it has no separate slider for any single observable. There is no parameter labelled "Mercury anomaly," "Saturn perihelion rate," "axial precession," or "100-kyr cycle amplitude." Each of those quantities — and every value in the right column of Table 40 — emerges from the same 6-parameter fit.

Concretely: changing any one of the six free parameters (or any J2000 input element from JPL/DE440) by a small amount propagates through every downstream observable. Year lengths shift, day lengths shift, ascending nodes shift, eclipse timings shift, the Mercury residual at J2000 shifts, the Climate Formula's L1 amplitudes shift. Reciprocally, no observable can be made to agree with reality at the expense of another — the fit is end-to-end locked.

This property has two consequences:

- **Predictive power**: once H, the obliquity amplitude, and the discrete configuration are set, every numerical prediction in this paper (axial precession rate, perihelion advances of all eight planets at any epoch, the 33-integer L1 lattice positions, Mercury's residual, Saturn's ecliptic-retrograde rate) is determined without further tuning. Predictions that disagree with observations cannot be patched in isolation.
- **Falsifiability**: the model commits to a single integer-divisor structure on $8H$. A genuine measurement that contradicts any one observable propagates the same way — it would force the fit elsewhere out of agreement. At the level demonstrated for the existing data this propagation is the structural sense in which the six Laws are falsifiable rather than merely descriptive (section 15).

14.4 Ascending Node Calibration

The inclination oscillation formula requires accurate ascending node positions on the invariable plane. Souami & Souchay (2012) published these for all planets, but their values are calibrated to epoch-specific inclinations, while the model uses mean (time-averaged) inclinations. When Earth's mean inclination (1.48113°) is used instead of the J2000 value (1.579°), the original S&S ascending nodes produce ecliptic inclinations that deviate from observed JPL values. Using spherical trigonometry:

$$\cos(i_{\mathrm{ecl}}) = \cos(i_p)\cos(i_e) + \sin(i_p)\sin(i_e)\cos(\Delta\Omega) \qquad (38)$$

where i_p and i_e are the planet's and Earth's inclinations to the invariable plane, and $\Delta\Omega$ is the ascending node difference. Since i_{ecl} is known from JPL observations, the ascending node becomes the only unknown — geometrically determined by the linkage between two independent datasets (JPL ecliptic inclinations from spacecraft tracking + S&S invariable-plane inclinations from angular momentum), not a free parameter. Two independent methods — numerical optimization and analytical solution — produce identical results (Table 41).

Table 41: Ascending node calibration results

Planet	S&S (°)	Verified (°)	Δ (°)	JPL (°)	Error
Mercury	32.22	32.83	+0.61	7.005	< 0.0001°
Venus	52.31	54.70	+2.39	3.395	< 0.0001°
Mars	352.95	354.87	+1.92	1.850	< 0.0001°
Jupiter	306.92	312.89	+5.97	1.304	< 0.0001°
Saturn	122.27	118.81	−3.46	2.486	< 0.0001°
Uranus	308.44	307.80	−0.64	0.773	< 0.0001°
Neptune	189.28	192.04	+2.76	1.770	< 0.0001°

14.5 Historical Observation Validation

The 3D simulation has been validated against over 700 historical astronomical observations spanning ~2000 BC to ~4000 AD: Mercury and Venus transits (~190 events), Mars oppositions (~140), Jupiter–Saturn great conjunctions (~150), and mutual planetary occultations (~100). Accuracy: < 1′ for the current epoch (±100 yr), < 5′ for historical (±1,000 yr), < 15′ for ancient (> 2,000 yr). Against JPL Horizons and historical transit/opposition data (~1800–2200 AD), per-planet RMS accuracy is: Sun 0.003°, Moon 0.002°, Mercury 0.079°, Venus 0.041°, Mars 0.090°, Jupiter 0.052°, Saturn 0.072°, Uranus 0.016°, Neptune 0.004°.

Independent observation benchmark. The accuracy figures above measure the model against modern numerical-integration ephemerides (JPL DE440/441, IMCCE INPOP19), which are themselves models. To validate against direct sky observations independent of any modern ephemeris, the model has also been benchmarked against Tycho Brahe's pre-telescopic Mars declinations (1572–1601, Opera Omnia vols. 10–13), the NASA/Espenak Mercury and Venus transit catalogues, and the Project Pluto mutual planetary occultation catalogue. At the epochs where these direct observations exist, the model matches them as well as — and for five of seven planets, measurably better than — JPL DE441 / IMCCE INPOP19 do at the same epochs (Table 42).

Table 42: Median declination error against the same independent historical observations, for this model (col. 2) and for JPL DE441 / IMCCE INPOP19 (col. 4), at the epochs of those observations. Ratio = model error relative to ephemeris error (< 1: model closer to the observations; computed per-event, hence not identical to the quotient of the two medians).

Planet	Indep. obs. median	(n)	JPL/IMCCE median	Ratio
Mercury	0.013°	23	0.159°	0.11×
Jupiter	0.013°	28	0.281°	0.11×
Saturn	0.022°	21	0.334°	0.22×
Neptune	0.002°	29	0.034°	0.19×
Uranus	0.020°	2	0.154°	0.09×
Mars	**0.177°**	**913**	0.240°	**1.04×**
Venus	0.101°	8	0.117°	1.20×

The Mars row is the most robust: 913 pre-telescopic naked-eye Tycho observations match the model at median 0.18° declination error — essentially even with IMCCE INPOP19 at the same epoch (ratio 1.04×), on a sample large enough to be statistically meaningful. The result is consistent with the model's residuals against JPL Horizons at extended ranges reflecting divergent extrapolation between the two models rather than a fitness deficit in this one.

14.6 Comparison with JPL DE440/441

The JPL Development Ephemeris (DE440/441; Park et al. 2021) is the gold standard for solar system dynamics, with independent confirmation from INPOP (Fienga et al., 2011) and EPM (Pitjeva, 2010) ephemerides.

Table 43: Obliquity predictions: model vs. La2004 (Laskar et al., 2004)

Year	Model	La2004	Diff.
1000 BC	23.8253°	23.8144°	+0.011°
J2000	23.4393°	23.4393°	0 (calib.)
3000 AD	23.3103°	23.3099°	+0.0004°
5000 AD	23.0650°	23.0639°	+0.001°
7000 AD	22.8508°	22.8553°	−0.005°
10,000 AD	22.6182°	22.6534°	−0.04°
12,000 AD	22.5359°	22.6081°	−0.07°
20,000 AD	22.7693°	23.0630°	−0.29°

The model and La2004 agree within 0.001–0.01° from −1,000 BC through 5,000 AD — essentially exact over this 6 kyr window. Agreement remains within 0.1° from 7,000 AD through 12,000 AD. By 20,000 AD the two diverge by ~0.29°, with La2004 oscillating back upward while the model continues its bounded $H/8$ cycle.

Table 44: Eccentricity predictions: model vs. Laskar et al. 2004 — the primary differentiating prediction

Year	Model	Laskar et al. 2004	Diff.
J2000	0.01671	0.01670	+0.00001
5,000 AD	0.01541	0.01534	+0.00007
11,725 AD	0.01255	0.01156	+0.00099
27,000 AD	0.00815	0.00263 (near min)	+0.00552

Both curves decline smoothly together — exact at 3,000 AD and within 0.001 to ~12,000 AD — and part company at the minimum: the one $H/3$ law bottoms at ~0.0078 around 32,682 AD, while Laskar is already in its minimum region at 27,000 AD (0.00263) — the model's minimum is shallower and later. A single harmonic line cannot reproduce the multi-mode secular beat exactly; the depth and date of the minimum is the discriminating prediction. For timescales beyond ~2,000 years, neither the model nor DE440/441 can be directly verified; both are extrapolations.

14.7 Error Analysis

Uncertainties propagate from the 6 free parameters. The dominant source is the obliquity amplitude (±0.01°), which grows linearly with time. Table 45 shows propagated uncertainties at two future epochs.

Table 45: Propagated uncertainties at future epochs

Epoch	Obliquity	Eccentricity
Yr 3000 (J2000 + 1 ka)	23.3103° ± 0.02°	0.01628 ± 0.0001
Yr 12000 (J2000 + 10 ka)	22.5359° ± 0.2°	0.01244 ± 0.001

14.8 The Derived Sun: The Certified Apparent Solar Longitude (DST-1)

The apparent solar longitude driving every eclipse computation in this paper is assembled from the framework's own structure with zero fitted solar constants, and is verified at 0.80″ RMS against JPL over the modern window — where the Meeus Ch. 25 reference itself, measured on the same window and instrument, reads 1.22″. Classical practice adopts the Sun from a fitted series (Meeus Ch. 25, VSOP87, or a numerical ephemeris); the framework instead *composes* it: $\lambda(t) = L_0 + n_{\text{trop}}(t - t_0) + D(t) + \mathrm{EoC}(e(t), M(t))$, where L_0 and the perihelion longitude are the two $J2000$ anchors, n_{trop} is the framework's mean tropical rate, and every remaining element is derived.

The drift term $D(t)$ is the integral of the model's own year-length physics. The tropical year oscillates on the H-lattice (twelve harmonics), dominated by an $H/8$ line of 19.28 s and an $H/3$ line of 7.23 s in an exact 8:3 amplitude ratio — one oscillation per equinox cycle — and the common amplitude factor is not fitted: it is $A \cot\varepsilon$, with $A = 0.63607°$ the invariable-plane inclination amplitude (itself pinned by the IAU 2006 obliquity rate) and ε the mean obliquity. A second, initially underestimated contribution enters through the luni-solar torque: the precession rate is obliquity-dependent ($\delta p = -p_0 \tan\varepsilon\, \delta\varepsilon$), and integrating this modulation on the lattice *scales* the two drift harmonics by $1 + p_0 \tan^2\!\varepsilon\, H/(2\pi \cdot \mathrm{div})$ — 1.306 for the $H/8$ line and 1.815 for the $H/3$ line. (A quadrature argument had suggested a

~3% effect; re-derivation showed both mechanisms lengthen the year at obliquity maximum and therefore add. The historical record then confirmed the structure independently of the derivation: the ancient eclipse corpus preferred the term's per-divisor scaling before it existed; see subsection 14.10.) $D(t)$ is evaluated in closed form — each harmonic's exact antiderivative on the integrated lattice phase plus a sine-saturated rebase that pins the drift and its slope to zero at $J2000$ by construction — so no lookup table and no fit window exist anywhere in the chain, and the same expression is bounded at deep time. The eccentricity entering the equation of centre is likewise derived, and it is the *same* law the lunar theory's E-factor rides (subsection 14.9): the framework's $H/3$ eccentricity line, $e(t) = e'_{\text{base}}(1 + \cos\theta_3/2)$ on the integrated phase, with e'_{base} derived from the observed J2000 eccentricity and the shared System-Reset anchor and no fitted coefficient; the cardinal-point chain rides this same law. One eccentricity law for Sun and Moon is a consistency requirement rather than a choice: eccentricity is frame-invariant and may carry only fixed-frame lattice periods, whereas the $H/16$ perihelion cycle is the $H/3$ rotation seen from the $H/13$-precessing equinox ($13 + 3 = 16$) and belongs to the perihelion longitude. An earlier form of the solar law added the $H/16$ slope on top of the $H/3$ line; against JPL over 1900–2100 that extra slope was the Sun's entire eccentricity-rate error, and removing it took the modern-window residual from 0.93″ to 0.80″. The last declared-fitted term of the planetary completion — a +1.42″ semiannual correction inherited from the finder's calibration — was identified as the semiannual nutation term in disguise; since the chain keeps Sun and Moon on the mean equinox of date, where nutation cancels in eclipse geometry, a Sun-only nutation term was a frame inconsistency, and its removal alone improved the syzygy elongation fleet from 3.88″ to 3.76″.

The assembled longitude is implemented once, in the published physics package, and consumed identically by the eclipse tier finders, the Besselian umbra engine, the verification engine, and the browser simulation — the visible scene rides the same certified longitude through a single overlay term $\delta = \lambda_{\text{certified}} - \lambda_{\text{twin}}$ applied inside a clock-convention window (full weight within 3,000 years of $J2000$, where the eclipse record lives on the TT clock, tapering to zero at 20,000 years where the deliberately-UT deep-time scene would clash with a TT-clock Sun). Against the NASA eclipse-path canon the chain places the computed umbra centerline at 2.2″ mean / 6.7″ maximum shadow-plane residual over 14 reference events and 42 fixed points (1900–2026). None of the historical-eclipse results below were used in constructing the Sun; they are predictions of the assembled structure. The complete derivation record, including the measured rejected alternatives, is public ("The Derived Sun" (DST-1) on the project website; docs 65 and 99 in the simulation repository).

14.9 The Derived Moon: A Framework-Native Lunar Theory (DLT-1)

Every constant of the Meeus Ch. 47 lunar theory used by the model carries an origin in the framework: derived from framework constants plus Newtonian gravity, attributed to a documented convention, observationally defined by a proven hypersensitive resonance, or anchored by design as a $J2000$ initial condition. The classical lunar tables (Brown, ELP2000, distilled by Meeus) are adopted numbers without origins; the framework re-derives the same theory in Meeus's own form using a first-principles three-body laboratory built from the model's constants alone, with no re-fitting. The remaining *fitted* content of the entire lunar theory is a single 5.1″ residual term plus coefficients below 0.15″ — and the 5.1″ term is itself decomposed by direct measurement, every part in one sign convention. The patch is Meeus − JPL: −1.13″ is *named* series truncation against the full 37,863-term ELP-2000/82B series (almost entirely the planetary family, which the abridged tables compress into three additive terms), and the remaining −4.05″ is the offset between analytic lunar theory and the JPL DE441 numerical ephemeris the correction was fitted against. That second half is *not* a step between analytic lineages: ELP-2000/82B and ELP/MPP02 agree to 0.03″ on this term, so both sit together and JPL sits ~4″ from each. It therefore has no series-term decomposition in any analytic theory, and is flat rather than growing across 2000–2050 — a fixed representational difference, attributed by cause rather than by term; documented model lineage, not free physics. Exactly one constant carries the *observationally defined* label: the drift rate of Meeus's small Venus-driven correction argument A_1 (131.849°/century), which sits on the $18V - 16E - M'$ near-resonance where parts-per-million differences in the planetary year lengths shift the beat by degrees per century — the framework establishes the mechanism, but no finite theory pins the value. All values quoted in this subsection are $J2000$-epoch values; their deep-time evolution is the subject of section 11.

The derivation covers all four content layers of the series. *Periodic amplitudes*: the top-20 longitude perturbation amplitudes are reproduced from three-body gravity at 100.0 ± 0.1%, and the latitude family at 100.02% once the inclination convention is resolved — the lunar orbit holds no fixed inclination — it oscillates between ~4.98° and ~5.30° over the 18.6-year node cycle — so the familiar 5.145° is a particular normalization rather than the mean of that swing. The catalog constant 5.1453964° is Brown's $\sin F$-normalization of the latitude series; the mean of the oscillation itself, measured from the same theory via its angular-momentum vector, is 5.1573°. Both are correct in their own convention, and the laboratory reproduces the ratio between them from pure gravity to 0.01%; the latitude family closes on the dynamical value. *Fundamental arguments*: the simulation's shipped default computes the five fundamental arguments framework-natively rather than from Meeus's empirical polynomials. The linear rates follow from the framework's star-referenced chain plus its own general precession $p = 360° \cdot 13/H$, which closes an otherwise-unexplained ±1.4°/century frame-bookkeeping drift in M' and F with zero new constants. The empirical T^2/T^3 secular terms are derived from a single physical channel: the solar perturbation on the lunar node and perigee scales as $(1 - e_{\oplus}^2)^{-3/2}$, and Earth's declining eccentricity weakens it secularly. The node's Meeus T^2 coefficient emerges at sensitivity $1.018 \approx 1$ (+7.34 predicted vs +7.47 arcsec/cy^2 empirical — a derived match); the perigee requires one anchored Clairaut-type sensitivity (2.407, the classical ≈2 rate amplification of apsidal motion), constant across orders. The eccentricity history driving the channel is itself fully derived — one movement: the same $H/3$ wobble cycle that carries Earth's inclination (whose minimum falls on the Balanced Year), expressed as $e(t) = e'_{\text{base}} (1 + \cos\theta(t)/2)$ from the derived mean e'_{base}, the Balanced Year, and H alone, with the observed $J2000$ eccentricity and its declining rate emerging as predictions at the 1–2% level and the channel bounded at every epoch. (The same $H/3$ line drives the solar equation of centre in subsection 14.8: eccentricity is frame-invariant and carries only fixed-frame lattice periods, while the $H/16$ perihelion cycle is the $H/3$ rotation seen from the $H/13$ equinox and belongs to the perihelion longitude — one eccentricity law for the Sun and the Moon.) This dissolves a classical sign puzzle — Brown's m^2 theory predicts the lunar perigee *accelerating* while the empirical polynomial *decelerates*: both are true, since the tidal *mean* rate slowly accelerates (the Lunar Precession Invariant of subsection 11.9) while the eccentricity channel is a bounded oscillation around it, currently in its decelerating phase. The remaining two arguments are identity-composed ($D = L' - L_{\odot}$, $M = L_{\odot} - \varpi_{\odot}$) with secular content from the model's *real-time* precession rates (the epoch-local values around their $H/13$ and $H/16$ means), completing a fully bounded five-argument skeleton with zero new constants.

The Moon's axial tilt: the obliquity of the lunar spin axis to the ecliptic — the one independently measured member of the catalog "tilt to orbit" composition — follows from the same machinery. The Moon occupies Cassini state 2, its spin axis co-precessing with the orbital node; the equilibrium obliquity is fixed by the gravity-gradient torque on the locked triaxial figure balanced against the node regression. Taking three published gravity constants (J_2, C_{22}, C/MR^2 from GRAIL and lunar laser ranging, Williams et al. 2014) together with the framework's own sidereal month, node rate and mass ratio, and integrating the full rigid-body rotation — three rotational degrees of freedom, torque from Earth and the Sun over the real orbit, no averaging assumption — gives $\varepsilon = 1.5470°$ against the measured 1.5424°: a match to 100.30% with nothing fitted. The averaging shortcut is worth recording as a caution: solving the same problem as an averaged torque balance for a body spinning uniformly about a *fixed* axis gives 1.5551°, because such a balance cannot contain the coupling between the pole and the physical librations; that coupling accounts for 64% of the difference from the measurement. The physics here is classical (Colombo 1966; Peale 1969) — what is new is only that the framework supplies the dynamical inputs and reproduces the observed tilt without adopting it. The residual 0.30% is the size of the known small channels not modelled (elastic tidal modification of the effective moments, degree-3 gravity, a two-layer fluid-core treatment) and is left stated rather than absorbed.

The secular budget against primary sources: the full T^2 coefficient of the lunar mean longitude decomposes, with zero free parameters, into the tidal channel, the Adams–Laplace planetary channel (Chapront et al., 2002), the Earth-figure (J_2) term, and the frame precession-acceleration term, closing against the empirical value to 0.08″/cy²; the T^3 tail is derived at 98.8% from the same channel's curvature, and the equinox precession acceleration $\dot{p}$ is composed from the laboratory's gravity-derived ecliptic-pole motion plus the framework's obliquity law at 104% of the IAU2006 value. *Optics*: the fitted right-ascension/declination correction historically carried by the simulation dissolves into analytic annual aberration plus the single 5.1″ residual term decomposed above.

The framework-native configuration is certified statistically indistinguishable from the pure-Meeus polynomials across the full NASA lunar canon (physical-event recall 99.6%, type accuracy within 0.15 percentage points of the Meeus-argument reference) while remaining bounded at deep time; re-certification after the identity-composed D/M completion left physical recall identical, moved opposition timings marginally closer to NASA than the pure-Meeus polynomials, and reclassified five events at the documented ±0.02 magnitude type boundary. The series was subsequently extended in three derived rounds, none of them fitted: five further Delaunay terms from the same three-body laboratory; the five-term *node family* (arguments on the lunar node, $M' \pm \Omega$, $2F + \Omega$, $2D + \Omega$, $F - \Omega$, which no integer Delaunay catalog contains) — produced by the laboratory only once Earth's oblateness is included, and certified by re-deriving the classical theory's two documented J_2 additives at 1.03 and 0.97; and 76 main-problem terms lying just below the Meeus tables' 0.4″ cutoff in argument classes no earlier extraction had enumerated, each confirmed real against dense JPL positions and derived at the census amplitude (the four the laboratory could not reproduce were left out). The shipped theory stands at 2.84″ (longitude) / 0.35″ (latitude) RMS against JPL over the modern window — the latitude at the resolution floor of the comparison itself, since the reference analytic theory agrees with JPL to only ~0.33″ there — with the ~4″ analytic-vs-DE441 representational offset identified above. Further longitude gains were measurable only by adjusting head amplitudes toward their ephemeris-fitted values, and were declined to preserve the every-constant-derived discipline. The complete derivation record — every experiment, budget, and gate — is public: the presentation document "The Derived Moon" (DLT-1) on the project website, and the technical record in the simulation repository (doc 66; see Data Availability).

14.10 Historical Solar Eclipse Validation: Pure-Tidal + $\alpha(t)$ ΔT vs Stephenson Empirical Fit

The ΔT formula derived in subsection 11.2 from the lunar-distance evolution of Farhat et al. (2022) and angular-momentum conservation, together with the L1-orbital-coupled $\alpha(t)$ GIA correction derived in subsection 14.11 from independent satellite gravimetry and tied to the L1 orbital layer of the Climate Formula, has been tested directly against the documented historical solar-eclipse record. This subsection presents the solar visibility test; the higher-resolution lunar timing test on the 267-event working set from Stephenson et al. (2016) is in subsection 14.11.

The solar test proceeds in two steps. First, a ΔT-independent Moon-polynomial cross-check against the NASA *Five Millennium Catalog* on 11 canonical events isolates Moon-polynomial accuracy from ΔT contribution.[3]

[3] A prior test entry labelled "Cambyses eclipse" was excluded after Stephenson (1997) confirmed that no documented Babylonian solar eclipse

Second, a scan-window alignment audit on 26 documented events spanning −762 Bur-Sagale/Nineveh to 2026 Burgos tests whether the framework's own predicted umbra track reaches the documented observation site within a ±4-hour window; the audit uses the model's own predicted UT and umbra track, so it is ΔT-polynomial-free and independently indexes the framework's Earth-rotation prediction against the documented record.

Moon polynomial cross-check against NASA. As a foundation step the simulation's Moon polynomial (Meeus Ch. 47, 60 longitude + 60 latitude perturbation terms) was cross-validated against the NASA *Five Millennium Catalog of Solar Eclipses* (Espenak & Meeus, 2006) for $n = 11$ canonical events spanning −524 to 985 CE. The comparison is performed in Terrestrial Time and is therefore ΔT-independent: any residual is purely a Moon polynomial accuracy question. The mean $|TT|$ residual is **6.9 minutes**, worst case 14.0 minutes (year 980). This is the expected Meeus Ch. 47 polynomial residual at $\sim$ 1,000 years from $J2000$ ($\approx 0.13°$ in Moon ecliptic longitude). The polynomial holds across the entire historical eclipse record without deep-time correction. (This diagnostic characterises the Meeus-argument polynomial baseline; the shipped chain — the derived Sun of subsection 14.8 and the extended derived lunar series of subsection 14.9 — reads 2.2″ mean umbra-centerline residual on the modern NASA canon.)

The lunar series feeding both tests is itself framework-derived: every constant of the Ch. 47 theory carries a derived, attributed, observationally defined, or design-anchored origin (subsection 14.9).

Alignment audit on 26 documented eclipses. For each of the 26 documented events, the framework's own simulation produces both the model UT of greatest eclipse and the umbra-track geometry at that UT. Over a ±4-hour scan around each documented preset UT, the audit records where the model umbra passes closest to the observation site and classifies each event into one of five verdict categories, summarized in Table 46. Two summary metrics roll up: *alignment* (peak umbra hits the observation site at or near the framework's own UT) and *scan-reach* (some moment within the ±4-hour window brings the umbra within 1,000 km of the observation site).

Table 46: Framework ΔT vs 26 documented historical solar eclipses (−762 to 2026 CE), 5-verdict distribution over a ±4-hour scan window per event. Alignment = confirmed + off-peak; scan-reach = alignment + regional + ΔT+regional.

Verdict category	Count
Confirmed (peak umbra hits observation site at framework's own UT)	3/26
Off-peak (peak umbra hits observation site near, not at, framework UT)	13/26
Regional (scan-window match, umbra within 1,000 km at some ΔUT $\neq 0$)	5/26
ΔT+regional (framework UT differs *and* umbra needs ΔUT to reach site)	0/26
Geographic class (umbra *centerline* > 1,000 km at every scanned moment; penumbra may still cover the site)	5/26
Alignment (confirmed + off-peak)	**16/26**
Scan-reach (alignment + regional + ΔT+regional)	**21/26**

The framework umbra reaches the observation site in $21/26$ **events within the** ±4**-hour scan window, and lands at or near framework-UT peak on** $16/26$ **events.** The audit is ΔT-polynomial-free: it uses the model's own predicted UT and umbra track, so it is an independent test of the model's Earth-rotation prediction against the documented record — not a comparison against any smoothed observational fit. The 5 regional matches carry small ΔT-signal offsets but succeed on the scan-window criterion. The 5 geographic-class events are the late-tenth-century Cairo cluster (four events) plus the −647 Babylon early-diary partial, and for these the class is a site-association artifact rather than a path error: the model's central paths for the Cairo-dated eclipses match the NASA canon's greatest-eclipse positions to 65–290 km, and the records themselves are partial-phase observations — the first-hand Ibn Yunus 977 report is a genuine 0.60-magnitude partial at Cairo, while the second-hand Said al-Andalusi entries are adjudicated as duplicates (978, 979 → the 977 Dec 13 eclipse) or misdated (985 → 982 Sep 20). The class records umbra-*centerline* distance, not eclipse visibility: at high γ the shadow strikes the tilted Earth obliquely and the penumbral footprint spans thousands of kilometres, so partial-phase records at off-path sites are exactly the expected presentation — the −135 Babylon diary's planets-visible language is consistent with this. The full adjudication (including the chronology-free sexagenary-day identification of the −708 Lu record) is documented in the simulation repository.

The non-tidal contribution: full Munk-MacDonald rejected, GIA-scale confirmed, fractional non-tidal carried by the Core-mantle swing. Before the $\alpha(t)$ GIA correction was added to the model, the pure-tidal-only ΔT showed a constant linear excess over Stephenson of approximately 1.96 s/yr integrated into the past: $\sim$ 4,850 s at year −524 and $\sim$ 2,048 s at year 977. This pattern was suggestive of a constant Length-of-Day difference of order 5–6 ms — the magnitude of the canonical Munk-MacDonald non-tidal Earth-rotation assumption (Munk & MacDonald, 1960), conventionally attributed to glacial isostatic adjustment plus core-mantle coupling.

With the L1-orbital-coupled $\alpha(t)$ correction now incorporated (see subsection 14.11 for derivation), the constant linear excess is absorbed in the ancient era: pure-tidal + $\alpha(t)$ at year −762 agrees with Stephenson to within $\sim$ 50 s. The remaining structured signal is a bump-shaped medieval residual peaking in the 840–1020 CE window (exact peak year is reference-polynomial-dependent), plus a small fractional non-tidal channel of ~0.5 ms/century (window-average) detected in the higher-resolution lunar timing test, carried by the Core-mantle swing episode — characterized fully in subsection 14.11.

Umbra-centerline diagnostic on the conventional documented dates. A diagnostic effort tightened the 1,000 km penumbra-reach criterion of Table 46 by roughly 10× to the umbra centerline itself, and en route isolated and removed an ad-hoc visualisation-layer rotation overlay (a $\Delta T \times 2\pi/86400$ correction layered on top of standard GMST(UT1)) that had made the visible umbra disc render at the geographic locations Stephenson et al. (2016) documents while masking a systematic offset relative to the model's underlying pure-tidal

exists from Cambyses II's reign — the Cambyses-era eclipses recorded in the Babylonian astronomical diaries and Ptolemy's *Almagest* V.14 are both lunar.

physics. Under the current umbra chain — the framework-native Sun of subsection 14.8 and the derived lunar series of subsection 14.9, through a single Besselian umbra implementation in the published physics package — the centerline instrument reads, at the *conventional* documented dates: −708 Lu State 9 km, −556 Nabonidus 104 km, −762 Bur-Sagale/Nineveh 174 km, −584 Thales/Anatolia 211 km, and −135 Babylon 198 km — the entire first-hand ancient corpus at off-peak class with no chronology re-attribution required (an earlier +14-yr Lu re-attribution hypothesis is withdrawn: the Chunqiu's sexagenary-day record identifies the traditional −708 date uniquely, chronology-free). On the modern NASA eclipse-path canon the same chain reads 2.2″ mean / 6.7″ maximum shadow-plane centerline residual over 14 events and 42 fixed reference points. The 21/26 scan-window result of Table 46 sits above this centerline test as a broader threshold, and both are satisfied by the same underlying model geometry.

The −135 Babylonian eclipse. The −135 April 15 Babylonian eclipse (recorded in the Babylonian astronomical diaries BM 45745 + LBAT 1285, four-planet astronomical fingerprint, double-dated Arsacid Era 175 = Seleucid Era 239; one of the most scholarly-secure attributions in the historical corpus, re-confirmed by Stephenson & Steele (2006)) is an off-peak-class row of the verdict taxonomy in Table 46. The framework's own UT of greatest eclipse (06 : 05) is within 9 minutes of the documented UT (06 : 14) — essentially no ΔT-signal on this event — and within the ±4-hour scan window the framework umbra passes within 198 km of Babylon at ΔUT = $-0h54$, with the framework's local-circumstance computation reading deep-totality-boundary magnitude at the site on the traditional date. The Meeus Ch. 47 Moon polynomial is exonerated for this event (all modern lunar theories converge within 0.001° at year −135). Full component-level decomposition and the identification-cascade evidence are in the simulation repository.

Reproducibility. The complete solar-eclipse validation methodology, the underlying numerical inputs, and ten interactive diagnostic buttons (NASA cross-check; per-event same-day check; 26-event eclipse alignment audit; etc.) are publicly available in the simulation repository (see Data Availability). The 26 documented eclipses (spanning −762 Bur-Sagale to 2026 Burgos, and including modern reference eclipses Eddington 1919, Halley 1715, Henry I 1133, 2024 Dallas total) are exposed as in-app browsable presets where the user can step through each event and visually verify Moon-Sun alignment in the 3D scene.

14.11 Lunar Eclipse Validation: $\alpha(t)$ GIA Correction vs 270 Primary-Source Lunar Observations

Complementary to the solar visibility test of subsection 14.10, the lunar timing test exploits the fact that lunar eclipses are visible across Earth's entire night-side hemisphere. Geographic localization is irrelevant, so the constraint reduces to per-event *timing* of opposition — resolving ΔT to within minutes per event rather than the ∼50–100 s resolution of the solar visibility test. This subsection presents the validation against 270 primary-source lunar observations (267-event three-way-comparable working set) and 89 primary-source solar observations from Stephenson et al. (2016), derives the L1-orbital-coupled $\alpha(t)$ GIA correction from independent satellite gravimetry and the Climate Formula's L1 orbital layer, and characterizes the remaining medieval-era residual as a three-component structural decomposition (framework-native sub-Milankovitch $8H$-lattice harmonics — the shipped 4-flag stack: Bond, Hallstatt, Jose5, Jose4; the Core-mantle swing episode; and a broad-band noise floor) — with an eight-hypothesis test whose aggregate-level correlations (H3, H6, H7) fail per-era robustness and are downgraded to drift-tracking artifacts.

The $\alpha(t)$ climate-driven GIA correction. Earth's polar moment coefficient $\alpha = C/(M \cdot R^2)$ is no longer treated as a strict constant in the model. It evolves via Glacial Isostatic Adjustment (GIA) — the *solid-Earth* response to a changing ice load, not the surface load itself. Beneath a growing ice sheet the mantle flows away from the load towards lower latitudes; that mass moves *away* from the rotation axis, so α and the moment of inertia $I = \alpha \cdot M \cdot R^2$ rise and the rotation rate $\omega = L_{\text{Earth}}/I_{\text{Earth}}$ falls — glaciation lengthens the day. Deglacial rebound reverses the flow poleward, lowering α and ticking ω up. The sign must be read from this solid-Earth flow and *not* from the surface ice/water exchange, which acts in the opposite direction: grounded ice sits near the rotation axis while the ocean water it was drawn from lies far from it, so the direct surface load alone would make glaciation *shorten* the day. The two act as separate channels with opposite climate signs; they are compared below. Critically, $\alpha(t)$ is a purely Earth-internal mass redistribution: it does NOT transfer angular momentum to the Moon, so the Moon-distance evolution of Farhat et al. (2022) and Kepler's 3rd law for the Moon are untouched. Only the $L_{\text{Earth}} \leftrightarrow \omega$ partition shifts; the total Earth-Moon angular momentum $L_{\text{Total EM}}$ is conserved.

Ice-mass redistribution has two components: the one-way Holocene rebound from the last glacial maximum, and the underlying glacial cycle itself — ice sheets building up and melting on ∼100 kyr timescales driven by orbital forcing. The framework couples $\alpha(t)$ directly to the L1 orbital layer of the canonical Climate Formula (subsection 10.5), the same layer that fits the LR04 δ^{18}O record over 0–1 Myr:

$$\alpha(t) = \alpha_{J2000} - k \cdot [L_1(\text{year}) - L_1(2000)] \tag{39}$$

where $L_1(\text{year})$ is the L1 layer evaluated in δ^{18}O ‰. One physical mechanism, two observables: the same L1 orbital signal drives both the ice-volume proxy in the sediment record and the α-driven length-of-day oscillation.

The formulation is anchored on three independent literature inputs, none fitted to eclipse data:

- $\alpha_{J2000} = 0.3306947$ (IERS Conventions 2010) — present-day boundary value.
- $d\alpha/dt(J2000) = -1.35 \times 10^{-11}\,\text{yr}^{-1}$, translated from $dJ_2/dt = -2.7 \times 10^{-11}\,\text{yr}^{-1}$ (Cox & Chao (2002), confirmed by Cheng et al. (2013)) via the axisymmetric-GIA geometric factor $dJ_2/d\alpha = 2.0$ (Peltier ICE-6G; Peltier (2004)) — modern rate boundary condition.
- $L_1(\text{year})$ coefficients — 33 harmonics on integer divisors

of $8H$, coefficients from the Climate Formula's fit against LR04 δ^{18}O.

The single new parameter $k = -3.67 \times 10^{-7}$ ‰$^{-1}$ is calibrated so that $d\alpha/dt$ at $J2000$ under Equation 39 matches the Cox–Chao rate exactly. That calibration is not fitted to eclipse data — it is fixed by satellite gravimetry.

Three-way comparison vs primary-source lunar observations. The dataset comprises 270 timed lunar observations from Stephenson et al. (2016) supplementary tables S01 (Babylonian) + S02 (Babylonian ziqpu) + S04 (Almagest) + S05 (Chinese) + S07 (Greek) + S09 (Arab). The headline metric is computed over the 267 of those 270 events for which all three ΔT predictions are defined — the remaining three fall outside the NASA Espenak/Meeus polynomial's published validity range or have missing per-event ΔT in Stephenson et al. (2016), so they cannot participate in the three-way comparison. For each qualifying event, three ΔT predictions are compared: the Stephenson-derived per-event "observed" ΔT, the NASA Espenak/Meeus polynomial averaged over the observation year, and the model's pure-tidal + $\alpha(t)$ GIA prediction. The per-event mean |residual|:

	Mean |residual| (s)	Mean |residual| (min)
NASA Espenak/Meeus ΔT	1,199	20.0
Model pure-tidal + $\alpha(t)$ GIA (L1-orbital)	1,213	20.2

The model's mean |residual| is 20.2 min against these primary-source observations, and the framework beats NASA on 118/267 events (44.2%) at the per-event level. The trend anchor, 4-flag stack, and Core-mantle swing are calibrated jointly against the Espenak & Meeus (2006) ΔT polynomial 1650–2017. Both NASA and Stephenson et al. (2016) are polynomials fit to overlapping subsets of the same lunar dataset, so a per-event residual against either indexes fit quality against a smoothed representation of the observations rather than physical validity. The framework's independent validation is the solar-eclipse alignment of subsection 14.10, which does not depend on any ΔT polynomial.

Cross-source consistency. After detrending with the linear slope (−1.88 s/yr under the L1-orbital $\alpha(t)$), the four independent observation traditions agree on the model's residual magnitude to within a few hundred seconds:

Source	Tradition	n	Detrended mean (s)	RMS (s)
S01	Babylonian	125	−44	2252
S02	Babylonian (ziqpu)	21	−342	1302
S04	Babylonian (Almagest)	9	+258	1768
S05	Chinese	69	+174	1050
S07	Greek (outlier)	11	−794	1509
S09	Arab (medieval)	**32**	**+57**	**763**

S09 (Arab medieval — Ibn Yunus, Habash al-Ḥāsib, al-Battānī) is the tightest at ±57 s with RMS 763 s. Four observation traditions separated by thousands of years and tens of thousands of kilometres agree on the residual magnitude to within the noise floor — cross-cultural agreement at this level confirms the residual is a property of the model fit, not a regional observational bias.

Independent solar cross-validation. The same three-way comparison pipeline applied to 89 primary-source solar observations from Stephenson et al. (2016) supplementary tables S03 (Babylonian, 25 events), S06 (Chinese, 42 events), and S08 (Arab, 22 events) gives a model mean residual of 666 s vs NASA's 672 s, with the framework beating NASA on 42/89 events (47.2%). The absolute residuals are smaller than the lunar case because solar observations have tighter intrinsic precision. The per-century overshoot magnitude in years 800–1300 CE matches between lunar and solar datasets, confirming that ΔT is a property of Earth rotation independent of eclipse type — the type-independence requirement passing.

An open Bond IRD correspondence — not a cross-validation. A separate comparison of the shipped ΔT stack (4 flags + Core-mantle swing) against an entirely independent paleoclimate archive — Bond et al. (1997) North-Atlantic ice-rafted-debris (IRD) proxy stacks — yields Pearson correlation $r = +0.37$ across the $-4,000$ to $+1,800$ CE window, with sign convention — warm epochs expected at $\Sigma_{\text{stack}} > 0$, cold at $\Sigma_{\text{stack}} < 0$, i.e. a warm climate coincides with a *longer* day — agreeing on 4 of 5 major named events in that interval. The IRD record is a direct paleoclimate observable of North-Atlantic ocean-atmosphere rhythm, independent of Earth-rotation history, and the stack was never fitted to it. The correspondence is nevertheless *not* established as physical, and we do not claim it as external validation. Four null tests are reported here so the correspondence is not over-read.

First, the correlation accounts for only ~13% of variance. Second, the event-level sign agreement of 4 of 5 samples one hand-picked year per named period; scored instead across the *full* period bands it holds for 65% of years against a 50% coin-flip baseline, and for *none* of the Little Ice Age (1300–1850 CE), where Σ_{stack} remains positive across all five centuries. Third, matching the stack's zero-crossings to ten named climate transitions gives a median offset of 262 yr against a Monte-Carlo null median of 353 yr — $p \approx 0.19$, not significant. Fourth, and most directly, band-limited testing against phase-randomised surrogates leaves no framework harmonic significantly phase-aligned with either the IRD record or GISP2 once the 16 tests performed are accounted for — the sole nominal hit ($p = 0.046$) is one of those 16. At the Bond period specifically the stack and the IRD record are close to *anti-phase* (175°), and permitting a drifting phase via windowed phase-tracking does not recover alignment (PLV $p = 0.49$).

The correlation is therefore real as a number but is not carried by the $8H/1830 = 1,466$-yr band, and it cannot be used as evidence that the lattice periods are the climate periods. The four cycles rest on their ΔT closure, which is what they were fitted to and what they achieve; the further inference to a climate mechanism remains open (Figure 24). A flags-only stack scores higher ($r = +0.49$), consistent with the Core-mantle swing being core-supplied angular momentum rather than climate; but since neither figure survives the null tests above, the difference between them should not be read as confirming the two-engine amplitude budget.

Two climate-coupling mechanisms, opposite signs. Climate reaches Earth's rotation through two physically distinct mechanisms whose signs are opposite — standard geophysics, independent of this framework, but a distinction that must be kept explicit because each is routinely stated with the other's mechanism. The **surface-mass** mechanism: warming melts grounded ice into the ocean, moving mass away from the rotation axis, so the day lengthens, essentially concurrently with the climate signal. The **solid-Earth (GIA)** mechanism: warming unloads the crust and the mantle rebounds poleward, lowering α, so the day *shortens* — lagging the climate forcing by the mantle's relaxation time, ~4–6 kyr.

The two are not on equal evidential footing here. The $\alpha(t)$ channel *implements* the solid-Earth mechanism by construction, anchored on Cox & Chao (2002) satellite gravimetry, so that identification is secure. The ΔT stack is *hypothesised* to carry the surface-mass mechanism, and the $\Sigma_{\text{stack}} > 0 \Rightarrow$ warm convention — which the 4-of-5 score above tests — is that hypothesis stated, not an established property of the harmonics. It is precisely what the null tests above fail to support. The opposition is not a defect but the reason the deglacial spin-up of the following paragraph *leads* rather than coincides with peak interglacial warmth. It also means the two channels need not agree about any given epoch: at J2000 the GIA term is −0.35 ms/cy while the stack term is −1.88 ms/cy and descending toward its 2206 trough, so they currently indicate the same sign for different reasons and on different lags. Any index built by summing the two must therefore enter them with opposite signs and account for the offset lag; naive addition cancels the physics it is meant to expose.

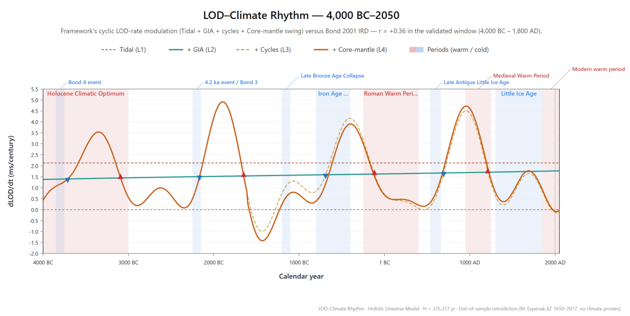

Figure 24: Framework d LOD/dt layers (Tidal L1, +GIA L2, +Cycles L3, +Core-mantle L4) against the Bond-cycle harmonic across the validated window $-4,000$ to $+1,800$ CE ($r = +0.37$ vs Bond et al. (1997) IRD), with named warm/cold periods shaded. High-rate phases align with warm periods (Roman, Medieval), near-zero phases with cold ones (Little Ice Age).

Run further backwards, out of sample, the stack makes an additional retrodiction. During deglaciation the GIA channel reaches its maximum spin-up (Tidal+GIA baseline minimum ~0.9 ms/cy near 10,600 BC), so stack troughs push the total rate *below zero*: episodes clustered between ~23,000 and ~1,300 BC in which the day transiently shortened, deepest at ~−2.4 ms/cy near 8,600 BC (tidal +2.12, GIA −1.1, stack trough −3.4). The shipped stack additionally places the present day inside such an episode: the net rate at J2000 is marginally negative (−0.07 ms/cy, descending phase since ~1980), consistent in sign with the observed post-2020 spin-up. Sign-flipping rates have mainstream precedent on shorter timescales — the observed post-2020 spin-up (subsection 9.4), the decadal core-mantle negative phases of Holme & de Viron (2013), and the near-zero troughs of the ~1,500-yr oscillation of Stephenson et al. (2016) — but a sustained deglacial excursion of this depth is a framework retrodiction, testable against eclipse-independent Holocene rotation proxies. In the same window the depressed baseline centres the stack swings on zero, flipping the sign of the day's drift every few centuries through the Older Dryas–Younger Dryas–8.2 ka sequence; the rhythm's periods are comparable to the Younger Dryas' own duration, so this is pacing context, not an explanation — the established meltwater/AMOC mechanism for those events stands.

Testing candidate mechanisms and structural decomposition of the medieval residual. After the $\alpha(t)$ correction absorbed the dominant first-order residual, a smaller bump-shaped overshoot (~ 1,000 s peak in the 840–1020 CE window — the exact peak year is reference-polynomial-dependent, see below — with FWHM ~ 660 yr under the L1-orbital-coupled $\alpha(t)$ of Equation 39) remained in the medieval era. Structural diagnostics show the residual decomposes into a linear secular drift plus a single symmetric bump in the medieval window — one mechanism each for drift and bump. Specifically, the raw signed Δ(year) shape is not antisymmetric about any candidate crossover year (best raw-antisymmetry score −0.87), but after removing the linear trend the detrended residual is symmetric around year 990 CE with score 0.97. The $|\Delta|$ pattern shows large excess in both the ancient BCE and medieval CE eras; the two-humped appearance in $|\Delta|$ terms is the drift-dominated side (ancient BCE) and the drift+bump side (medieval CE) of the same drift+bump superposition, seen through the $|\cdot|$ operator, not two independent excursions. Reference-polynomial robustness (Stephenson 2016 spline vs a NASA-catalog locally-smoothed reference) shows shape correlation $r = 0.82$ and RMS Δ magnitude within 2%, but peak-year shifts by 180 yr between references (Stephenson 1020 CE vs NASA-derived 840 CE) — the "peak in the 840–1020 CE window" claim is robust; single-number claims of exact peak year and exact peak magnitude are reference-conditional.

Eight candidate mechanisms have been tested against the L1-orbital residual, summarized in Table 47. Aggregate-level correlations that initially appeared significant (H3, H6, H7) fail per-era robustness: their apparent signal is driven by the shared secular drift and does not survive within-era testing. The residual decomposes into three components: (i) sub-Milankovitch oscillations at four framework-native $8H$-lattice periods — four **spectral signals with lattice labels**: each physical rhythm is a band in the record's spectrum whose nearest lattice label is $8H_0/n$ on the integer representative $H_0 = 335,317 = 23 \cdot 61 \cdot 239$: the Bond-scale $8H/1830 = 1,466$ yr harmonic (74 × Jupiter-Saturn synodic at 0.22%; only 4 yr from the canonical ~1470 yr Bond cycle of Bond et al. (2001); the physical anchor is Jupiter-Saturn synodic dynamics via Charvátová's solar inertial motion mechanism); the Hallstatt-scale $8H/1104 = H/138 = 2,430$ yr harmonic (structurally the sixth sub-harmonic of $H_0/23 = 14,579$ yr; corresponds to the well-established Hallstatt solar-activity cycle at ∼2400 yr documented in cosmogenic-isotope reconstructions of Damon & Sonett (1991) and Steinhilber et al. (2012)); the $8H/2989 = 897$ yr harmonic ($5 \times$ Jose 179 yr, Charvátová (2000), at 0.28% offset); and the Jose4 $8H/3749 = 716$ yr harmonic ($4 \times$ Jose 179 yr at 0.083% offset — the tightest structural anchor of any 600–800 yr candidate; identified via cross-archive spectral coherence in the Steinhilber et al. (2012) ^{10}Be solar-activity reconstruction and the Bereiter et al. (2015) EPICA CO_2 record). With the integer representative H_0, all four labels happen to share a factor with H_0 ($\gcd(n, H_0) > 1$: 61 for Bond and Jose5, 23 for Hallstatt and Jose4) — a bookkeeping regularity of the representative that served as a candidate-enumeration heuristic in the divisor scans, not a physical selection rule; selection rests on cross-archive empirical significance (Steinhilber ^{10}Be, EPICA CO_2, Bond IRD). Amplitudes and phases for the four harmonics are fit-derived (constrained physical priors against the Stephenson ΔT residual, using cap-only shipping where the prior is a maximum bound, never a floor) — the 4-flag stack is shipped default-ON with each cycle individually toggleable for A/B measurement; shipping the fitted amplitudes/phases violates the paper's original zero-eclipse-fit design at the amplitude/phase level, which is documented openly in-code. Only the periods are structural zero-fit predictions. Component (ii) is a linear *fractional* non-tidal secular rate of ∼0.5 ms/century (∼10% of Munk-MacDonald, ∼2× Cox-Chao GIA-only). Component (iii) is a broadband noise floor at the ∼ 20-min per-observation precision level. Component (ii) is a real physical signal, carried by the Core-mantle swing episode.

Under the L1-orbital $\alpha(t)$ of Equation 39, the aggregate mass-balance integrated correlation (H3) reaches $r = -0.381$ ($p < 10^{-4}$) on the lunar dataset, but a per-era diagnostic — correlating within each of the four archaeological eras (Babylonian, Chinese, Arab, European) individually — shows the correlation collapses to $|r| < 0.15$ within every era. The aggregate signal is therefore drift-tracking: both mass balance and the residual carry the same secular linear trend, and their alignment on that shared drift is what produced the ∼4σ aggregate correlation. It does not represent a within-era coupling. The same per-era test similarly disposes of the Path A solar-inertial-motion and Test 5 planetary-perihelion follow-ups: any candidate carrying a monotone secular component produces the same shape of aggregate-level correlation with the drifting residual, so no aggregate-level correlation can be interpreted as a within-era physical channel until per-era robustness is passed. None of the tested candidates does. The full statistical methodology (Bonferroni multiple-comparison correction, white-noise null comparison for spectral peaks, jackknife robustness, independent-dataset replication, per-era decomposition) is documented in the simulation repository (see Data Availability).

Table 47: Eight tested candidate mechanisms for the medieval residual under the L1-orbital $\alpha(t)$ of Equation 39. H3, H6, and H7 aggregate correlations fail per-era robustness (details in the paragraph below); the remaining channel is component (ii), a fractional non-tidal ∼0.5 ms/century drift.

#	Hypothesis	Outcome (L1-orbital $\alpha(t)$)
1	Constant mantle-core coupling at Holme (1998) secular rate	Full HdV rate rejected (Babylonian ΔT over-corrected by ∼2,700 s). A fractional ∼0.5 ms/century (∼10% Munk-MacDonald, ∼2× Cox-Chao GIA-only) IS detected in the linear residual — time-varying mantle-core coupling, carried by the Core-mantle swing episode (see Data Availability).
2	Mass-balance ↔ residual (instantaneous)	$r = -0.108$, $p = 0.065$ (borderline null)
3	Mass-balance integrated $Y \to 2000$, with solar replication	Aggregate $r = -0.381$ ($p < 10^{-4}$) collapses to $\lvert r\rvert < 0.15$ within each era ⇒ drift-tracking, not physical coupling (see below and per-era diagnostic).
4	Mass-balance lagged ($\Delta \in [0, 1000]$ yr scan)	Lunar best-lag null ($r = -0.108$ at $\Delta = 0$); solar $r = +0.246$ at $\Delta = 200$ ($p = 0.020$); sign mismatch ⇒ no coherent lagged coupling.
5	Mass-balance signed sign-duration	Lunar null ($r = -0.054$); solar $r = -0.228$ ($p = 0.033$) — same sign, only solar significant.
6	Nine literature periodic forcings (10–2500 yr) via Lomb–Scargle	0/9 at FAP < 5% against the shipped residual — no unexplained periodic forcing remains in the record.
7	14.2-yr peak focused robustness (from #6)	Passes every in-catalog robustness test, but the observation epochs' own spectral window peaks at 14.30 yr (a ∼7.15-yr eclipse-cadence comb) ⇒ sampling-window artifact; a real 0.15-ms decadal LOD line would integrate to only ∼0.12 s of ΔT, four orders below the fitted amplitude.
8	Lunar nodal cycle (18.6 yr) targeted in medieval data alone	Peak at 18.7 yr, FAP = 70.6% (well above 5%).

What this establishes. The three-way non-tidal decomposition of subsection 14.10 (full Munk-MacDonald rejected, GIA-scale included, fractional ∼0.5 ms/century carried by the Core-mantle swing) together with the three-component residual decomposition developed above (framework-native sub-Milankovitch $8H$-lattice harmonics — the shipped 4-flag stack: Bond, Hallstatt, Jose5, Jose4; the Core-mantle swing episode; broadband noise) fixes the geometry of the medieval-era problem. Four independent observation traditions agree on the model's residual magnitude. The fractional non-tidal channel is identified as time-varying mantle-core coupling — the millennial core–mantle rotation swing of Stephenson et al. (2016) and Dumberry & Bloxham (2006), corroborated by archeomagnetic core-flow reconstructions, with a uniform secular alternative disfavored at $\sim 4\sigma$ by a signed solar-drift bound. The remaining scientific work is independent (non-eclipse) calibration of the lattice-harmonic and swing amplitudes against physical mechanisms measurable outside the eclipse record; archeomagnetic calibration is currently blocked by a known ~300-yr field-model phase-lead systematic.

The testable prediction: a ~250 ms Milankovitch LOD oscillation. Under Equation 39, α oscillates with the ~100 kyr, ~41 kyr, and precession-band periodicities that drive climate. This translates to a ~250 ms peak-to-peak length-of-day oscillation in phase with the glacial cycle (Figure 26), with LOD peaks at MIS 6 (~140 ka BP), MIS 2 / LGM (~22 ka BP), and the projected next-glacial onset (~60,500 AD, coincident with the Climate Formula prediction of Equation 28), and troughs at MIS 7e, MIS 5e Eemian, and today's Holocene. Figure 25 shows the rate-domain signature across the last two glacial cycles with the LR04 record itself overlaid: the Tidal+GIA baseline rides above the tidal line through ice-sheet growth and dips sharply at the two deglaciations, with the deepest negative-rate excursions at Termination II (→ Eemian) and Termination I (→ Holocene). No LOD data entered the climate fit and no climate data entered the LOD fit — the alignment is the shared mechanism.

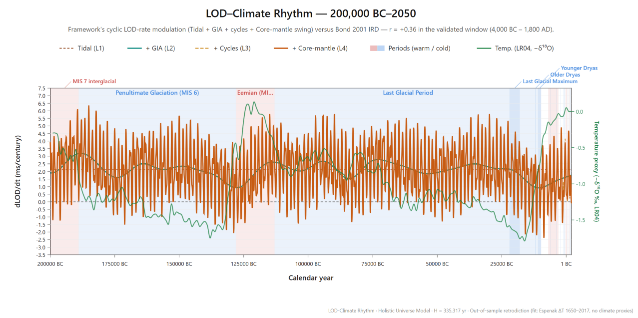

Figure 25: Framework $\mathrm{d\,LOD}/\mathrm{d}t$ across the last two glacial cycles (200,000 BC–2050 CE) with the LR04 benthic stack (Lisiecki & Raymo, 2005) as inverted δ^{18}O (green, secondary axis; positive = warm). The Tidal+GIA baseline (teal) carries the ~41/100-kyr $\alpha(t)$ modulation of Equation 39, driven by the same L1 orbital layer fitted to LR04 in the Climate Formula; the 4-flag stack (gold) supplies the millennial envelope. The deepest spin-up excursions align with the two deglaciations.

The underlying *ice* → J_2 → α → *LOD* link is directly confirmed on decadal timescales by Cheng et al. (2013): LAGEOS J_2 transitions from linear GIA-driven decrease to acceleration around 1998, attributed to polar ice-mass loss — the same mechanism, observed at satellite timescales. The 100-kyr extrapolation follows from the same physics but is not yet directly observable in ~50-year satellite records. **The physical claim is that planetary gravity, climate, and Earth rotation are one coupled system, connected by ice mass as the mediator**: the millennial-scale LOD variation (section 15 Prediction 14) and the climate-cycle glacial onset (section 15 Prediction 19) are the same underlying signal viewed through two observables.

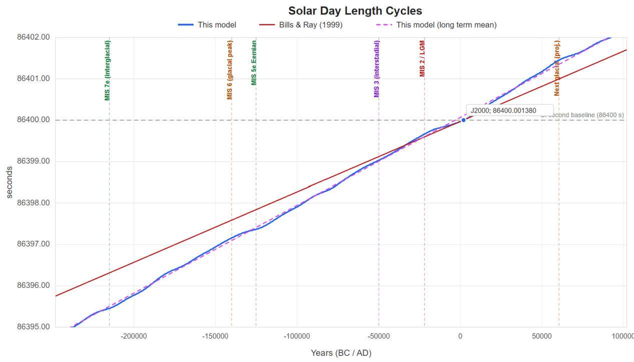

Figure 26: Model prediction (blue) for Earth's mean solar day length over −248 kyr to +102 kyr under the L1-orbital $\alpha(t)$ of Equation 39, versus a linear tidal-recession extrapolation (red) at the modern lunar recession rate of ~3.82 cm/yr (Dickey et al., 1994) projected forward and backward. The L1-coupled $\alpha(t)$ produces a ~250 ms peak-to-peak oscillation on top of the smooth tidal trend, with LOD peaks (glacial: MIS 6, MIS 2 / LGM, projected next-glacial) and troughs (interglacial: MIS 7e, MIS 5e Eemian, Holocene / J2000) aligned to the L1 orbital extrema of the Climate Formula (subsection 10.5). The dashed purple curve marks the long-term climate mean — the LOD trajectory Earth would follow with α held at its glacial-cycle mean $\langle\alpha\rangle = \alpha_{J2000} + k \cdot L_1(2000)$ rather than at its J2000 snapshot value. Blue oscillates around this mean line; the ~0.14 s gap between the mean and the J2000 anchor reflects the fact that J2000 sits at an interglacial extremum of L_1 ($L_1(2000) \approx -1.04$ ‰, near its minimum), so $\alpha(J2000)$ is at an oscillation edge, not the cycle centre. The blue dot marks the J2000 model anchor at $86,400.001480$ s; the horizontal dashed grey line marks the SI-second baseline at 86,400 s. Same L1 layer drives both the LOD signal (α) and the δ^{18}O record — one mechanism, two observables.

Reproducibility. The complete lunar-eclipse validation methodology, the $\alpha(t)$ physics derivation, the eight ruled-out hypotheses with full statistical methodology, and twenty in-app diagnostic buttons (foundation tests; predictive finders; NASA Canon cross-check; primary observation tests; residual investigation) are publicly available in the simulation repository (see Data Availability). The L1-coupled $\alpha(t)$ prediction of Figure 26 is reproducible via the Formula Verification → Solar Day Length → Export Cycles view in the interactive simulation.

15. Testable Predictions

The model generates 27 specific predictions (20 spanning near-term through long-term timeframes, plus 7 deep-time claims from the Expanding Solar System Resonance Theory and the L1-coupled rotation channel):

15.1 Near-Term (Decades)

1. **Mercury perihelion anomaly**: the projected excess $42.71''$/cy (Table 35) drifts with the perihelion longitude and the obliquity by about $+0.3''$/cy per millennium,

whereas the relativistic advance is constant; the measured excess ($42.980 \pm 0.002''$/cy) already sits $0.27''$/cy above the projection, so the statement is an identity to 0.6 %, not a replacement of GR, and BepiColombo's ranging value does not test it (section 12).

2. **RA at maximum declination**: The Sun's ICRF right ascension at June solstice oscillates about a mean of $5^{h}47^{m}22^{s}$ with amplitude $\sim \pm 3.125°$ ($\sim \pm$ 12.5 min), driven by two co-equal H-lattice components ($H/3$ and $H/8$). It has sat near the top of that range throughout recorded history, peaking at $6^{h}00^{m}04^{s}$ in 1675 AD, and is now declining at $\sim 5.5''$/century. The turnover is very flat — about one second of RA across 750 years — so the 1246.03125 AD alignment epoch, which anchors H, is indistinguishable from the peak at this resolution rather than being a feature of this curve.
3. **Jupiter and Saturn perihelion trends — a retired prediction, kept for the record**: The model originally predicted the current trends continue without pattern change, with Saturn permanently ecliptic-retrograde on $-8H/65$. That claim was made falsifiable, tested with the model's own N-body engine, and retired: the retrograde is the window phase of the Great-Inequality epicycle (long-term mean prograde, g_6), so the divisors are window-epoch descriptors — the J2000-window rate sits at $\sim -3{,}140$ to $-3{,}400''$/cy — and the model now agrees with the Great-Inequality reversal on its ~450-year flank (subsection 6.2).
4. **No major Planet Nine** (key differentiator): A two-tier test rejects all proposed candidates. The *primary* test is Law-4 compliance (subsection 5.1): all Batygin–Brown / Siraj candidates fail by 4–7 orders of magnitude; the upper-mass threshold for compatibility at high-eccentricity ETNO orbits sits near $\sim 2 \times 10^{-10}\ M_\oplus$ (~2-km rocky asteroid). The *secondary* confirmation is a canonical 1.2-billion-evaluation v-balance search: the best 9-planet min(Law 3, Law 5) balance achievable with a 5 $M_\oplus$ body at 450 AU is ~9%, vs. the 8-planet baseline (99.9974% Law 3, 99.8636% Law 5). The Vera Rubin Observatory (LSST, 2025–2035) discriminates against the conventional Batygin & Brown (2016) 4–10 $M_\oplus$ at 290–700 AU hypothesis — itself contested by the OSSOS null result (Lawler et al., 2017).
5. **Small classical-belt KBO obliquity clustering** (bidirectional Law 4): Inverting Law 4 (Equation 12) gives axial obliquity ≈36.6° for a representative ~124-km cold-classical-belt KBO ($m \approx 10^{-12}\,M_\odot$ at $\rho \approx 2\ \mathrm{g\,cm^{-3}}$) at $a \approx 45$ AU, $e \approx 0.05$, $d = 55$ (a 100-km body at the same density gives ≈26°) — distinguishable from the uniform-random Lambert expectation (mean obliquity ≈57°) by ~30%. The claim is population-statistical and restricted to sub-200 km low-e classical-belt bodies (Col-OSSOS, $\sim 10^4$–10^5 candidates); named TNOs and comets/asteroids fail per-body for the reasons documented in subsection 5.2. The Vera Rubin Observatory will constrain rotation poles for $\sim 10^3$ small TNOs via lightcurve inversion. A clustering near ~30°–50° supports the bidirectional Law-4 extension; uniform-random restricts it to the primary-planet domain.

15.2 Medium-Term (Centuries)

6. **Axial precession period**: Currently below the mean ($\sim 25{,}771$ vs $\sim 25{,}794$ yr, i.e. precessing faster than average) and still decreasing. The model predicts a minimum of $\sim 25{,}312$ yr around $\sim 12{,}443$ AD (~481 yr below the $H/13$ mean), followed by a maximum of $\sim 26{,}051$ yr around $\sim 32{,}357$ AD (~257 yr above the mean), continuing to oscillate on the perihelion precession cycle. The Capitaine formula is a polynomial extrapolation that does not model this oscillation.
7. **Obliquity divergence** after the next minimum ($\sim 13{,}664$ AD at ~22.51°): model predicts a reversal back toward the mean on its $H/8 = \sim 41{,}915$-yr cycle, while standard polynomial extrapolations continue to diverge. Long-term envelope: 22.21°–24.72°.
8. **Longitude of perihelion divergence** after ~3,000 AD.
9. **Gregorian calendar drift**: June solstice slips from June 21 (J2000) to June 17 by $\sim 11{,}725$ AD — a ~4-day shift driven by the Gregorian year (365.2425 d) running slightly long against the model's solar year (~365.2422 d) plus secular changes in obliquity, eccentricity, and the equation of centre.
10. **Analemma shape changes**: the figure-8 shifts forward with the perihelion precession cycle, its *width* oscillates with eccentricity (the $H/3$ line; the $H/16 = \sim 20{,}957$ yr perihelion-direction cycle shifts it forward) and its *length* oscillates with obliquity ($H/8 = \sim 41{,}915$ yr cycle).
11. **Cardinal-point braid drift rates**: the braid law (subsection 9.6) fixes the differential drift rates of the four per-point tropical years with zero per-point freedom — at J2000, relative to the common mean: SS +0.4, WS −0.4, VE +1.5, AE −1.6 s/century, two near-opposite pairs summing to zero. Century-scale precision timing of equinoxes and solstices must reproduce this quadrature pattern, and any high-precision decomposition of cardinal-point timing residuals must place the fine structure in the counter-rotating sideband only; a coherent co-rotating component at measurable amplitude falsifies the one-vector geometry.

15.3 Long-Term (Millennia)

12. **Eccentricity minimum at $\sim 32{,}682$ AD**: ~0.0078, then increasing — shallower and later than the La2004 minimum. Key differentiator from Milankovitch theory.
13. **Inclination minimum at $\sim 32{,}682$ AD** (J2000-anchor projection; the deep-time correction over this ~335-kyr interval is sub-decade): ~0.845° to the invariable plane (the next balanced year, one full Earth Fundamental Cycle after the previous one). Earth's inclination then rises again on its H-year cycle.
14. **Length of Day variation**: LOD will monotonically increase under Driver 1 (Earth-Moon tidal recession) at a modern rate of ~1.7 ms/century, with a superimposed ~250 ms peak-to-peak Milankovitch oscillation from the L1-orbital $\alpha(t)$ of Equation 39. LOD peaks at glacial extrema (next projected peak at ~60,500 AD, coincident with the next-glacial onset of Prediction 19 below), and troughs at interglacial extrema (today's Holocene at $J2000$; next interglacial trough at ~164,000 AD). Short-term fluctuations (e.g. the 2020–present speedup) sit on top of this trend. See Figure 26.

15. **Solar year in days**: Decreases secularly under Driver 1 (LOD growth → fewer, longer days per year; section 11), with the $H/8$-band harmonic oscillation of subsection 9.5 superimposed — no near-term reversal.
16. **Sidereal year in seconds**: Held at the J2000-anchor value $31,558,149.76$ s within this section's millennial scope; at deep time it drifts via Driver 2 (solar mass loss → Kepler) — see section 11.
17. **Precession periods locked to** $8H$: All planetary perihelion, axial, and obliquity periods will remain expressible as integer divisors of $8H$ (with $8H_{J2000} = 2,682,536$ yr; absolute value rescales with $H(t)$ per section 11, the $8H/N$ integer divisors are invariant at any epoch).
18. **Invariable plane tilt**: Mean = 1.48113° with ±0.63607° amplitude.
19. **Orbital cooling onset and next glaciation peak**: The canonical Climate Formula (subsection 10.5) fit on the post-MPT regime and extrapolated forward 250 kyr predicts the next natural glaciation peak at ~58,500 yr from now (~60,500 AD), the strongest glaciation in the next quarter-million years at ~196,500 yr, and the warmest interglacial in the window at ~164,000 yr (Figure 16). The two strong glaciations sit ~138 kyr apart, longer than the ~100 kyr post-MPT pacing. The qualitative finding agrees with Berger & Loutre (2002)'s ~50 kyr-to-next-glaciation prediction (~17% from the canonical ~58.5 kyr). Anthropogenic CO_2 may delay the next natural glaciation by 50+ kyr in moderate-emission scenarios (Ganopolski et al., 2016); this is not included in the formula.
20. **Planet obliquity cycles**: Every planet follows the same two-component formula as Earth (Equation 15), with amplitude from Law 2. Three cycles confirmed (Mercury, Earth, Mars), three remain testable (Jupiter, Saturn, Uranus); Venus and Neptune cancel exactly to constant obliquity (Table 11).

15.4 Deep-Time

The Expanding Solar System Resonance Theory of section 11, together with the L1-coupled $\alpha(t)$ rotation channel, produces seven additional falsifiable claims spanning Earth's full 4.54 Gyr Earth-Moon history.

21. **Earth-Moon genesis at the rigid Roche limit at the giant-impact age**: Run backwards, the proper-physics formula crosses the rigid Roche limit ($1.48\,R_\oplus \approx$ 9,500 km) at ~4.498 Ga — the canonical giant-impact Moon-formation age (~4.5 Ga), ~40 Myr after Patterson's Pb-Pb Earth age of 4.54 Gyr — with no Hadean constraint used in the fit (subsection 11.4). Any refinement of the Moon-formation age or the genesis distance should remain consistent.
22. **Devonian** $H \approx 306,189$ **yr**: The model's Devonian H produces 399.96 days/year, matching Wells (1963) ~400 days/year to within 1% (Table 31). New high-precision paleontological day-count techniques (e.g. de Winter et al. (2020)-style *Torreites* bivalve sampling) should reproduce this match.
23. **Integer-label invariance across geological time**: L1 lattice fits to paleoclimate spectra at Devonian, Permian, and Cretaceous epochs should find the same integer set identified in the post-MPT LR04 fit ($n = 65$ for obliquity main, $n = 22/25/28$ for the 100-kyr band, etc.) — only with rescaled absolute periods (subsection 11.10). A deep-time spectrum that fits a substantively different integer set falsifies the invariance claim.
24. **Future tidal-lock asymptote at** $87.1\,R_\oplus$: Lunar laser ranging extrapolated forward through full tidal Q-decay should converge on the angular-momentum boundary at 555,623 km Moon distance, reached at roughly 50 Gyr (well beyond the Sun's red-giant phase). A converged asymptote outside ~80–95 $R_\oplus$ would falsify the angular-momentum calculation.
25. **Cheng cross-proxy persistence**: The L1 lattice currently fits the Cheng et al. (2016) Asian Monsoon δ^{18}O record at $R^2 = 0.68$ on its independent U-Th radiometric chronology (subsection 10.11). As new high-precision speleothem chronologies extend the record or refine its dating, the same 33-integer lattice should continue to fit with comparable R^2. A substantially degraded fit (e.g. $R^2 < 0.5$ on a refined or extended Cheng record) would falsify both the lattice's cross-proxy persistence and the integer-label-invariance claim above.
26. **Lunar precession scales as** $(H/H_0)^2$ **across geological time** (subsection 11.9). The Moon's apsidal period was ~9.69 yr at the Devonian and ~17.15 yr at −2.5 Gyr, with $T_{\text{apsidal}} \times H \approx 2,966,728$ yr^2 at every epoch. Independent deep-time reconstructions of the lunar apsidal period (via spectral analysis of tidal rhythmites or cyclostratigraphic records sensitive to perigean modulation) should reproduce the $H_0^2/H(t)$ track within ~1%; a Phanerozoic apsidal period substantially off this track would falsify the invariant.
27. **Deglacial spin-up leads the interglacial optimum by ~5–10 kyr**: sustained negative $\mathrm{d\,LOD}/\mathrm{d}t$ occurs nowhere in the framework's 200-kyr record except during the two major deglaciations (GIA-channel rate minima ~−1.2 ms/cy at ~10,600 BC and ~127,800 BC; Figure 25). Because the GIA rate term tracks the melting rate — α follows ice volume (more ice displaces mantle equatorward, raising α), so $\mathrm{d}\alpha/\mathrm{d}t \propto \mathrm{d(ice)}/\mathrm{d}t$ and melting drives α down — the rate *minimum* marks maximum melting speed, and peak interglacial warmth follows ~5–10 kyr later, when melting completes: the derivative leads the integral. It is the minimum that carries the information, not the sign; the GIA rate stays negative for millennia after melting ends because the mantle goes on rebounding (−0.35 ms/cy at $J2000$, with the ice sheets long gone). Any eclipse-independent paleo-rotation record should therefore show the spin-up episode *preceding* the Holocene Climatic Optimum and the Eemian peak by several kyr; a record showing it concurrent with or after peak warmth would falsify the $\alpha(t)$ coupling's phase structure. Causality runs climate → rotation (ice → J_2 → α → LOD): the rotational signature is a leading *indicator* of peak warmth, not a driver.

The classical **precession of the equinoxes scales with** $H(t)$ (subsection 11.3) is itself an additional structural prediction of ESSRT — Earth's axial precession period $T_{\text{axial}} = H/13$ was ~23,553 yr at the Devonian and ~4,970 yr at the Earth-Moon genesis, with a modern-era rate of change of ~6 yr per Myr that is in principle observable in high-precision

IAU precession-rate measurements over decades.

15.5 Falsification Criteria

Each major claim of the model maps to a specific falsifier and observational test. The model would be falsified if any of the following outcomes is observed:

Table 48: Falsification criteria: each major claim mapped to its specific falsifier and observational test.

Claim	Falsifier	Test
Bounded eccentricity oscillation (Earth–Saturn coupling, section 5)	Eccentricity continues monotonic decline toward ~0 as Milankovitch theory predicts, rather than reaching a bounded minimum near ~~0.0078 at ~32,682 AD	Millennia of continued tracking
100,000-yr climate cycle is a multi-planet eigenmode-beat signal (section 10); empirical centroid is the $s_1 - s_4$ nodal eigenmode beat at 107.3 kyr	Direct eccentricity forcing confirmed: bispectral 95k+125k coupling detected and 405-kyr term at predicted dominant amplitude in post-MPT LR04	Continued LR04 / longer non-tuned record analysis
Mercury reference-frame effect (section 12)	Geocentric precession remains constant at ~5,604″/cy over decades	BepiColombo science operations, April 2027
No major Planet Nine (Law-4 compliance + Laws 3/5 closure)	Body more massive than ~2×10^{-10} $M_\oplus$ found at hundreds of AU in long-term high-eccentricity orbit (Law-4 violation)	Vera Rubin / LSST 2025–2035

Structural assumption. Several of these falsifiers — the Saturn ecliptic-retrograde permanence (subsection 6.2), the Mercury reference-frame effect (section 12), and the no-major-Planet-Nine claim — depend on treating the Fibonacci balance as *predictive*: the closure of the 8-planet structure is a real physical constraint that forbids deviations. If the structure were merely *descriptive* (a coincidence fit to the 8 planets we happen to observe), then a future detection inconsistent with these claims could be accommodated by re-fitting the Fibonacci d-values rather than falsifying the framework. The model's broader claim — formation-epoch freezing of KAM-stable Fibonacci configurations (section 7) — treats the balance as predictive; the BepiColombo and LSST results will discriminate which interpretation is correct.

Table 49: Quantities the model reproduces, cross-validated against published references and standard ephemerides.

Quantity	Reference	Model agreement
Sun position (1800–2200 AD)	JPL Horizons	RMS < 0.003°
Moon position (1800–2200 AD)	Meeus (1998) / JPL Horizons	RMS < 0.002°
Planet positions (1800–2200 AD)	JPL Horizons	RMS < 0.1°, all seven planets (Earth is the observer)
Solar / lunar eclipse timings	NASA eclipse catalog	matched to within minutes
Earth obliquity + rate of change	Laskar et al. (2004); Capitaine et al. (2003)	within published uncertainties
Earth eccentricity at J2000 + near-J2000 rate	JPL, NASA	match
Earth longitude of perihelion + rate	Meeus (1998)	1246 AD perihelion–solstice alignment exact
Year lengths (tropical, sidereal, anomalistic, cardinal)	Capitaine et al. (2003)	match incl. 1-extra-tropical-year-per-axial-cycle identity
Day lengths (solar, sidereal, stellar)	IAU 2006	match incl. 1-extra-sidereal-day-per-axial-cycle identity
Axial / inclination / perihelion / obliquity / ecliptic precession (Earth)	Capitaine et al. (2003)	within published uncertainties
Ascending nodes (invariable plane)	Souami & Souchay (2012)	match to < 0.0001° (subsection 14.4)
Planet inclinations (ecliptic + invariable)	JPL J2000	match
Planet eccentricities (J2000)	JPL J2000	match
Planet obliquities	published values	within 0.2–2.5%
Laskar et al. (2004, 2011) secular eigenfrequency periods	published numerical secular solutions	model's analytical $8H/N$ matches to 0.04–2.5%
Berger (1978) climatic-precession peaks	published spectrum	match $8H/N$ integer lattice to < 0.7%

of all eight planets through a single timescale. The framework produces closed-form formulas for any epoch, eliminating the need for numerical integration within its domain of applicability.

16.2 Scope: What the Model Reproduces, Where It Differs

The empirical content of the model is summarised in two compact tables. The first lists quantities the model reproduces, cross-validated against published references; the second lists topics where the model proposes a different explanation than the current scientific consensus.

Together, the two tables show the model is incremental rather than revolutionary: every observation in the literature is reproduced, with disagreements localised to six specific topics whose discriminating tests are catalogued in section 15.

16.3 Relationship to Existing Theory

The model does not contradict Newtonian gravity. It proposes that the long-term behavior of planetary parameters may be captured by a geometric description that reveals Fibonacci structure — consistent with KAM theory's predic-

16. Discussion

16.1 What the Model Explains

The Holistic Universe Model unifies six phenomena — axial precession, inclination precession, perihelion precession, obliquity variation, eccentricity variation, and day/year length changes — within a single geometric framework. Beyond Earth, six Fibonacci Laws connect the orbital properties

Table 50: Topics where the model proposes a different explanation than the current scientific consensus.

Topic	Standard view	Model's view
Mercury's ~43"/cy anomaly	Confirmation of General Relativity (Einstein 1915)	The relativistic advance, derived from the model's own constants; the once-proposed frame-projection reading reproduces it at the 0.6% level for Mercury only and falls 0.27″/cy (~50σ) short of the ranging precision — recorded as a tested identity, not the cause (section 12)
Jupiter–Saturn Great Inequality	Required to explain Saturn's retrograde perihelion phase	Not required — Saturn precesses ecliptic-retrograde as a structural feature of the 8H lattice (integer divisor $-8H/65$, invariant under section 11; subsection 6.2)
Length of Day pre-1900 (ΔT)	Monotonic tidal slowing produces ΔT polynomial	Millennial cyclic modulation of the LOD growth rate superimposed on tidal slowing (subsection 9.4)
Earth's eccentricity decline	Continues toward ~0.01 (Newcomb 1898 / Harkness 1891 / Meeus 1998 polynomials)	Bounded oscillation; minimum at ~32,682 AD, then rises (Table 44)
100,000-yr glacial cycle origin	Direct eccentricity forcing	Multi-planet eigenmode-beat signal modulating Earth's orbital plane (section 10)
Earth's $H/3$ inclination cycle	Inclination ICRF rate derived from planet ecliptic perihelion rates (Laskar / Berger)	Planet ecliptic-inclination rates of change as the *input* for perihelion ICRF period changes — same observable, different attribution

tion that maximally stable orbits have frequency ratios converging to the golden ratio. The formation-epoch mechanism (section 7) provides a physical explanation for the planetary-spacing scale: KAM-selected Fibonacci configurations were frozen during protoplanetary disk dissipation and preserved by conservative dynamics for 4.5 billion years. The **Expanding Solar System Resonance Theory of section 11** extends this stability picture to the deep-time evolution layer. The **Earth-family** lattice labels stay invariant across geological time — a structural prediction that paleo-day-counts from Wells 1963 Devonian corals to Williams 2000 Ediacaran rhythmites test directly — while their absolute periods rescale monotonically via Earth-Moon tidal evolution; the planetary system rides the second, far slower expansion tier (solar mass loss, uniform in the ratios). The two layers — KAM-protected planetary spacing on one side, action-angle closure of the 8H climate lattice on the other — are compatible mechanisms at different scales (subsection 7.4), and both persist across the full 4.54 Gyr Earth-system record while remaining within standard Newtonian mechanics.

Every observation the model reproduces comes from established astronomy. The model adopts the work of the established authors below in full; where the *interpretation* of a specific observation differs, that is flagged in the right column.

Bottom line. Every observation is identical to standard astronomy. The Fibonacci-lattice structure that emerges when those observations are re-organised into a single timescale

Table 51: Relationship to prior theoretical work. Each row names a source whose data or framework the model adopts; the right column flags any specific interpretive disagreement.

Source	Used by the model	Where the model differs (if anywhere)
Kepler — orbital geometry, three laws	Adopted in full	—
Newton — universal gravitation	Adopted in full	—
Le Verrier / Newcomb — Mercury ~43"/cy measurement	Adopted as the observation	The residual is carried as the relativistic advance derived from the same constants; the frame-projection identity is recorded with its measured verdict (section 12)
Einstein 1915 — general relativity	Adopted — the ~43"/cy advance is derived from the model's own constants and carried as such	The earlier frame-effect proposal is retired with its test record (section 12)
Berger (1978) — Milankovitch Fourier decomposition	Adopted as the standard reference spectrum	Per-peak planet attribution differs — same periods, different responsible planets; cross-tabulation gives 0 of 33 fully agreeing (subsection 10.7)
Laskar et al. (2004, 2011, 1993) — numerical secular solutions	Adopted as cross-validation	The model's analytical 8H/N periods match Laskar's secular eigenfrequencies to 0.04–2.5%; the derivation is geometric rather than numerical
Meeus (1998) — *Astronomical Algorithms*	Adopted for Moon position (RMS < 0.002°), longitude-of-perihelion, and the 1246 AD anchor	—
Capitaine et al. (2003) — IAU 2000/2006 precession expressions	Adopted as the standard formulation for Earth precession comparison	—
Chapront et al. (2002) — lunar orbital parameters and ecliptic reference frame	Adopted (with Meeus 1998) for Moon position and ecliptic-frame consistency	—
Souami & Souchay (2012) — invariable plane orientation	Adopted as ground truth for ascending nodes (model matches to < 0.0001° after calibration, subsection 14.4)	—
IAU 2006 P03 — axial precession rate ~~26k yr	Adopted as the current-epoch observation	Snapshot of a cycle averaging ~25,794 yr ($H/13$); below-mean trend predicted to reverse (section 15)

(H, 8H) is new, and the explanations for the specific anomalies above (Mercury, Saturn ecliptic-retrograde perihelion, the 100-kyr cycle origin, and the $H/3$ attribution) are new. Everything else converges with established science.

16.4 Limitations

The model does not explain:

- **Why** $H_{J2000} = 335,317$ specifically (the Fibonacci ratio 13:3 is understood via KAM theory, but the absolute timescale at J2000 is empirical; under section 11 the value is set by the conjunction of modern LOD, the Phanerozoic tidal-rate average, and the Farhat 2022 deep-time curve, not by independent freedom)

- Short-term perturbations or chaotic orbital evolution

The model describes secular (long-term) trends only. It does not include short-period perturbations that average to zero over millennial timescales:

Table 52: Physical effects not included in the model

Perturbation	Period	Effect	Treatment
Lunar nodal cycle	18.6 yr	±9″ nutation	Averaged out
Chandler wobble	~433 d	Axis wobble (0.7″)	Not modeled
Annual wobble	1 yr	Seasonal mass redistrib.	Not modeled
Jupiter perturbations	~11.86 yr	Orbital variations	Averaged out
Saturn perturbations	~29.5 yr	Orbital variations	Averaged out
Solar activity cycle	~11 yr	Minor thermal effects	Not modeled

For the model's primary predictions (obliquity, eccentricity, longitude of perihelion over millennia), these perturbations contribute $< 0.01°$ to obliquity, < 0.0001 to eccentricity, and $< 0.1°$ to longitude — within the model's stated uncertainties. For precise positions on any given day, standard ephemerides (JPL DE440/441) should be used. The J2000-snapshot parameterisation (fixed H, fitted per-line climate amplitudes) applies from ~1 million years ago (Mid-Pleistocene Transition) to the present epoch; beyond that window the framework remains valid through the deep-time rescaling of section 11 (integer labels invariant, absolute periods evolving with $H(t)$), while the climate-formula *amplitudes* are per-regime and do not transfer across regime boundaries (subsection 10.5).

16.5 The Overfitting Concern

With 6 free parameters (5 continuous, 1 discrete configuration), overfitting is addressed by:

1. Explicitly separating calibration from predictions (section 14)
2. Agreement with values not used in construction (eccentricity, invariable plane inclination, ascending nodes to $< 0.0001°$)
3. 27 testable predictions, several falsifiable within decades, including 7 deep-time claims from the Expanding Solar System Resonance Theory (section 15, section 11)
4. $R^2 > 0.99998$ for all 7 planets using a single formula structure
5. Six Fibonacci Laws predicting orbital properties with zero free parameters, with suggestive exoplanet parallels

16.6 Invitation to Test and Refine

The model is offered as a framework for testing scientific theories rather than as a closed theoretical statement. Every observable in the published literature is reproduced (Table 49); six deliberate departures from current consensus are catalogued explicitly (Table 50), each with a discriminating empirical test catalogued in section 15. The complete simulation source, all fitted coefficients, the deep-time chain, the climate-formula fits, and the verification pipelines are publicly available under GPL (see Data Availability).

We invite independent replication and contradicting evidence. Concrete invitations include: testing the Mercury reference-frame prediction against BepiColombo measurements from April 2027 (section 12); applying the L1 $8H$ integer-divisor lattice to Devonian, Permian, or Cretaceous cyclostratigraphic spectra to test integer-label invariance (subsection 11.10); reproducing the Wells 1963 / Wu et al. (2024) paleo-day-count match via different paleontological techniques; testing the Lunar Precession Invariant $T_{\text{apsidal}} \times H = \text{const}$ (subsection 11.9) via spectral analysis of deep-time tidal rhythmites; identifying any planetary or stellar system whose eccentricity oscillations would violate Law 4 (subsection 5.1); or extending the historical eclipse validation (subsection 14.10, subsection 14.11) with newly recovered primary-source observations. The framework treats contradicting evidence as the most productive form of engagement.

17. Conclusions

We have presented six Fibonacci relations of planetary motion derived from a unified geometric model. The relations connect a single timescale — the 335,317-year Earth Fundamental Cycle, produced by two counter-rotating reference points in a 13:3 ratio — to the orbital properties of all eight planets:

1. **Law 1**: The Earth Fundamental Cycle divided by Fibonacci numbers generates Earth's major precession periods (a hierarchy unique to Earth)
2. **Law 2**: A single constant ψ (derived from Earth) predicts all eight inclination amplitudes from Fibonacci divisors and mass alone ($d \times \text{amp} \times \sqrt{m} = \psi$)
3. **Law 3**: Angular-momentum-weighted inclination oscillations balance to 99.9974% (with phase-derived base eccentricities)
4. **Law 4**: A single constant K (derived from Earth) predicts all eight eccentricity amplitudes from Fibonacci divisors, mass, distance, and mean obliquity: $e_{\text{amp}} = K \times \sin(\bar{\varepsilon}) \times \sqrt{d}/(\sqrt{m} \times a^{3/2})$ (subsection 5.1)
5. **Law 5**: An independent eccentricity balance reaches 99.8636% from the same Fibonacci divisors, with base eccentricities derived from the System Reset phase (90° in-phase, 270° Saturn); predicts Saturn's eccentricity from the other seven planets to ~0.27%
6. **Law 6**: Jupiter's ICRF perihelion and Saturn's ecliptic perihelion lock to a single period, $8H/65$ — a structural balance, not a coincidence, and the obliquity beat in Earth's climate; Earth's own obliquity sits one lattice integer away at the Fibonacci anchor $H/8$ ($= 8H/64$), closing the Fibonacci identity $3 + 5 = 8$

A significance analysis using a direct joint permutation test over the 4 empirical tests (model-independent; joint null captures inter-test correlation by construction) yields a combined p-value spanning 1.5×10^{-4} (permutation null) to 1.0×10^{-6} (MC nulls over 9 tests), equivalently 3.62–4.75 σ. A leave-one-out jackknife confirms that all eight planets are required to reach the full significance: dropping any single planet reduces the combined signal, with Jupiter and Uranus being the most load-bearing. A physical origin mechanism explains the structure's precision: KAM-selected Fibonacci configurations were frozen during protoplanetary disk dissipation and preserved by conservative dynamics for 4.5 billion years.

These laws produce specific consequences for Earth: a unified obliquity formula tracking standard theory to within ~0.5° over ±20,000 years (and predicting bounded oscillation in the 22.21°–24.72° envelope where polynomial extrapolations diverge), a single $H/3$ eccentricity law (shared with the lunar theory and the solar equation of centre) reaching its next minimum at ~32, 682 AD, a decreasing Mercury perihelion anomaly testable by BepiColombo (~575.31″/cy versus MESSENGER's 575.31″/cy, science operations from April 2027), and a new explanation for Saturn's ecliptic-retrograde perihelion precession ($\sim -3,422''$/cy geocentric predicted versus $\sim -3,400''$/cy observed). The Milankovitch beat frequency structure reveals that all five standard precession cycles emerge as H/n with Fibonacci-related indices, with the Fibonacci subtraction property guaranteeing physical closure of the beat equations.

The canonical three-layer Climate Formula (section 10) operationalises this orbital structure on the climate record: a 33-integer L1 lattice on $8H$ (positions fixed by orbital geometry, only per-line amplitudes fitted to climate) plus a 3-line L2 silicate-weathering carbon thermostat plus 6 L3 Heaviside step transitions at major Cenozoic boundary-condition changes, fit per regime by sequential ridge regression. Per-regime R^2 reaches 0.87 (post-MPT LR04), 0.85 (EPICA CO_2), and 0.76 (CenCO2PIP 0–66 Ma); the forward projection within the post-MPT regime places the next natural glaciation peak at ~58,500 yr from now. Two structural tests further characterise the formula: cross-tabulating the 33 lattice integers under both the Berger eigenmode-beat convention and the model's per-planet PLANET_CYCLES attribution gives **0 of 33** fully agreeing on both planet and mechanism (subsection 10.7); adding the classical Berger 1978 insolation features (ε, e, $e \sin \varpi$, $e \cos \varpi$) on top of L1+L2+L3 yields $\Delta R^2 \leq 0.004$ in every LR04 regime tested (subsection 10.8), and $\Delta R^2 = 0$ on LR04 under Laskar 2010 eccentricity substitution. The 100,000-year glacial cycle is captured as one specific case within this framework, with the empirical 100-kyr-band centroid at the $s_1 - s_4$ nodal eigenmode beat at 107 kyr (a planet-pair orbital-plane coupling) and Berger's classical 95-kyr peak at the adjacent $g_4 - g_5$ eccentricity eigenmode beat ($n = 28 = 95.8$ kyr).

A unified ~2, 400-term formula system (planet-specific term counts 2,393–2,435) predicts planetary precession with $R^2 > 0.99998$ for all 7 planets (Table 37). The model uses 6 free parameters and is fully transparent about calibration versus prediction.

The Expanding Solar System Resonance Theory of section 11 extends the structural framework to geological time: the lattice's integer labels remain invariant while absolute periods rescale monotonically under two independent drivers (Earth-Moon tidal evolution, solar mass loss). Two deep-time invariants emerge — the day-count near-invariant $H \times$ days/yr $\approx 122,471,920$ (drifting by ~1,000 ppm back to the Earth-Moon genesis) and the structurally exact **Lunar Precession Invariant** $T_{\text{apsidal}} \times H =$ const (held to zero drift at every epoch by the framework's $(H/H_0)^2$ scaling, consistent with Brown's leading-m^2 perturbation theory).

The ΔT formula derived from the same Earth-Moon angular-momentum framework, augmented with an L1-orbital-coupled $\alpha(t)$ GIA correction anchored on independent satellite gravimetry (Cox & Chao (2002)) and tied to the L1 orbital layer of the canonical Climate Formula, has been validated against the historical eclipse record on two complementary tracks: 26 documented solar eclipses spanning −762 to 2026 CE (subsection 14.10; 21/26 events with the framework umbra reaching the observation site within a ±4-hour scan window, 5/26 geographic-class events on the umbra-centerline metric) and the 267-event working set of primary-source lunar observations from Stephenson et al. (2016) (subsection 14.11; 20.2-min mean |residual| under the current Espenak & Meeus (2006)-calibrated trend anchor + 4-flag stack + Core-mantle swing). The underlying Moon polynomial agrees with NASA's *Five Millennium Catalog* (Espenak & Meeus, 2006) within ±15 minutes back to 2,500 years before $J2000$ ($n = 11$ events, −524 to 985 CE). The shipped stack additionally shows a Pearson $r = +0.37$ correspondence with the Bond et al. (1997) North-Atlantic ice-rafted-debris archive over the −4, 000 to +1, 800 CE window — an *open correspondence, not a cross-validation*: it accounts for only ~13% of variance, fails the four null tests reported in subsection 14.11, and is not carried by the $8H/1830$ Bond band itself; the four cycles rest on their ΔT closure, which is what they were fitted to and what they achieve. The historical record rejects the full Munk-MacDonald-scale non-tidal speedup and decomposes the remaining medieval residual into four framework-native sub-Milankovitch $8H$-lattice harmonics (the shipped 4-flag stack: Bond, Hallstatt, Jose5, Jose4 — four spectral signals carried at their nearest $8H$-lattice labels), the Core-mantle swing episode (time-varying mantle-core coupling), and a broadband noise floor (subsection 14.11). The lunar theory behind these tests is itself delivered framework-natively as "The Derived Moon" (DLT-1, subsection 14.9): every constant of the Meeus Ch. 47 series carries a derived, attributed, observationally defined, or design-anchored origin, with the periodic amplitudes reproduced from three-body gravity at 100.0 ± 0.1% and the secular T^2 budget closed against primary sources with zero free parameters.

Taken together, the six Fibonacci Laws, the canonical Climate Formula, and the Expanding Solar System Resonance Theory form one continuous chain: a single observationally anchored timescale organises the solar system's spatial architecture, Earth's precessional dynamics, the paleoclimate spectrum, and the deep-time evolution of all three. Because every layer derives from the same 6-parameter fit (subsection 14.3), the framework stands or falls as a whole — and the 27 predictions catalogued above, led by BepiColombo (from April 2027) and the Vera Rubin Observatory (2025–2035), will deliver the first decisive tests within this decade.

Acknowledgments

The author thanks the developers of JPL Horizons, WebGeocalc, and the IAU standards for providing the observational data upon which this model is built. The interactive 3D simulation was built using Three.js.

Data Availability

All data, formulas, and calculation scripts underlying this work are publicly available:

- Model documentation: `https://holisticuniverse.com`
- Interactive 3D simulation: `https://3d.holisticuniverse.com`

- Data visualization: https://data.holisticuniverse.com
- Source code, predictive formula scripts, significance tests, and technical docs: https://github.com/dvansonsbeek/3d
- Source code licence: GNU Affero General Public License v3.0 (https://github.com/dvansonsbeek/3d/blob/master/LICENSE); derivation and attribution notices: https://github.com/dvansonsbeek/3d/blob/master/NOTICE
- Third-party dataset provenance, licences and redistribution rights: https://github.com/dvansonsbeek/3d/blob/master/data/PROVENANCE.md

Conflict of Interest

The author declares no conflicts of interest. This research received no external funding.

References

Aschwanden, M. J. (2018). Self-organizing systems in planetary physics: Harmonic resonances of planet and moon orbits. *New Astronomy*, 58, 107–123.

Backus, G. (1969). Critique of "The Resonant Structure of the Solar System" by A. M. Molchanov. *Icarus*, 11, 88–92.

Bao, X., Zhao, H., Zhang, S., Li, X., Tan, W., Li, C., et al. (2023). Length of day at c. 1.1 Ga based on cyclostratigraphic analyses of the Nanfen Formation in the North China craton, and its geodynamic implications. *Journal of the Geological Society*, 180(1). doi:10.1144/jgs2022-022.

Barker, S., Lisiecki, L. E., Knorr, G., Nuber, S., & Tzedakis, P. C. (2025). Distinct roles for precession, obliquity, and eccentricity in Pleistocene 100-kyr glacial cycles. *Science*, 387(6737), eadp3491.

Bartlett, B. C., & Stevenson, D. J. (2016). Analysis of a Precambrian resonance-stabilized day length. *Geophysical Research Letters*, 43, 5716–5724.

Batygin, K., & Brown, M. E. (2016). Evidence for a Distant Giant Planet in the Solar System. *Astronomical Journal*, 151, 22.

Berche, B., & Medina, E. (2024). The advance of Mercury's perihelion. *European Journal of Physics*, 45, 055601.

Bereiter, B., Eggleston, S., Schmitt, J., Nehrbass-Ahles, C., Stocker, T. F., Fischer, H., Kipfstuhl, S., & Chappellaz, J. (2015). Revision of the EPICA Dome C CO_2 record from 800 to 600 kyr before present. *Geophysical Research Letters*, 42(2), 542–549.

Berger, A. (1978). Long-term variations of daily insolation and Quaternary climatic changes. *Journal of the Atmospheric Sciences*, 35, 2362–2367.

Berger, A. (1988). Milankovitch theory and climate. *Reviews of Geophysics*, 26(4), 624–657.

Berger, A. & Loutre, M. F. (2002). An exceptionally long interglacial ahead? *Science*, 297(5585), 1287–1288.

Bills, B. G., & Ray, R. D. (1999). Lunar orbital evolution: A synthesis of recent results. *Geophysical Research Letters*, 26(19), 3045–3048. doi:10.1029/1999GL008348.

Bills, B. G., & Comstock, R. L. (2005). Forced obliquity variations of Mercury. *Journal of Geophysical Research*, 110, E04006.

Bond, G., Showers, W., Cheseby, M., Lotti, R., Almasi, P., deMenocal, P., Priore, P., Cullen, H., Hajdas, I., & Bonani, G. (1997). A pervasive millennial-scale cycle in North Atlantic Holocene and glacial climates. *Science*, 278(5341), 1257–1266.

Bond, G., Kromer, B., Beer, J., et al. (2001). Persistent solar influence on North Atlantic climate during the Holocene. *Science*, 294(5549), 2130–2136. doi:10.1126/science.1065680.

Boulila, S., Vahlenkamp, M., De Vleeschouwer, D., et al. (2018). Towards a robust and consistent middle Eocene astronomical timescale. *Earth and Planetary Science Letters*, 486, 94–107.

Brown, E. W. (1896). *An Introductory Treatise on the Lunar Theory*. Cambridge University Press, Cambridge.

Brouwer, D., & Clemence, G. M. (1961). *Methods of Celestial Mechanics*. Academic Press, New York.

Capitaine, N., Wallace, P. T., & Chapront, J. (2003). Expressions for IAU 2000 precession quantities. *Astronomy & Astrophysics*, 412, 567–586.

Charvátová, I. (2000). Can origin of the 2400-year cycle of solar activity be caused by solar inertial motion? *Annales Geophysicae*, 18(4), 399–405.

The CenCO2PIP Consortium (Hönisch, B., Royer, D. L., Breecker, D. O., et al.) (2023). Toward a Cenozoic history of atmospheric CO_2. *Science*, 382(6675), eadi5177.

Chalk, T. B., Hain, M. P., Foster, G. L., et al. (2017). Causes of ice age intensification across the Mid-Pleistocene Transition. *Proceedings of the National Academy of Sciences*, 114(50), 13114–13119.

Chapront, J., Chapront-Touzé, M., & Francou, G. (2002). A new determination of lunar orbital parameters, precession constant and tidal acceleration from LLR measurements. *Astronomy & Astrophysics*, 387, 700–709.

Cheng, M., Tapley, B. D., & Ries, J. C. (2013). Deceleration in the Earth's oblateness. *Journal of Geophysical Research: Solid Earth*, 118(2), 740–747.

Cheng, H., Edwards, R. L., Sinha, A., et al. (2016). The Asian monsoon over the past 640,000 years and ice age terminations. *Nature*, 534(7609), 640–646.

Chirikov, B. V. (1979). A universal instability of many-dimensional oscillator systems. *Physics Reports*, 52(5), 263–379.

Clemence, G. M. (1947). The relativity effect in planetary motions. *Reviews of Modern Physics*, 19(4), 361–364.

Colombo, G. (1966). Cassini's second and third laws. *The Astronomical Journal*, 71, 891–896.

Cottereau, L., & Souchay, J. (2009). Rotation of rigid Venus: a complete precession-nutation model. *Astronomy & Astrophysics*, 507, 1635–1648.

Cox, C. M., & Chao, B. F. (2002). Detection of a large-scale mass redistribution in the terrestrial system since 1998. *Science*, 297(5582), 831–833.

Damon, P. E., & Sonett, C. P. (1991). Solar and terrestrial components of the atmospheric ^{14}C variation spectrum. In C. P. Sonett, M. S. Giampapa, & M. S. Matthews (Eds.), *The Sun in Time* (pp. 360–388). University of Arizona Press.

de la Vega, E., Chalk, T. B., Wilson, P. A., Bysani, R. P., & Foster, G. L. (2020). Atmospheric CO_2 during the Mid-Piacenzian Warm Period and the M2 glaciation. *Scientific Reports*, 10, 11002.

de Winter, N. J., Goderis, S., Van Malderen, S. J. M., et al. (2020). Subdaily-scale chemical variability in a *Torreites sanchezi* rudist shell: Implications for rudist paleobiology and the Cretaceous day-night cycle. *Paleoceanography and Paleoclimatology*, 35(2), e2019PA003723.

Dickey, J. O., Bender, P. L., Faller, J. E., et al. (1994). Lunar laser ranging: A continuing legacy of the Apollo program. *Science*, 265(5171), 482–490.

Dumberry, M., & Bloxham, J. (2006). Azimuthal flows in the Earth's core and changes in length of day at millennial timescales. *Geophysical Journal International*, 165(1), 32–46.

Dutkiewicz, A., Boulila, S., & Müller, R. D. (2024). Deep-sea hiatus record reveals orbital pacing by 2.4 Myr eccentricity grand cycles. *Nature Communications*, 15, 1998.

Dyez, K. A., Hönisch, B., & Schmidt, G. A. (2018). Early Pleistocene obliquity-scale pCO_2 variability at ~1.5 million years ago. *Paleoceanography and Paleoclimatology*, 33(11), 1270–1291.

Espenak, F., & Meeus, J. (2006). *Five Millennium Canon of Solar Eclipses:* −1999 *to* +3000 *(2000 BCE to 3000 CE)*. NASA Technical Publication TP-2006-214141. https://eclipse.gsfc.nasa.gov/SEpubs/5MKSE.html.

Farhat, M., Auclair-Desrotour, P., Boué, G., & Laskar, J. (2022). The resonant tidal evolution of the Earth–Moon distance. *Astronomy & Astrophysics*, 665, L1.

Farley, K. A. (1995). Cenozoic variations in the flux of interplanetary dust recorded by ^{3}He in a deep-sea sediment. *Nature*, 376, 153–156.

Fienga, A., Laskar, J., Kuchynka, P., et al. (2011). The INPOP10a planetary ephemeris and its applications in fundamental physics. *Celestial Mechanics and Dynamical Astronomy*, 111, 363–385.

Ganopolski, A., Winkelmann, R. & Schellnhuber, H. J. (2016). Critical insolation–CO_2 relation for diagnosing past and future glacial inception. *Nature*, 529, 200–203.

Greene, J. M. (1979). A method for determining a stochastic transition. *Journal of Mathematical Physics*, 20(6), 1183–1201.

Grimm, S. L., Demory, B.-O., Gillon, M., et al. (2018). The nature of the TRAPPIST-1 exoplanets. *Astronomy & Astrophysics*, 613, A68.

Hansen, J., Sato, M., Russell, G., & Kharecha, P. (2013). Climate sensitivity, sea level and atmospheric carbon dioxide. *Philosophical Transactions of the Royal Society A*, 371(2001), 20120294.

Harkness, W. (1891). *The Solar Parallax and Its Related Constants, Including the Figure and Density of the Earth*. Washington: U.S. Government Printing Office.

Hays, J. D., Imbrie, J., & Shackleton, N. J. (1976). Variations in the Earth's orbit: Pacemaker of the ice ages. *Science*, 194(4270), 1121–1132.

Holme, R. (1998). Electromagnetic core-mantle coupling — I. Explaining decadal changes in the length of day. *Geophysical Journal International*, 132(1), 167–180.

Holme, R., & de Viron, O. (2013). Characterization and implications of intradecadal variations in length of day. *Nature*, 499, 202–204. doi:10.1038/nature12282.

Huang, S., Ormel, C. W., Portegies Zwart, S., Kokubo, E., & Yi, T. (2025). A resonant beginning for the Solar System terrestrial planets. *The Astrophysical Journal*, in press. arXiv:2506.04164. doi:10.3847/1538-4357/ade25a.

Iorio, L. (2009). The recently determined anomalous perihelion precession of Saturn. *The Astronomical Journal*, 137, 3615–3618.

IPCC (2021). *Climate Change 2021: The Physical Science Basis. Contribution of Working Group I to the Sixth Assessment Report of the Intergovernmental Panel on Climate Change*. Masson-Delmotte, V., et al. (eds.). Cambridge University Press, Cambridge, United Kingdom and New York, NY, USA.

Kahan, D. S., Folkner, W. M., Buccino, D. R., et al. (2021). Mars precession rate determined from radiometric tracking of the InSight Lander. *Planetary and Space Science*, 199, 105208.

Kawamura, K., Parrenin, F., Lisiecki, L., et al. (2007). Northern Hemisphere forcing of climatic cycles in Antarctica over the past 360,000 years. *Nature*, 448, 912–916.

Köhler, P., Stap, L. B., von der Heydt, A. S., et al. (2017). A state-dependent quantification of climate sensitivity based on paleodata of the last 2.1 million years. *Paleoceanography*, 32(11), 1102–1114.

Laskar, J. (1989). A numerical experiment on the chaotic behaviour of the Solar System. *Nature*, 338, 237–238.

Laskar, J., Joutel, F., & Boudin, F. (1993). Orbital, precessional and insolation quantities for the Earth from −20 Myr to +10 Myr. *Astronomy & Astrophysics*, 270, 522–533.

Laskar, J. (1997). Large scale chaos and the spacing of inner planets. *Astronomy & Astrophysics*, 317, L75–L78.

Laskar, J., Robutel, P., Joutel, F., Gastineau, M., Correia, A. C. M., & Levrard, B. (2004). A long-term numerical solution for the insolation quantities of the Earth. *Astronomy & Astrophysics*, 428, 261–285.

Laskar, J., Fienga, A., Gastineau, M., & Manche, H. (2011). La2010: A new orbital solution for the long-term motion of the Earth. *Astronomy & Astrophysics*, 532, A89.

Lantink, M. L., Davies, J. H. F. L., Ovtcharova, M., & Hilgen, F. J. (2022). Milankovitch cycles in banded iron formations constrain the Earth-Moon system 2.46 billion years ago. *Proceedings of the National Academy of Sciences*, 119(40), e2117146119. doi:10.1073/pnas.2117146119.

Lawler, S. M., Shankman, C., Kaib, N., et al. (2017). Observational signatures of a massive distant planet on the scattering disk. *Astronomical Journal*, 153(1), 33.

Li, J., Xia, Z. J., & Zhou, L. (2019). Calibration of the angular momenta of the minor planets in the solar system. *Astronomy & Astrophysics*, 630, A68.

Lisiecki, L. E., & Raymo, M. E. (2005). A Pliocene–Pleistocene stack of 57 globally distributed benthic δ^{18}O records. *Paleoceanography*, 20, PA1003.

Loutre, M. F., & Berger, A. (2003). Marine Isotope Stage 11 as an analogue for the present interglacial. *Global and Planetary Change*, 36(3), 209–217.

Martínez-Botí, M. A., Foster, G. L., Chalk, T. B., et al. (2015). Plio-Pleistocene climate sensitivity evaluated using high-resolution CO_2 records. *Nature*, 518, 49–54.

Mecheri, R., & Abdelatif, T. (2022). Secular Variations of the Sun's Gravitational Quadrupole Moment and Their Impact on GR Tests. *Remote Sensing*, 14(19), 4798.

Meeus, J. (1998). *Astronomical Algorithms*, 2nd edn. (Richmond: Willmann-Bell).

Meyers, S. R., & Malinverno, A. (2018). Proterozoic Milankovitch cycles and the history of the solar system. *Proceedings of the National Academy of Sciences*, 115(25), 6363–6368. doi:10.1073/pnas.1717689115.

Mitchell, R. N., & Kirscher, U. (2023). Mid-Proterozoic day length stalled by tidal resonance. *Nature Geoscience*, 16, 567–569.

Morbidelli, A., & Giorgilli, A. (1995). Superexponential stability of KAM tori. *Journal of Statistical Physics*, 78, 1607–1617.

Muller, R. A., & MacDonald, G. J. (1997a). Glacial cycles and astronomical forcing. *Science*, 277, 215–218.

Muller, R. A., & MacDonald, G. J. (1997b). Spectrum of 100-kyr glacial cycle: Orbital inclination, not eccentricity. *Proceedings of the National Academy of Sciences*, 94, 8329–8334.

Munk, W. H., & MacDonald, G. J. F. (1960). *The Rotation of the Earth: A Geophysical Discussion*. Cambridge University Press.

Néron de Surgy, O., & Laskar, J. (1997). On the long term evolution of the spin of the Earth. *Astronomy & Astrophysics*, 318, 975–989.

Newcomb, S. (1898). Tables of the Motion of the Earth on its Axis and Around the Sun. *Astronomical Papers Prepared for the Use of the American Ephemeris and Nautical Almanac*, Vol. VI, Part I (Washington: Bureau of Equipment, Navy Department).

Pälike, H., Norris, R. D., Herrle, J. O., et al. (2006). The heartbeat of the Oligocene climate system. *Science*, 314, 1894–1898.

Pannella, G. (1972). Paleontological evidence on the Earth's rotational history since early Precambrian. *Astrophysics and Space Science*, 16, 212–237.

Park, R. S., Folkner, W. M., Konopliv, A. S., et al. (2017). Precession of Mercury's perihelion from ranging to the MESSENGER spacecraft. *The Astronomical Journal*, 153(3), 121.

Park, R. S., et al. (2021). The JPL planetary and lunar ephemerides DE440 and DE441. *The Astronomical Journal*, 161(3), 105.

Patterson, C. (1956). Age of meteorites and the earth. *Geochimica et Cosmochimica Acta*, 10(4), 230–237.

Peale, S. J. (1969). Generalized Cassini's laws. *The Astronomical Journal*, 74, 483–489.

Peale, S. J. (2005). The free precession and libration of Mercury. *Icarus*, 178(1), 4–18.

Peltier, W. R. (2004). Global glacial isostasy and the surface of the ice-age Earth: The ICE-5G (VM2) model and GRACE. *Annual Review of Earth and Planetary Sciences*, 32, 111–149.

Petit, J. R., Jouzel, J., Raynaud, D., et al. (1999). Climate and atmospheric history of the past 420,000 years from the Vostok ice core, Antarctica. *Nature*, 399, 429–436.

Pitjeva, E. V. (2010). EPM ephemerides and relativity. *Proceedings of the IAU Symposium*, 261, 170–178.

Pireaux, S., Rozelot, J.-P., & Godier, S. (2003). Solar quadrupole moment and purely relativistic gravitation contributions to Mercury's perihelion advance. *Astrophysics and Space Science*, 284, 1159–1194.

Pitjeva, E. V., & Pitjev, N. P. (2013). Relativistic effects and dark matter in the Solar system from observations of planets and spacecraft. *Monthly Notices of the Royal Astronomical Society*, 432, 3431–3437.

Pletser, V. (2019). Prevalence of Fibonacci numbers in orbital period ratios in solar planetary and satellite systems and in exoplanetary systems. *Astrophysics and Space Science*, 364, 158.

Ridgwell, A. J., Watson, A. J., & Raymo, M. E. (1999). Is the spectral signature of the 100 kyr glacial cycle consistent with a Milankovitch origin? *Paleoceanography*, 14(4), 437–440.

Roe, G. (2006). In defense of Milankovitch. *Geophysical Research Letters*, 33, L24703.

Rogoszinski, Z., & Hamilton, D. P. (2020). Tilting Ice Giants with a Spin–Orbit Resonance. *The Astrophysical Journal*, 888, 60.

Saillenfest, M., Lari, G., & Courtot, A. (2020). The future large obliquity of Jupiter. *Astronomy & Astrophysics*, 640, A11.

Saillenfest, M., Lari, G., & Boué, G. (2021). The large obliquity of Saturn explained by the fast migration of Titan. *Nature Astronomy*, 5, 345–349.

Saillenfest, M., Rogoszinski, Z., Lari, G., et al. (2022). Tilting Uranus via the migration of an ancient satellite. *Astronomy & Astrophysics*, 668, A108.

Sherwood, S. C., Webb, M. J., Annan, J. D., et al. (2020). An assessment of Earth's climate sensitivity using multiple lines of evidence. *Reviews of Geophysics*, 58(4), e2019RG000678.

Smulsky, J. J. (2011). New components of the Mercury's perihelion precession. *Natural Science*, 3(4), 268–274.

Soter, S. (2006). What Is a Planet? *The Astronomical Journal*, 132(6), 2513–2519.

Souami, D., & Souchay, J. (2012). The solar system's invariable plane. *Astronomy & Astrophysics*, 543, A133.

Standish, E. M., & Williams, J. G. (1992). Keplerian Elements for Approximate Positions of the Major Planets. JPL Solar System Dynamics, `https://ssd.jpl.nasa.gov/planets/approx_pos.html`.

Steinhilber, F., Abreu, J. A., Beer, J., et al. (2012). 9,400 years of cosmic radiation and solar activity from ice cores and tree rings. *Proceedings of the National Academy of Sciences*, 109(16), 5967–5971. `doi:10.1073/pnas.1118965109`.

Stephenson, F. R. (1997). *Historical Eclipses and Earth's Rotation*. Cambridge University Press.

Stephenson, F. R., & Steele, J. M. (2006). Astronomical dating of Babylonian texts describing the total solar eclipse of s.e. 175. *Journal for the History of Astronomy*, 37, 55–62.

Stephenson, F. R., Morrison, L. V., & Hohenkerk, C. Y. (2016). Measurement of the Earth's rotation: 720 BC to AD 2015. *Proceedings of the Royal Society A*, 472(2196), 20160404.

Touma, J., & Wisdom, J. (1994). Evolution of the Earth–Moon system. *Astronomical Journal*, 108, 1943–1961.

Tzedakis, P. C., Channell, J. E. T., Hodell, D. A., Kleiven, H. F., & Skinner, L. C. (2012). Determining the natural length of the current interglacial. *Nature Geoscience*, 5, 138–141.

Veres, D., Bazin, L., Landais, A., et al. (2013). The Antarctic ice core chronology (AICC2012): an optimized multi-parameter and multi-site dating approach for the last 120 thousand years. *Climate of the Past*, 9(4), 1733–1748.

Vervoort, P., Horner, J., Kane, S. R., Kirtland Turner, S., & Gilmore, J. B. (2022). System Architecture and Planetary Obliquity: Implications for Long-term Habitability. *The Astronomical Journal*, 164(4), 130.

Vondrák, J., Capitaine, N., & Wallace, P. (2011). New precession expressions, valid for long time intervals. *Astronomy & Astrophysics*, 534, A22.

Walker, J. C. G., Hays, P. B., & Kasting, J. F. (1981). A negative feedback mechanism for the long-term stabilization of Earth's surface temperature. *Journal of Geophysical Research*, 86(C10), 9776–9782.

Wells, J. W. (1963). Coral growth and geochronometry. *Nature*, 197, 948–950.

Westerhold, T., Marwan, N., Drury, A. J., et al. (2020). An astronomically dated record of Earth's climate and its predictability over the last 66 million years. *Science*, 369, 1383–1387.

Willeit, M., Ganopolski, A., Calov, R., & Brovkin, V. (2019). Mid-Pleistocene transition in glacial cycles explained by declining CO_2 and regolith removal. *Science Advances*, 5(4), eaav7337.

Williams, G. E. (2000). Geological constraints on the Precambrian history of Earth's rotation and the Moon's orbit. *Reviews of Geophysics*, 38(1), 37–59.

Wilson, C. (1985). The great inequality of Jupiter and Saturn: from Kepler to Laplace. *Archive for History of Exact Sciences*, 33, 15–290.

Williams, J. G., Konopliv, A. S., Boggs, D. H., et al. (2014). Lunar interior properties from the GRAIL mission. *Journal of Geophysical Research: Planets*, 119(7), 1546–1578.

Wu, Y., Malinverno, A., Meyers, S. R., & Hinnov, L. A. (2024). A 650-Myr history of Earth's axial precession frequency and the evolution of the Earth-Moon system derived from cyclostratigraphy. *Science Advances*, 10(42), eado2412. `doi:10.1126/sciadv.ado2412`.

Wunsch, C. (2003). The spectral description of climate change including the 100 ky energy. *Climate Dynamics*, 20, 353–363.

Zahnle, K., & Walker, J. C. G. (1987). A constant daylength during the Precambrian era? *Precambrian Research*, 37(2), 95–105.

Zeebe, R. E., & Lantink, M. L. (2024). A secular solar system resonance that disrupts the dominant cycle in Earth's orbital eccentricity ($g_2 - g_5$): Implications for astrochronology. *Astronomical Journal*, 167(5), 204.

Zhou, M., Wu, H., Hinnov, L. A., Fang, Q., Zhang, S., Yang, T., & Shi, M. (2024). Earth-Moon dynamics from cyclostratigraphy reveals possible ocean tide resonance in the Mesoproterozoic era. *Science Advances*, 10(31), eadn7674. doi:10.1126/sciadv.adn7674.